

**Magnetization dynamics in all-optical
pump-probe experiments:
spin-wave modes and spin-current damping**

Dissertation
zur Erlangung des Doktorgrades
der Mathematisch-Naturwissenschaftlichen Fakultäten
der Georg-August-Universität zu Göttingen

vorgelegt von
Marija Djordjević Kaufmann
aus
Niš, Serbien

Göttingen 2006

D 7

Referent: Herr Prof Dr. M. Münzenberg

Korreferent: Herr Prof. Dr. C. H. Back

Tag der mündlichen Prüfung: 6. November 2006

Contents

1	Introduction	1
2	Theory of magnetization dynamics	3
2.1	Introduction to magnetization dynamics	3
2.1.1	Magnetization precession	3
2.1.2	Magnetic damping	5
2.1.3	Lagrangian Formalism for the magnetization dynamics	5
2.1.4	Energies of a ferromagnet	6
2.2	Derivation of $\omega(H)$	9
2.2.1	Landau-Lifshitz equation in spherical coordinates	10
2.2.2	Derivation of the Kittel formula	12
2.2.3	Derivation of the magnon dispersion relation	13
2.3	Derivation of $\alpha(\tau_\alpha)$	16
2.3.1	α versus τ_α for Kittel mode	16
2.3.2	α versus τ_α for standing spin-wave mode	19
3	Experimental technique	21
3.1	Methods for investigating magnetization dynamics	21
3.1.1	Techniques on the time scale	22
3.1.2	Techniques on the frequency scale	23
3.2	All-optical pump-probe experiments	25
3.2.1	Ultrafast demagnetization	26
3.2.2	Induced magnetization precession	28
3.3	Magneto-optical Kerr Effect	28
3.3.1	Phenomenological origin	29
3.3.2	Quantum mechanical origin	32
3.4	Measurement setup	33
3.4.1	Detection of the Kerr Effect	33
3.4.2	Detection of the Time Resolved Kerr Effect	36

3.4.3	Femtosecond laser system	37
3.4.4	Electromagnet	38
3.5	Samples	39
3.5.1	XRD characterization	41
4	Ultrafast demagnetization	43
4.1	Variation of the external magnetic field	44
4.2	Variation of the pump fluence	45
4.3	Modeling by micromagnetic simulations	47
4.4	Conclusion	50
5	Magnetization dynamics on a 100ps timescale	53
5.1	Coherent precession modes	55
5.1.1	Kittel $k = 0$ mode	56
5.1.2	Standing spin-wave mode	59
5.1.3	Dipole modes	61
5.2	Incoherent magnetic relaxation	66
5.3	Mode dependent damping	68
5.4	Dependence on external field orientation	70
5.4.1	Small angles between magnetization and applied field	70
5.4.2	Large angles between magnetization and applied field	72
5.5	Dependence on the pump fluence	76
5.6	Conclusion	79
6	The Gilbert damping parameter	81
6.1	Different origins of damping	82
6.2	Theoretical modeling of damping	83
6.2.1	Damping by spin-flip scattering	84
6.2.2	s-d current model	86
6.2.3	The breathing Fermi surface model	89
6.2.4	Non-local damping	94
6.3	Experimental approach	100
6.3.1	Variation of the demagnetization rate	101
6.3.2	Different magnetization relaxation channels	103
6.4	Extrinsic damping for F/N samples	104
6.4.1	Influence of roughness	107
6.5	Non-local damping	110
6.5.1	Si/Pd/Ni/Cu individual samples	111
6.5.2	Si/Pd/Ni/Al wedge sample	114
6.5.3	Si/Ni/Dy/Al wedge sample	117
6.5.4	Si/Cr/Ni/Cu individual samples	121
6.6	Conclusion	126
7	Summary	129
	Bibliography	131

CHAPTER 1

Introduction

Even in nowadays science, light interaction with solids is an intriguing area of research. In particular, if the light can magnetize or demagnetize a ferromagnet and if, in which timescales, are challenging questions to be yet answered. The absorption of intense laser pulses by a ferromagnet causes a rearrangement of the electrons and the magnetic moments through fundamental microscopical physical processes, such as electron-electron scattering, electron-phonon scattering and magnon generation. All these processes are accessible with femtosecond laser pulses. With the time resolution inherent, femtosecond laser pulses in all-optical pump-probe experiments can be used to study the basic time constants of ultrafast demagnetization, the magnetic precessional modes, as well as the energy dissipation processes, which all determine the Gilbert damping. These experiments lighten up a theoretically demanding area, in which both the dominating interactions and the timescales of the interaction processes are still subject of extensive research.

Current technological development demands new insight into the magnetization relaxation processes in the sub-nanosecond regime. The increased density of magnetic memories is achieved using giant magneto resistance (GMR) and tunnel magneto resistance (TMR) effects. Novel non-volatile magnetic devices are based on Magnetic Random Access Memory (MRAM), in which each bit can be separately manipulated by means of current controlled write or read. The timescales of the magnetic recording, limited to the motion of the magnetic precession, are approaching the ns timescale. Hence, fundamental research on the magnetization dynamics on the fs scale has become a major interest for the storage industry.

New approaches have been developed to manipulate spins on the nm scale and in GHz frequency range. Some of these directly inspired the research in

this thesis. The thermally assisted writing, for example, is based on the short anisotropy reduction, which makes it easier to switch the magnetization in moderate magnetic fields. The engineering of the Gilbert damping parameter with the emission of spin currents on the ferromagnet/normal metal prevents the ringing of the magnetization during precessional switching.

The application of ultrashort laser pulses was a major breakthrough in time resolved studies of magnetization dynamics, which extended time resolution into the sub ps range. Intensive 80fs laser pulses from a Ti:Sapphire oscillator with a wavelength of 800nm are used in the all-optical pump-probe scheme to investigate the magnetization dynamics of thin ferromagnetic samples using the magneto-optical Kerr effect. The magnetization relaxation upon laser excitation is characterized by an ultrafast demagnetization, which takes place shortly after the absorption of the pump pulse, and the coherent precession of magnetization on the 100ps timescale. The former reflects incoherent, and the later coherent processes. This can determine both the timescale of the magnetization relaxation and the ultimate timescale of the energy dissipation processes.

This PhD thesis is organized as follows: The second chapter gives the basic premises of the theoretical background of magnetization dynamics and derives the frequency and damping dispersion relation. The third chapter handles the measurement techniques used in our experiment. Chapters four, five and six cover the experimental findings regarding magnetization dynamics upon laser excitations. In detail, the fourth chapter presents ultrafast demagnetization. Chapter five gives an overview of the magnetization dynamics on a 100ps timescale using coherent precession modes and incoherent magnetic background. Chapter six discusses the Gilbert damping parameter, starting with theoretical approaches to model magnetic damping up to a presentation of the results on non-local damping for various ferromagnet/normal metal samples. At the end, a conclusion regarding the main achievements of this thesis is given.

CHAPTER 2

Theory of magnetization dynamics

This chapter presents the basic theoretical premises regarding magnetization dynamics by deriving the equation of motion for the damped magnetic precession and introducing the different contributions to the magnetic free energy. The frequency dispersion relation is then derived for the Kittel $k = 0$ mode and for the standing spin-wave mode, based on the configuration used in our experiments. Similarly, the relation between the Gilbert damping parameter and the exponential decay time of the precession amplitude is also derived for different precession modes.

2.1 Introduction to magnetization dynamics

2.1.1 Magnetization precession

The dynamic behavior of a spin is determined by the equation of motion, which can be derived from the quantum theory[1]. The time evolution of a spin observable S is determined by its commutator with the Hamilton operator H :

$$i\hbar \frac{d}{dt} \mathbf{S} = [\mathbf{S}, H]. \quad (2.1)$$

The Hamiltonian, which describes the interaction of the spin with the external magnetic field, given by its flux \mathbf{B} , can be expressed as:

$$H = -\frac{g\mu_B}{\hbar} \mathbf{S} \cdot \mathbf{B}, \quad (2.2)$$

where μ_B is the Bohr magneton ($\mu_B < 0$) and g is the gyromagnetic factor for a free electron. The z-component of the commutator in Eq. 2.1 can be derived

as:

$$\begin{aligned}
 [S_z, H] &= -\frac{g\mu_B}{\hbar} [S_z, S_x B_x + S_y B_y + S_z B_z] \\
 &= -\frac{g\mu_B}{\hbar} ([S_z, S_x] B_x + [S_z, S_y] B_y) \\
 &= ig\mu_B (B_y S_x + B_x S_y) \\
 &= ig\mu_B (\mathbf{S} \times \mathbf{B})_x ,
 \end{aligned}$$

with the help of the commutation rules for spin operators:

$$[S_i, S_j] = i\hbar\epsilon_{ijk}S_k .$$

Corresponding expressions can be derived for the other two components of the spin, which lead to the spin equation of motion:

$$\frac{d}{dt} \langle \mathbf{S} \rangle = \frac{g\mu_B}{\hbar} (\mathbf{S} \times \mathbf{B}) . \quad (2.3)$$

The derived equation of motion for one spin can be further generalized for the case of homogeneous magnetization within the macrospin model, considering the relation between the magnetization \mathbf{M} and $\langle \mathbf{S} \rangle$:

$$\mathbf{M} = \frac{g\mu_B}{\hbar} \langle \mathbf{S} \rangle \quad (2.4)$$

Therewith, the analogous equation of motion of the magnetization in an external field \mathbf{H} is observed as in case of one spin:

$$\frac{d}{dt} \mathbf{M} = -\gamma\mu_0 \mathbf{M} \times \mathbf{H} = \gamma_0 \mathbf{M} \times \mathbf{H} , \quad (2.5)$$

where the gyromagnetic ratio $\gamma = g\mu_B/\hbar$ is introduced and $\gamma_0 > 0$. Eq. 2.5 is known as the Landau-Lifshitz (LL) equation.

The specific properties of the LL equation are observed for a constant magnetic field \mathbf{H} , due to the vector product specifications:

$$\frac{d}{dt} M^2 = 0 , \quad \frac{d}{dt} (\mathbf{M} \cdot \mathbf{H}) = 0 .$$

The first equation states, that the absolute value of the magnetization does not change during the precession around a constant external field. The second equation implies that the angle between the magnetization and the external field is constant during the rotation. The schematically presented magnetization rotation is shown in Fig. 2.1 a), in which the top of the magnetization vector marks out a circle around \mathbf{H} . The magnetization vector \mathbf{M} precesses around the magnetic field \mathbf{H} with the frequency $\omega = \gamma_0 H$. This frequency is also known as the Larmor frequency. The derived equation of motion for the magnetization in an external field \mathbf{H} can be generalized for the case in which the anisotropy fields and the exchange interaction contribute to the magnetic energy by simply replacing \mathbf{H} with the effective magnetic field \mathbf{H}_{eff} .

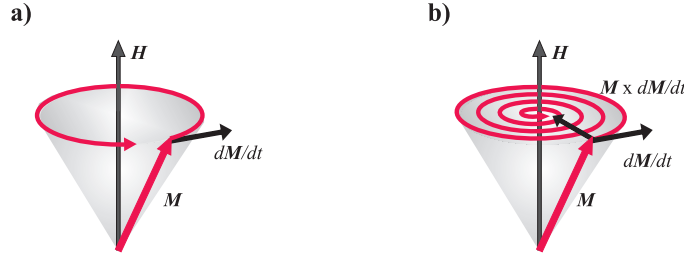


Figure 2.1: Magnetization torque without damping and with damping term.

2.1.2 Magnetic damping

The Landau-Lifshitz equation implies that the magnetization, once taken out of the equilibrium position, precesses around the external field \mathbf{H} infinitely long. In reality, though, the magnetization eventually aligns with the external field. This experimentally observable fact demands the introduction of a dissipation term into the Landau-Lifshitz equation. As shown in Fig. 2.1 b) the amplitude of the magnetization precession is gradually reduced until the magnetization aligns with the external field. To estimate the damping term, Gilbert first applied a thermodynamical approach in the following form:

$$\frac{\alpha}{M_s} \left(\mathbf{M} \times \frac{d}{dt} \mathbf{M} \right)$$

where α denotes the dimensionless Gilbert damping parameter. It determines how fast the energy of the magnetization precession is dissipated from the system. With this, the equation of motion for the magnetization is given by the Landau-Lifshitz-Gilbert (LLG) equation:

$$\frac{d}{dt} \mathbf{M} = -\gamma \mu_0 (\mathbf{M} \times \mathbf{H}) + \frac{\alpha}{M_s} \left(\mathbf{M} \times \frac{d}{dt} \mathbf{M} \right). \quad (2.6)$$

The Gilbert damping parameter for transition metals is much smaller than 1, which allows the magnetization to make a number of precessions before it is aligned with the external field. The nature of the damping and different contributions to the energy dissipation processes are explained in detail in Chapter 6.

2.1.3 Lagrangian Formalism for the magnetization dynamics

An elegant method to determine the dynamics of the magnetization vector in an external field can be also derived from the Lagrangian formalism[1, 2]. The Lagrangian density for the magnetization precession with the generalized coordinates θ and φ is given by:

$$L = -w - \frac{\mu_0 M_s}{\gamma_0} \dot{\varphi} \cos \theta, \quad \dot{\varphi} = \frac{d\varphi}{dt} \quad (2.7)$$

where w denotes the free energy density functional. The classical equation describes the motion of the magnetization:

$$\frac{d}{dt} \frac{\partial L}{\partial \dot{\theta}} - \frac{\partial L}{\partial \theta} = 0 \quad (2.8)$$

$$\frac{d}{dt} \frac{\partial L}{\partial \dot{\varphi}} - \frac{\partial L}{\partial \varphi} = 0 \quad (2.9)$$

The free energy density functional of the magnetization in the external field $\mathbf{H} = H\mathbf{e}_z$ is given by:

$$w = -\mu_0 M_s \mathbf{m} \cdot \mathbf{H} . \quad (2.10)$$

Without damping, the magnetization obeys the following equations:

$$\dot{\theta} = 0 , \quad \dot{\varphi} = \gamma_0 H . \quad (2.11)$$

The first equation implies that one of the generalized coordinates θ stays constant during the magnetization motion. The second equation implies that φ harmonically changes in time according to the Larmor precession frequency.

The damping term can be explicitly included within the Lagrangian formalism with a scalar function R [3]. The equations of motion are then given by:

$$\frac{d}{dt} \frac{\partial L}{\partial \dot{\theta}} - \frac{\partial L}{\partial \theta} + \frac{\partial R}{\partial \dot{\theta}} = 0 \quad (2.12)$$

$$\frac{d}{dt} \frac{\partial L}{\partial \dot{\varphi}} - \frac{\partial L}{\partial \varphi} + \frac{\partial R}{\partial \dot{\varphi}} = 0 . \quad (2.13)$$

The damping term, for example, can be given in the form of a Rayleigh's dissipation function, which is proportional to the generalized velocities

$$R = \frac{\alpha \mu_0 M_s}{2\gamma_0} \left(\dot{\theta}^2 + \dot{\varphi}^2 \sin^2 \theta \right) .$$

2.1.4 Energies of a ferromagnet

Magnetization dynamics are determined by the effective magnetic field \mathbf{H}_{eff} in the sample. This field is the derivative of the free magnetic energy over the direction of the magnetization. Later on, it is used to determine the frequency of the magnetization precession.

The magnetization is oriented in such a way, that all energy contributions to the free magnetic energy are reduced. The most important contributions, such as exchange energy, anisotropy energy, stray field energy and Zeeman energy are presented in the following sections[1, 4].

Exchange Energy

The tendency of spins to align themselves parallel or antiparallel to each other is attributed to the exchange interaction. This originates from the Columb

interaction between electrons and the antisymmetry of the wave function given by the Pauli principle. The exchange interaction is described by the Heisenberg Hamiltonian H_{ex} , which is given by:

$$H_{ex} = - \sum_{i,j=1} J_{ij} S_i S_j , \quad (2.14)$$

where J_{ij} denotes the exchange integral and S_i are spin operators. The parallel alignment of the spins in the ferromagnet is the energetically favorable configuration, due to the negative value of the exchange integral. By increasing the distance between the atoms, the value of J_{ij} decreases rapidly. Therefore, a good approximation of the sum in Eq. 2.14 may consider only the nearest neighbors. In that case, a value for the exchange integral $J_{ij} = J$ can be derived from the Weiss classical molecular field theory:

$$J = \frac{3kT_C}{2zS(S+1)} , \quad (2.15)$$

where T_C denotes the Curie temperature, z the number of nearest neighbors and S the total spin number. Nevertheless, by replacing the summation in Eq. 2.14 by an integral over the ferromagnetic sample, the following expression for the energy of the exchange interaction is derived:

$$E_{ex} = A \int_V (\nabla \mathbf{m})^2 d^3 \mathbf{r} , \quad (2.16)$$

where \mathbf{m} is a continuously defined vector quantity. The exchange constant A is the material constant, expressed by the exchange integral J :

$$A = \frac{2JS^2}{a} , \quad (2.17)$$

where a denotes the lattice constant.

The Heisenberg Hamiltonian is completely isotropic and its energy levels do not depend on the direction in space in which the crystal is magnetized.

Magneto-crystalline Anisotropy Energy

The energy of a ferromagnet depends on the direction of the magnetization relative to the structural axes of the material. There are different types of anisotropy which contribute to the free energy of the ferromagnet, such as magneto-crystalline anisotropy, shape anisotropy and magneto-elastic anisotropy. The shape anisotropy is often considered as demagnetization energy and will be presented in the next section. The anisotropy energy is usually small compared to the exchange energy. Nevertheless, the direction of the magnetization is determined only by the anisotropy in absence of an external magnetic field. The exchange interaction just tries to align the magnetic moments, regardless of direction.

The most common type of anisotropy is magnetocrystalline anisotropy, which is caused by the spin-orbit interaction of the electrons due to the reorientation

of orbitals and the creation of crystallographic axes. In hexagonal crystals with out-of-plane anisotropy the magnetic anisotropy energy can be expressed as:

$$E_{ani} = \int_V (-K_1 m_z^2 - K_2 m_z^4) d^3 \mathbf{r} \quad (2.18)$$

Terms of higher order, and in most cases even K_2 are negligible:

- if $K_1 > 0$, then the crystallographic z axis is an easy axis, which means it is a direction of minimal energy

- if $K_1 < 0$, then the crystallographic z axis is a hard axis with an easy plane perpendicular to it.

Stray Field Energy

Stray field energy is also known as magnetostatic energy, demagnetization field energy or shape anisotropy energy. It has its origin in the classical interactions between the magnetic dipoles, in particular, within the interaction of the magnetization in the magnetic field of the sample itself. Gauss's law for the magnetic flux density \mathbf{B} is given by:

$$\text{div} \mathbf{B} = \text{div} \mu_0 (\mathbf{H} + \mathbf{M}) = 0 . \quad (2.19)$$

The stray field H_d can be defined as divergence of the magnetization:

$$\text{div} \mathbf{H}_d = -\text{div} \mathbf{M} . \quad (2.20)$$

The energy attributed to the demagnetization field is then given by:

$$E_d = \frac{1}{2} \mu_0 \int_{all\ space} \mathbf{H}_d^2 d^3 \mathbf{r} = -\frac{1}{2} \mu_0 \int_{sample} \mathbf{M} \cdot \mathbf{H}_d d^3 \mathbf{r} . \quad (2.21)$$

The stray field energy is always positive as it is shown by the first integral in Eq. 2.21.

In the approximation of given magnetic charge densities, the stray field energy can be derived from the volume charge density ρ_v and the surface charge density σ_s , given by:

$$\rho_v = -\text{div} \mathbf{m} , \quad \sigma_s = \mathbf{m} \cdot \mathbf{n} , \quad (2.22)$$

where \mathbf{n} is the outward directed surface normal. The potential of the stray field is then defined as:

$$\Phi_d(\mathbf{r}) = \frac{M_s}{4\pi} \left(\int_V \frac{\rho_v(\mathbf{r}')}{|\mathbf{r} - \mathbf{r}'|} d^3 \mathbf{r}' + \int_S \frac{\sigma_s(\mathbf{r}')}{|\mathbf{r} - \mathbf{r}'|} d^2 \mathbf{r}' \right) , \quad (2.23)$$

which leads to the stray field $\mathbf{H}_d(\mathbf{r}) = -\text{grad} \Phi_d(\mathbf{r})$. Therewith, the demagnetization field energy is given by the volume and surface integral as

$$E_d = \mu_0 M_s \left(\int_V \rho_v(\mathbf{r}) \Phi_d(\mathbf{r}) d^3 \mathbf{r} + \int_S \sigma_s(\mathbf{r}) \Phi_d(\mathbf{r}) d^2 \mathbf{r} \right) . \quad (2.24)$$

Two important implications of Eq. 2.24 light up the main difference between stray field energy and exchange energy. In contrast to the exchange interaction energy, which only depends on the nearest neighbors, the demagnetization energy is characterized by the entire sample. Second, E_d is proportional to the saturation magnetization M_d , as opposed to the exchange energy which scales with the exchange constant A . This causes domain formation with closure magnetization to be more energetically favorable with regard to the single domain states.

To simplify the calculation of the stray field energy the demagnetization tensor N is introduced. The stray field can be then expressed as:

$$\mathbf{H}_d = -\mathbf{N} \cdot \mathbf{M} . \quad (2.25)$$

The demagnetization tensor is determined by the geometry of the sample. In case of the homogeneously magnetized ellipsoids, the demagnetizing tensor is a diagonal matrix. The simplest form of N is given for the thin homogeneously magnetized plate in xy -plane with only one non-zero component, $N_{zz} = 1$. In this case, the stray field energy is given by:

$$E_d = -\frac{1}{2}\mu_0 M_s^2 . \quad (2.26)$$

Zeeman Energy

The interaction of the magnetization and the external field H gives the Zeeman energy. In general, it is:

$$E_Z = -\mu_0 \int_V \mathbf{M} \cdot \mathbf{H} d^3\mathbf{r} . \quad (2.27)$$

This term is important for the magnetic excitations caused by the external field. The magnetization will align with the external field, when H overcomes the contributions from the crystalline-anisotropy and demagnetization fields.

2.2 Derivation of $\omega(H)$

To analyze the frequencies observed in our pump-probe experiment, the dispersion relation for different precession modes has to be deduced. At first, the case without magnetic damping is considered for simplicity. For various precession modes, different contributions to the free magnetic energy are considered, from which the effective magnetic field and the corresponding frequency dispersion relation are deduced.

This section derives the Landau-Lifshitz-Gilbert equation in spherical coordinates. From this derivation, the frequency of the magnetic precession is related to the derivatives of the free magnetic energy. From there, the frequency dispersion relations for the Kittel $k = 0$ mode and for the standing spin-wave mode are deduced.

The Kittel mode is the basic mode in which the magnetization is homogeneous within the entire sample. It is characterized by the wavevector $k = 0$. This is the dominant relaxation channel for the magnetization precession in the presence of external magnetic field \mathbf{H} . In this case, Zeeman, stray field and crystalline anisotropy energy contribution to the free magnetic energy are considered.

For the case of the standing spin waves, magnetic moments precess coherently with a constant phase shift between neighboring spins. This mode has been also observed in our experiments. The spin wave is characterized by a wavevector $k \neq 0$. The exchange interaction is explicitly included in deriving the magnon dispersion relation. The solutions for a wavevector \mathbf{k} are then analyzed for specific boundary conditions.

2.2.1 Landau-Lifshitz equation in spherical coordinates

To derive the general expression for frequency dependence on the external magnetic field by both amplitude and orientations relative to the sample magnetization, we first derive the Landau-Lifshitz equation in a more applicable form. The LL equation of motion in macrospin approximation,

$$\frac{d\mathbf{M}}{dt} = -\gamma\mu_0\mathbf{M} \times \mathbf{H}_{eff} , \quad (2.28)$$

can be derived with the spherical coordinates[5] schematically presented in Fig. 2.2, related to the magnetization vector \mathbf{M} .

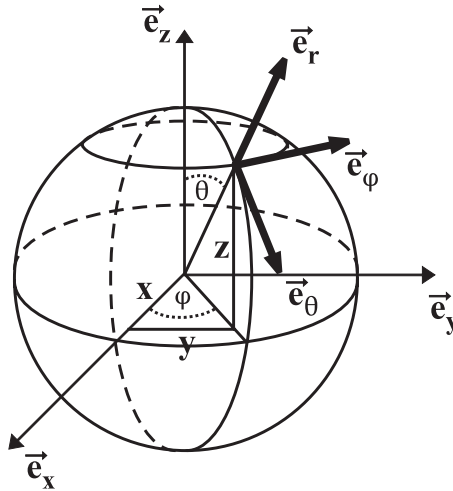


Figure 2.2: Spherical coordinate system.

The infinitesimal small change of the magnetization vector is then expressed by:

$$d\mathbf{M} = M_s dr\mathbf{e}_r + M_s d\theta\mathbf{e}_\theta + M_s \sin\theta d\varphi\mathbf{e}_\varphi , \quad (2.29)$$

where M_s denotes saturation magnetization, and θ and φ denote the polar and azimuthal angle of \mathbf{M} in the Cartesian coordinate system. The effective

magnetic field H_{eff} can be expressed in spherical coordinates using the following expression:

$$\begin{aligned} \mathbf{H}_{eff} &= -\frac{1}{\mu_0 M_s} \frac{\partial F}{\partial \mathbf{m}} \\ &= -\frac{1}{\mu_0} \left(\frac{\partial F}{\partial r} \mathbf{e}_r + \frac{1}{M_s} \frac{\partial F}{\partial \theta} \mathbf{e}_\theta + \frac{1}{M_s \sin \theta} \frac{\partial F}{\partial \varphi} \right) \end{aligned}$$

The left and right hand side in the Landau Lifshitz equation Eq. 2.28 can then be expressed as:

$$\begin{aligned} \frac{d\mathbf{M}}{dt} &= M_s \frac{d\theta}{dt} \mathbf{e}_\theta + M_s \sin \theta \frac{d\varphi}{dt} \mathbf{e}_\varphi \\ \mathbf{M} \times \mathbf{H}_{eff} &= \frac{1}{\mu_0 \sin \theta} \frac{\partial F}{\partial \varphi} \mathbf{e}_\theta - \frac{1}{\mu_0} \frac{\partial F}{\partial \theta} \mathbf{e}_\varphi, \end{aligned}$$

which leads to the Landau-Lifshitz equation in spherical coordinates:

$$\begin{aligned} \frac{d\theta}{dt} &= -\frac{\gamma}{M_s \sin \theta} \frac{\partial F}{\partial \varphi} \\ \frac{d\varphi}{dt} &= \frac{\gamma}{M_s \sin \theta} \frac{\partial F}{\partial \theta}. \end{aligned}$$

For the small variations around the equilibrium position, the free energy F can be converted to a Taylor series, in which the first approximation is given by:

$$F = F_0 + \frac{1}{2} (F_{\theta\theta}\theta^2 + 2F_{\theta\varphi}\theta\varphi + F_{\varphi\varphi}\varphi^2). \quad (2.30)$$

The equations of motion for the azimuthal and polar angle of the magnetization then become:

$$\frac{d\theta}{dt} = -\frac{\gamma}{M_s \sin \theta} (F_{\theta\varphi}\theta + F_{\varphi\varphi}\varphi) \quad (2.31)$$

$$\frac{d\varphi}{dt} = \frac{\gamma}{M_s \sin \theta} (F_{\theta\theta}\theta + F_{\theta\varphi}\varphi) \quad (2.32)$$

The θ and φ , which satisfy the previous sets of equations, are given by the small harmonic oscillations around the equilibrium values, θ_0 and φ_0 :

$$\theta - \theta_0 = \theta_A \exp(-i\omega t)$$

$$\varphi - \varphi_0 = \varphi_A \exp(-i\omega t),$$

where θ_A and φ_A denote the amplitude of those precessions. The previous expressions are incorporated into Eq. 2.31 and Eq. 2.32 to derive the following set of equations:

$$\begin{aligned} \left(\frac{\gamma F_{\theta\varphi}}{M_s \sin \theta} - i\omega \right) \theta + \frac{\gamma F_{\varphi\varphi}}{M_s \sin \theta} \varphi &= 0 \\ \frac{\gamma F_{\theta\theta}}{M_s \sin \theta} \theta + \left(\frac{\gamma F_{\theta\varphi}}{M_s \sin \theta} + i\omega \right) \varphi &= 0. \end{aligned}$$

The non-trivial solution to the homogeneous system given by the previous equations exists only when the following condition is satisfied:

$$\omega = \frac{\gamma}{M_s \sin \theta} \sqrt{\frac{\partial^2 F}{\partial \theta^2} \cdot \frac{\partial^2 F}{\partial \varphi^2} - \left(\frac{\partial^2 F}{\partial \theta \partial \varphi} \right)^2} \quad (2.33)$$

The precession frequency is given by the partial derivatives of the free magnetic energy with respect to the azimuthal and polar angle of the magnetization \mathbf{M} at their equilibrium values. This formula is used later on to determine the frequency dispersion relation for different magnetic precession modes.

2.2.2 Derivation of the Kittel formula

In all-optical pump-probe experiments the thermally induced anisotropy field pulse triggers the magnetization precession in the GHz range. However, the precession frequency is determined by the stationary effective magnetic field \mathbf{H}_{eff} . For the homogeneously precessing magnetization described by the Kittel $k = 0$ mode, the free magnetic energy is composed of the crystalline anisotropy, the demagnetization field and the Zeeman term. In spherical coordinates, with respect to the magnetization vector \mathbf{M} , the free magnetic energy F can be expressed as follows:

$$\begin{aligned} F = & - K_x \sin^2 \theta \cos^2 \varphi - K_y \sin^2 \theta \sin^2 \varphi - K_z \cos^2 \theta \quad (2.34) \\ & - \mu_0 M_s (H_x \sin \theta \cos \varphi + H_y \sin \theta \sin \varphi + H_z \cos \theta) \\ & + \frac{1}{2} \mu_0 M_s^2 \cos^2 \theta . \end{aligned}$$

The relevant partial derivatives which contribute to the precession frequency (see Eq. 2.33) have to be taken at the equilibrium orientation of the magnetization. The orientation of the magnetization can be estimated by comparing the involved magnetic interactions. In our experiment the maximum external field applied is $\mu_0 H_x = 150\text{mT}$ in-plane and $\mu_0 H_z = 70\text{mT}$ out-of-plane. The small thickness of the sample implies that the demagnetization field determines the easy axis of the magnetization in-plane. The Zeeman term rotates the magnetization at a maximum of 7° out-of-plane. Due to the absence of significant in-plane anisotropies, the magnetization is mostly aligned with the x-component of the external field, H_x . Hence, the partial derivatives in Eq. 2.33 are given by:

$$\begin{aligned} \frac{\partial^2 F}{\partial \theta^2} \Big|_{\varphi=0} &= (-2K_x + 2K_z - \mu_0 M_s^2) \cos 2\theta + \mu_0 M_s (H_x \sin \theta + H_z \cos \theta) \\ \frac{\partial^2 F}{\partial \varphi^2} \Big|_{\varphi=0} &= (2K_x - 2K_y) \sin^2 \theta + \mu_0 M_s H_x \sin \theta \\ \frac{\partial^2 F}{\partial \theta \partial \varphi} \Big|_{\varphi=0, H_y=0} &= 0 . \end{aligned}$$

The frequency of the magnetization precession, in which the magnetization is canted for angle θ in respect to the sample normal, can be expressed as:

$$\omega = \frac{\gamma}{\sin \theta} \cdot \sqrt{\left(-\frac{2K_x}{M_s} + \frac{2K_z}{M_s} - \mu_0 M_s\right) \cos 2\theta + \mu_0 H_x \sin \theta + \mu_0 H_z \cos \theta} \cdot \sqrt{\left(\frac{2K_x}{M_s} - \frac{2K_y}{M_s}\right) \sin^2 \theta + \mu_0 H_x \sin \theta} . \quad (2.35)$$

In the absence of external fields no precession is observed which implies that $K_x \approx K_y$. There is no significant in-plane anisotropy in our sample, therefore one can assume that $K_z \gg K_x$. By considering the realistic case with $\theta \approx \pi/2$, Eq. 2.35 is further simplified to the following expression:

$$\omega = \gamma \sqrt{\mu_0 H_x \left(\mu_0 H_x + \mu_0 M_s - \frac{2K_z}{M_s}\right)} \quad (2.36)$$

The saturation magnetization of the transition metals is $\mu_0 M_s = 659\text{mT}$ for nickel, $\mu_0 M_s = 2190\text{mT}$ for iron and $\mu_0 M_s = 1833\text{mT}$ for cobalt.

The frequency dispersion relation, given by Eq. 2.36, is the Kittel formula and describes the homogeneously rotating magnetization ($k = 0$) within the entire sample. When the amplitude of the external field is systematically varied, the Kittel formula can be used to fit the frequency spectrum and to determine the corresponding out-of-plane anisotropy constant K_z .

2.2.3 Derivation of the magnon dispersion relation

Besides the volume homogeneous magnetization mode, in which all spins behave as one macrospin, there are spin-wave modes, which do not obey homogeneous precession in the entire sample. Due to the large cross section of our samples, the spin waves which propagate laterally from the area under the pump laser spot are not important on the ns-timescale[6]. The experimentally observed standing spin waves are attributed to the spin waves which propagate perpendicular to the sample surface. The spin waves, excited at the sample surface, travel through the sample into the substrate, where they are reflected and returned back to the surface. Under special geometrical conditions for the propagating spin vector \mathbf{k} , standing spin waves can form. Fig. 2.3 shows the standing spin waves of the main order and higher orders with open and fixed boundary conditions.

The frequency of the exchange interaction dominated modes, such as the standing spin waves, cannot be described by the Kittel formula derived in the previous chapter. To derive the frequency distribution of the spin-wave modes, the exchange interaction has to be explicitly included in the free magnetic energy. The contribution of the exchange interaction to the free energy F is taken directly from the magnetization vector \mathbf{M} by:

$$F_{ex} = \frac{A}{M_s^2} \left((\nabla M_x)^2 + (\nabla M_y)^2 + (\nabla M_z)^2 \right) \quad (2.37)$$

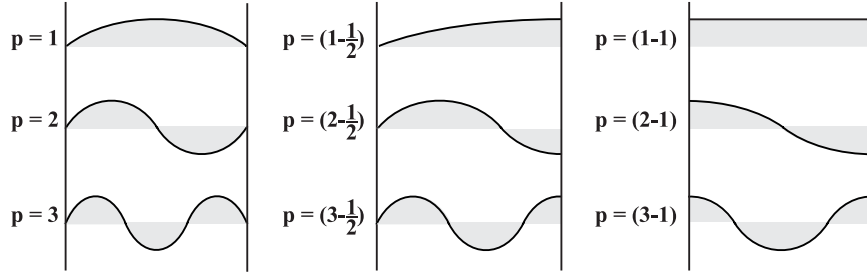


Figure 2.3: Standing spin waves of different order with open and fixed boundary conditions[7].

In our experiments, the magnetization oscillates in the yz -plane, while the external field keeps the magnetization aligned with the x -direction. The magnetization can be represented by a plane wave $\exp(-i(\omega t - \mathbf{k} \cdot \mathbf{r}))$ at the position \mathbf{r} with the wavevector \mathbf{k} . Nevertheless, for the case of thin films, only waves that travel perpendicular to the sample plane are important. Therefore, the magnetization vector is given by:

$$\mathbf{M} = \text{Re} \begin{pmatrix} \hat{M}_x \\ \hat{M}_y \exp(-i(\omega t - kz)) \\ \hat{M}_z \exp(-i(\omega t - kz)) \end{pmatrix}, \hat{M}_x \cong M_s, \hat{M}_z = i\hat{M}_y, \hat{M}_y \in \Re. \quad (2.38)$$

One has to keep in mind how the standing spin wave is formed within the sample. Open boundary conditions correspond to the maximum radius of the precessing magnetization at the sample surface. There is no pinning of the spins in the interface with the substrate. Therefore, the open boundary conditions for the spin waves are expected on both interfaces. For the magnetization vector \mathbf{M} defined by the Eq. 2.38, the precession amplitude is given with:

$$M_y^2 + M_z^2 = \hat{M}_y^2 = \text{const}(t, z)$$

The precession amplitude is constant within the entire sample. The spin wave described by the Eq. 2.38 is shown in Fig. 2.4 a). It is the appropriate presentation of the magnetization vector of the usual propagating spin wave, but not of the standing spin wave. Fig. 2.4b) shows the standing spin wave with open boundary condition and node in the middle. The corresponding magnetization vector \mathbf{M} is:

$$\mathbf{M} = \text{Re} \begin{pmatrix} \hat{M}_x \\ \hat{M}_y \exp(-i\omega t) \cos kz \\ \hat{M}_z \exp(-i\omega t) \cos kz \end{pmatrix}, \hat{M}_x \cong M_s, \hat{M}_z = i\hat{M}_y, \hat{M}_y \in \Re. \quad (2.39)$$

In this case, the amplitude of the magnetization precession varies with thickness,

with maximum value at the sample surface:

$$\begin{aligned} M_y^2 + M_z^2 &= \hat{M}_y^2 \cos^2 kz = \text{const}(t) \\ M_y^2 + M_z^2 &\stackrel{z=0}{=} \hat{M}_y^2 . \end{aligned}$$

The open boundary conditions determine a value for the k-vector $k = \pi n/d$, for n th order standing spin wave.

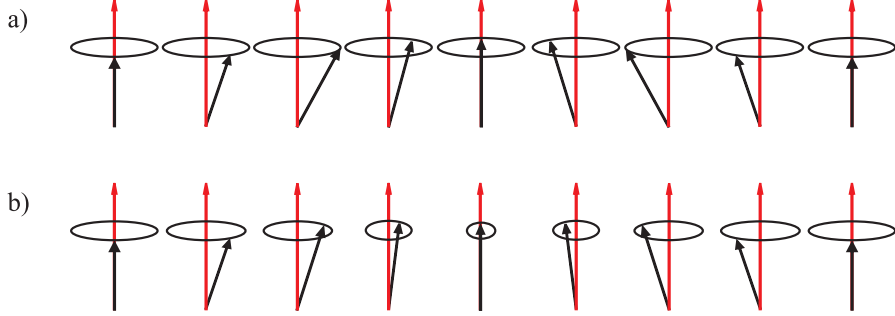


Figure 2.4: Schematical view of the propagating and standing spin waves.

Once the magnetization vector \mathbf{M} is known, the contribution of the exchange interaction to the magnetic free energy, defined by Eq. 2.37, can be calculated:

$$\begin{aligned} F_{ex} &= \frac{A}{M_s^2} \left(0 + k^2 \left(\hat{M}_y^2 \cos^2 \omega t - M_y^2 \right) + k^2 \left(\hat{M}_y^2 \sin^2 \omega t - M_z^2 \right) \right) \\ &= \frac{A}{M_s^2} \left(k^2 \hat{M}_y^2 - k^2 (M_y^2 + M_z^2) \right) \\ &= \underbrace{\frac{A}{M_s^2} k^2 \hat{M}_y^2}_{const} - k^2 A (m_y^2 + m_z^2) . \end{aligned}$$

The precession frequency is then deduced from the total free magnetic energy comprised from F_{ex} and the free energy given by Eq. 2.34. The relevant partial derivatives with respect to the spherical coordinates are:

$$\begin{aligned} \frac{\partial^2 F}{\partial \theta^2} \Big|_{\varphi=0} &= (-2K_x + 2K_z - \mu_0 M_s^2 + 2k^2 A) \cos 2\theta + \mu_0 M_s (H_x \sin \theta + H_z \cos \theta) \\ \frac{\partial^2 F}{\partial \varphi^2} \Big|_{\varphi=0} &= (2K_x - 2K_y - 2k^2 A) \sin^2 \theta + \mu_0 M_s H_x \sin \theta \\ \frac{\partial^2 F}{\partial \theta \partial \varphi} \Big|_{\varphi=0, H_y=0} &= 0 . \end{aligned}$$

Therewith, the precession frequency of the standing spin wave, with the realistic approximation that $\theta \approx \pi/2$, and neglecting the in-plane anisotropies, is given by:

$$\omega = \gamma \sqrt{\left(\mu_0 H_x - \frac{2k^2 A}{M_s} \right) \left(\mu_0 H_x + \mu_0 M_s - \frac{2K_z}{M_s} - \frac{2k^2 A}{M_s} \right)} . \quad (2.40)$$

This depends on the amplitude of the external field, the value of the out-of-plane anisotropy and the exchange constant. When the value of K_z is determined by fitting the main $k = 0$ mode with the Kittel formula, the value of $2k^2A/M_s$ can be found by fitting the frequency spectra of the standing spin waves in Eq. 2.40. The modulus of the $|k|$ vector can be determined from the geometrical conditions. The value of the exchange constant A can then be derived directly from the experiments.

2.3 Derivation of $\alpha(\tau_\alpha)$

To compare the magnetic damping from different experiments and experimental configurations in regard of strength and orientation of the external field, it is important to determine the dimensionless Gilbert damping parameter α . In time resolved measurements, magnetic damping is signaturred in the characteristic exponential decay time τ_α of the amplitude of the magnetization precession. This section derives the relation between the damping parameter α and the decay time τ_α for the Kittel $k = 0$ mode and the standing spin-wave mode. For this purpose the Landau-Lifshitz-Gilbert equation

$$\frac{d\mathbf{M}}{dt} = -\gamma\mu_0\mathbf{M} \times \mathbf{H}_{eff} + \frac{\alpha}{M_s}\mathbf{M} \times \frac{d\mathbf{M}}{dt} \quad (2.41)$$

is linearized for the corresponding effective magnetic field H_{eff} for each of the precession modes.

The system of three coupled differential equations derived from linearization of the LLG equation can be simplified by considering only those magnetization components that contribute to the precession. For thin films the magnetization is mainly in-plane, so $M_z \ll \sqrt{M_x^2 + M_y^2}$. The external magnetic field H is applied in the xz -plane. Therefore, we can assume that the magnetization \mathbf{M} is aligned with the x -direction, with a small precession in the yz -plane: $M_y, M_z \ll M_x \cong 1$. In this case, the equations for motion of the precessing magnetization components are:

$$\dot{M}_y = -\gamma\mu_0 (M_z H_{eff,x} - M_s H_{eff,z}) - \alpha \dot{M}_z \quad (2.42)$$

$$\dot{M}_z = -\gamma\mu_0 (M_s H_{eff,y} - M_y H_{eff,x}) + \alpha \dot{M}_y . \quad (2.43)$$

To further determine the dynamic of the magnetization vector from the system of coupled linear differential equations, the effective magnetic field H_{eff} has to be explicitly known. Therefore, two separate cases are considered: one corresponding to the Kittel $k = 0$ mode and one to the standing spin-wave mode.

2.3.1 α versus τ_α for Kittel mode

The free magnetic energy of the ferromagnet in the external field H comprises the Zeeman energy, the demagnetization field energy and the crystalline

anisotropy term. It can generally be assumed that anisotropy in all three directions, described by the anisotropy constants K_x , K_y and K_z , is present. The following expression holds for the free magnetic energy F :

$$\begin{aligned} F = & - K_x m_x^2 - K_y m_y^2 - K_z m_z^2 \\ & - \mu_0 M_s (H_x m_x + H_y m_y + H_z m_z) \\ & + \frac{1}{2} \mu_0 M_s^2 m_z^2, \end{aligned} \quad (2.44)$$

where $\mathbf{m} = (m_x, m_y, m_z)$ denotes the magnetization unit vector. The effective magnetic field H_{eff} is then derived as

$$\mathbf{H}_{eff} = -\frac{1}{\mu_0 M_s} \frac{\partial F}{\partial \mathbf{m}} \quad (2.45)$$

$$\Rightarrow \mathbf{H}_{eff} = \begin{pmatrix} H_x + \frac{2K_x}{\mu_0 M_s} m_x \\ H_y + \frac{2K_y}{\mu_0 M_s} m_y \\ H_z + \left(\frac{2K_z}{\mu_0 M_s} - M_s \right) m_z \end{pmatrix}. \quad (2.46)$$

The equations of motions for the M_y and M_z magnetization components are:

$$\dot{M}_y = \gamma \mu_0 M_s H_z - \gamma \mu_0 \left(H_x + \frac{2K_x}{\mu_0 M_s} - \frac{2K_z}{\mu_0 M_s} + M_s \right) M_z - \alpha \dot{M}_z \quad (2.47)$$

$$\dot{M}_z = \gamma \mu_0 \left(H_x - \frac{2K_y}{\mu_0 M_s} + \frac{2K_x}{\mu_0 M_s} \right) M_y + \alpha \dot{M}_y. \quad (2.48)$$

One of the methods to solve the coupled linear differential equations for continuous functions is to make time derivative of higher order and then conceive one of the variables over the others. Due to the continuous trajectories of the precessing magnetization vector, the time derivative of the previous equation can be taken to derive the relations:

$$\ddot{M}_y = -\gamma \mu_0 \left(H_x + \frac{2K_x}{\mu_0 M_s} - \frac{2K_z}{\mu_0 M_s} + M_s \right) \dot{M}_z - \alpha \ddot{M}_z \quad (2.49)$$

$$\ddot{M}_z = \gamma \mu_0 \left(H_x - \frac{2K_y}{\mu_0 M_s} + \frac{2K_x}{\mu_0 M_s} \right) \dot{M}_y + \alpha \ddot{M}_y. \quad (2.50)$$

During precession, the end of the magnetization vector lies on a circle in the yz -plane and the solutions $M_z(t)$ and $M_y(t)$ of the coupled different equations Eq. 2.47 and Eq. 2.48 differ only in phase. Later on, only the equation of motion for the M_y component is considered:

$$\begin{aligned} (1 + \alpha^2) \ddot{M}_y + \alpha \gamma \mu_0 \left(2H_x + \frac{4K_x}{\mu_0 M_s} - \frac{2K_y}{\mu_0 M_s} - \frac{2K_z}{\mu_0 M_s} + M_s \right) \dot{M}_y + \\ + (\gamma \mu_0)^2 \left(H_x + \frac{2K_x}{\mu_0 M_s} - \frac{2K_z}{\mu_0 M_s} + M_s \right) \left(H_x + \frac{2K_x}{\mu_0 M_s} - \frac{2K_y}{\mu_0 M_s} \right) M_y = 0. \end{aligned}$$

The assumed solution is:

$$M_y = M_y^0 \exp(-i\omega t) e^{-t/\tau_\alpha} , \quad (2.51)$$

where ω denotes the angular frequency of the precessing magnetization and τ_α the characteristic exponential decay time. The imaginary part of the previous equation is zero, therefore

$$(\alpha^2 + 1) \frac{2i\omega}{\tau_\alpha} - i\omega\alpha\gamma\mu_0 \left(2H_x + \frac{4K_x}{\mu_0 M_s} - \frac{2K_y}{\mu_0 M_s} - \frac{2K_z}{\mu_0 M_s} + M_s \right) = 0 . \quad (2.52)$$

The solution of the previous quadratic equation for α is:

$$\alpha = \frac{1}{2} \left(\frac{\tau_\alpha\gamma\mu_0 H'}{2} \pm \sqrt{\left(\frac{\tau_\alpha\gamma\mu_0 H'}{2} \right)^2 - 4} \right) , \quad (2.53)$$

with the constant H'

$$H' = 2H_x + \frac{4K_x}{\mu_0 M_s} - \frac{2K_y}{\mu_0 M_s} - \frac{2K_z}{\mu_0 M_s} + M_s . \quad (2.54)$$

The value of $\tau_\alpha\gamma\mu_0 H'$ is much larger than 1 for our experimental conditions. Therefore, the solution to Eq. 2.53 with the + sign leads to $\alpha \gg 1$, which implies that the magnetization precession is overdamped. This is opposite to our experimental findings. Therefore, only the solution with the - sign is relevant in this case. With the above introduced H' , the damping parameter α is determined by:

$$\alpha = \left(\tau_\alpha\gamma\mu_0 \left(H_x + \frac{2K_x}{\mu_0 M_s} - \frac{K_y}{\mu_0 M_s} - \frac{K_z}{\mu_0 M_s} + \frac{M_s}{2} \right) \right)^{-1} . \quad (2.55)$$

Samples investigated in this work don't have pronounced in-plane anisotropy, therefore the K_x and K_y constants can be neglected and a simpler expression used to calculate α :

$$\alpha = \left(\tau_\alpha\gamma\mu_0 \left(H_x - \frac{K_z}{\mu_0 M_s} + \frac{M_s}{2} \right) \right)^{-1} . \quad (2.56)$$

Eq. 2.56 is not applicable when the out-of-plane anisotropy constant K_z is unknown. Therefore, the measurement of the frequency spectra of the Kittel mode is required to determine the damping parameter. In the limit of high external fields, the anisotropy contribution to the frequency dispersion can be neglected, so the damping parameter is inversely dependent on the precession frequency:

$$\alpha = (\tau_\alpha\omega)^{-1} . \quad (2.57)$$

2.3.2 α versus τ_α for standing spin-wave mode

This section derives the damping parameter α of the standing spin-wave mode from the exponential decay time τ_α . The effective magnetic field is derived from the free magnetic energy, which is the sum of expressions given by Eq. 2.44 and Eq. 2.37:

$$\mathbf{H}_{eff} = -\frac{1}{\mu_0 M_s} \frac{\partial(F + F_{ex})}{\partial \mathbf{m}} \quad (2.58)$$

$$\Rightarrow \mathbf{H}_{eff} = \begin{pmatrix} H_x + \frac{2K_x}{\mu_0 M_s} m_x \\ H_y + \frac{2K_y + 2k^2 A}{\mu_0 M_s} m_y \\ H_z + \left(\frac{2K_z + 2k^2 A}{\mu_0 M_s} - M_s \right) m_z \end{pmatrix}. \quad (2.59)$$

Applying the same procedure as that for the Kittel mode, the following expression is derived for the damping parameter of the standing spin-wave mode:

$$\alpha = \left(\tau_\alpha \gamma \mu_0 \left(H_x + \frac{2K_x}{\mu_0 M_s} - \frac{K_y}{\mu_0 M_s} - \frac{K_z}{\mu_0 M_s} - \frac{2k^2 A}{M_s} + \frac{M_s}{2} \right) \right)^{-1}. \quad (2.60)$$

The in-plane anisotropy constants can be neglected for the samples investigated within this work, which leads to the final formula to determine α for the standing spin-wave mode:

$$\alpha = \left(\tau_\alpha \gamma \mu_0 \left(H_x - \frac{K_z}{\mu_0 M_s} - \frac{2k^2 A}{M_s} + \frac{M_s}{2} \right) \right)^{-1}. \quad (2.61)$$

To apply the Eq. 2.61 the out-of-plane anisotropy constant K_z and exchange constant A must be known. Again, the frequency spectra of the Kittel and standing spin-wave mode are required to determine the damping parameter α of the standing spin-wave mode.

CHAPTER 3

Experimental technique

This chapter presents the details of the experimental technique the all-optical pump-probe approach that allow access the magnetization dynamics on time scales from 100fs to a few ns. Beginning introduces a small overview of the measurement techniques used to investigate the magnetization dynamics in general. Thereafter, is an introduction to the all-optical pump-probe approach with a special focus on the excitation mechanisms of the magnetization dynamics and the origin of the magneto-optical Kerr effect. There is then a detailed description of the experimental setup, the measurement procedure, the femtosecond laser system and the electromagnet. The final remarks in this chapter regard the samples, their deposition and characterization.

3.1 Methods for investigating magnetization dynamics

Magnetization dynamics is an intriguing field of magnetism with a number of open questions. The term magnetization dynamics mainly stands for a magnetization precession, during which the magnetization vector aligns with the external field. The characteristic timescales of the magnetization processes are approaching the technological limit for magnetic devices. Therefore, the relevance of the fundamental timescales of the magnetization relaxation goes from theoretical to practical research.

In the experiments, the magnetization is first taken out of equilibrium, and its relaxation to the equilibrium position is recorded. Due to the timescale of these processes, it is possible to separate the near-adiabatic processes, which occur on a timescale from several picoseconds up to nanoseconds, and the strongly non-adiabatic processes, which occur on a timescale from a femtosecond up

to picoseconds after the excitation. The near-adiabatic processes include long wavelength spin waves, dynamics of the domain walls, and field- and current-induced magnetization switching. To measure magnetization dynamics at these timescales, the following techniques are used: Kerr microscopy, magnetic transmission X-ray microscopy (MTXM), spin-polarized low-energy electron microscopy (SP-LEEM), spin-polarized photoemission electron microscopy (SP-PEEM), ferromagnetic resonance (FMR) and Brillouin light scattering (BLS). Processes on a even shorter timescale can be investigated by the time-resolved Kerr effect (TR MOKE) or the time resolved photoemission electron spectroscopy (TR PEES).

Different techniques are used to investigate magnetization dynamics. These can be generally classified into techniques on the time scale and techniques on the frequency scale. The most important techniques from each category are presented in the following.

3.1.1 Techniques on the time scale

Techniques owning the highest time resolution are generally based on the stroboscopic principle. Here the intensive excitation by the short laser or the magnetic field pulse triggers the magnetization dynamics. The magnetization relaxation is then recorded after a certain time delay. This kind of measurement belongs to the pump-probe scheme in which the time resolution is achieved by the time delay between pump (denotes excitation) and probe (denotes measurement of the magnetic variable) at the sample.

Time resolved Magneto-Optical Kerr Effect (TR MOKE)

This technique is based on the magnetic contrast from the magneto-optical Kerr effect in the visible light. It denotes the polarization change of the light reflected from a ferromagnetic sample. Due to the spin-orbit coupling, the Kerr angle is proportional to the magnetization of the sample. As a pump mechanism, either short magnetic pulses[8] or an intensive pump-laser pulse can be used, as this work does. The high temporal and spatial resolution given by the microscope optics in these experiments allows a high applicability. A detailed explanation of the experimental setup is given in Section 3.2.

Time resolved second harmonic generation (TR SHG)

This technique is also based on the all-optical approach. It differs from TR MOKE in that the magnetic contrast originates from the nonlinear response of the ferromagnetic sample in an intensive laser field. Due to the large electric fields \mathbf{E} of the laser light, the polarization of the sample \mathbf{P} is not only linearly dependent on the electric field, but also the higher order terms:

$$\mathbf{P} = \epsilon_0 (\chi_1 \times \mathbf{E} + \chi_2 \times \mathbf{E} \times \mathbf{E} + \chi_3 \times \mathbf{E} \times \mathbf{E}) .$$

The susceptibility tensor of the first, second and third order is given by χ_1 , χ_2 and χ_3 respectively.

The generated second-harmonic light with a significant polarization change in comparison to the incident light, even with a small intensity, can be directly related to the electron temperature and the magnetization from the selection rules[9–11].

Time resolved photoemission electron spectroscopy (TR X-PEES)

This technique is analogous to the time-resolved magneto-optical Kerr effect at a shorter wavelength: in the X-ray range. The magnetic circular dichroism (XMCD) reveals the magnetic contrast through X-ray absorption which depends on the relative orientation of the local magnetization and the light's polarization vector. Both the size and the direction of the magnetic moments can be measured element selectively. This magnetic contrast can be used together with an X-ray photoemission electron microscopy (X-PEEM) to spatially map the magnetization of the sample[12]. The time resolution is achieved using a pump-probe scheme, where the magnetic pulses created by a microcoil or strip line are synchronized with the X-ray photon pulses at the repetition rate of the accelerator[13]. The main advantages of this method are the element selectivity and the spatial resolution of 20nm, which is much smaller than that for the optical methods in the visible range. The time resolution of 70ps is limited by the synchrotron characteristics and is significantly larger than in the optical pump-probe experiments[14]. Recently, the femtosecond slicing experiments have been developed in BESSY with the femtosecond X-rays radiation produced from a single electron bunch. This is a powerful technique with a competitive time resolution and the possibility to separately attribute the orbital and magnetic moment during the magnetization relaxation[15].

3.1.2 Techniques on the frequency scale

These techniques follow the magnetization dynamics by measuring the frequencies of the coherent magnetization precession based on spectroscopic principle.

Ferromagnetic Resonance (FMR)

Ferromagnetic resonance can be used to investigate the collective magnetization excitations in the microwave frequency range with a small wavevector. The ferromagnetic resonance absorption is similar to the nuclear resonance absorption with the difference being that FMR probes the magnetic moment of electrons instead of the nucleus. Generally, the effect is based on the optical transitions due to the Zeeman splitting in the microwave range.

A constant external field \mathbf{H}_{dc} is applied using an electromagnet with an amplitude of 1T to initialize the magnetization direction in the sample. In the direction perpendicular to the external field, an alternating magnetic field

$\mathbf{H}_{rf}(t) = \mathbf{H} \exp(i\omega t)$ is applied with the microwave frequency ω and an amplitude significantly smaller than \mathbf{H}_{dc} . The magnetization precesses in the effective magnetic field and the resonant absorption takes place when the frequency of the \mathbf{H}_{rf} equals the magnetization precession frequency. The resonance condition for a plane surface[16] is given by

$$\omega_0 = \gamma \sqrt{\mathbf{B} \cdot \mathbf{H}_{dc}} ,$$

where γ represents the gyromagnetic ratio and \mathbf{B} the magnetic induction in the sample. The ideal ferromagnetic absorption line, as shown in Fig. 3.1, has the

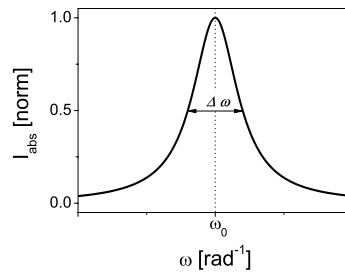


Figure 3.1: Ideal ferromagnetic resonance absorption line.

Lorentzian shape. Its width $\Delta\omega$ can be correlated with the Gilbert damping parameter α with the expression,

$$\Delta\omega = \frac{\alpha\omega}{\gamma\mu_0} ,$$

where μ_0 denotes the vacuum's magnetic permeability. At interfaces between ferromagnetic and nonmagnetic layers, there are additional contributions to the width of the FMR peak which do not originate from the Gilbert damping, but rather from two-magnon scattering[17]. FMR is a powerful tool to determine the precessional eigenmodes of different materials[18, 19]. The damping parameter can be attributed to each precession mode[20]. Due to the measurement of the total magnetization of the sample, this method is also used to determine the enhancement of the Gilbert damping α from the emission of the spin currents[21].

Brillouin Light Scattering (BLS)

This experimental technique can investigate both lattice and magnetic excitations with wavevectors comparable to the wavevector of the applied laser light and frequencies in the GHz range. Due to the conservation of energy and impulse, the photon carries information about the wavevector of the phonon or magnon by which it was scattered. The magnon can be annihilated or created in this scattering process with the same probability as for temperatures higher than $T > 10\text{K}$. Classically, the inelastic scattering of the incident optical wave from spin-orbit coupling causes a phase-grating in the sample, and

the frequency of the scattered light obeys the Doppler shift equal to the spin-wave frequency[22]. The quantum and classical scattering processes are shown in Fig. 3.2. Both surface and volume modes can be measured with this technique. The surface mode is characterized by the different heights of the Stokes and Anti-Stokes peaks, due to limited propagation of magnons at the sample surface.

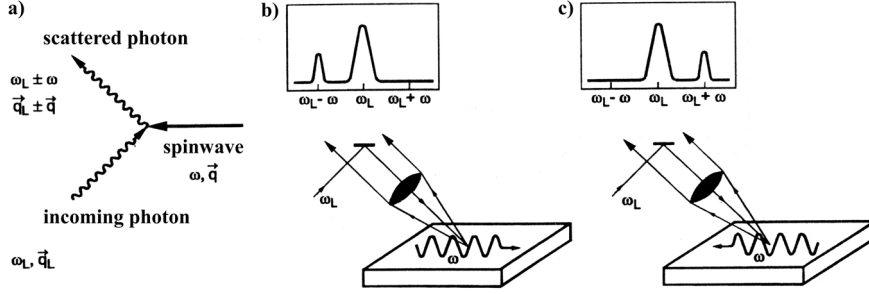


Figure 3.2: Schematical representation of Brillouin light scattering. a) scattering process of phonons at magnons. Inelastic scattering of the light at spin waves: b) magnon and incoming light propagate in the same direction, c) magnon and incoming light propagate in the opposite direction. Both cases are parallel to the sample plane. Figure taken from [22].

To measure the small shift in frequency, the conventional Fabry-Perot-Interferometer has to be improved to achieve the contrast needed to resolve the weak Brillouin doublets. Multipassing was first experimentally realized by Sandercock[23]. This is done by coupling the two synchronized Fabry-Perot-Interferometers, which significantly increases the contrast and thereby prevents overlapping of different orders of interference. The Tandem-Fabry-Perot-Interferometer has a frequency resolution in the sub-GHz range and a contrast better than $1 : 10^{10}$ [24].

Magnetostatic modes have been investigated *in situ* using BLS and are reported in detail in [25]. Due to the focused laser light, spatially resolved measurements can also be made with BLS. This technique is also used to investigate dipolar Damon-Eschbach modes and spatially localized spin waves on structured ferromagnetic films[26, 27].

3.2 All-optical pump-probe experiments

As mentioned in the previous section, the pump-probe technique uses a pump pulse to excite the sample, and a probe pulse to detect the sample relaxation. By varying the time delay relative to the pump pulse, time resolved measurements are possible. In an all-optical pump-probe scheme both the sample excitation and the detection of the relaxation process is done using laser pulses. Depending on the probe scheme, both the electron dynamics and magnetization dynamics can be recorded. To follow electron relaxation upon laser excitation, time resolved reflectivity is measured. The reflectivity measurements are not

explicitly included in this thesis. The details are published in [28, 29]. The time resolved Kerr effect is measured to follow the magnetization relaxation upon laser excitation.

The intense pump-laser pulse strongly perturbs the ferromagnetic sample. The energy of the pump-laser pulse is transferred to the sample within the pulse duration of $\Delta\tau = 80\text{fs}$. This causes an ultrafast demagnetization of the sample on timescales of $<1\text{ps}$ and triggers the coherent precession of the magnetization on the 100ps timescale. The excitation mechanisms and relevant time scales for both regimes are given in the following sections.

3.2.1 Ultrafast demagnetization

Demagnetization upon laser excitation can be attributed to the increased spin temperature from absorption of the pump-laser pulse. Nevertheless, on timescales of $<1\text{ps}$, the highly non-equilibrium state is a playground of various intensive interactions which challenges both experimentalists and theorists. The demagnetization of the nickel samples was first observed in the all-optical pump-probe experiments by Beaurepaire in [30].

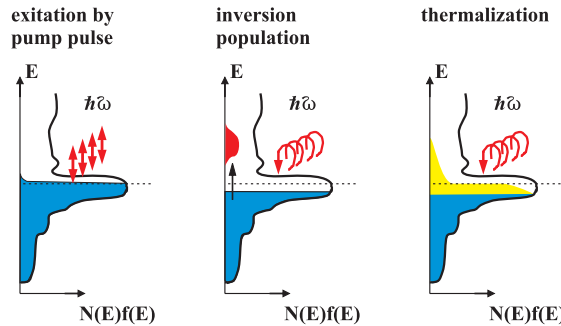


Figure 3.3: Schematical representation of the optical excitation by the pump pulse.

The energy of the pump-laser pulse is first deposited to the electron system, and the further distributed to the phonon and spin system. The excitation process is shown in Fig. 3.3. Before excitation by the intensive pump-laser pulse, the electrons satisfy the Fermi Dirac distribution at temperature T . Exposure to the intensive pump pulse causes optical transitions and induces the inversion of the population of allowed states with the hot electrons. Due to electron-electron scattering, the electron system thermalizes to the Fermi-Dirac distribution at the higher temperature $T + \Delta T$. The energy is then transferred from the thermalized electron system to the lattice and spin system by the electron-phonon and electron-spin scattering processes. The increased sample temperature causes the loss of the ferromagnetic order as shown in Fig. 3.4.

The ultrafast demagnetization and restoration of the ferromagnetic order on the ps timescale upon laser excitation can be described using the Three Tem-

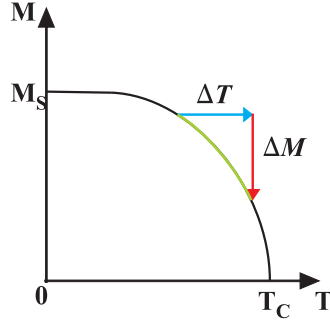


Figure 3.4: Schematical view of the demagnetization, caused by an increase of the sample temperature.

perature model [30, 31]. This model assumes independent electron, lattice and spin baths temperatures of T_e , T_p and T_s , in which the interactions between them are described by the coupling constants g_{ep} , g_{es} and g_{sp} , shown in Fig. 3.5.

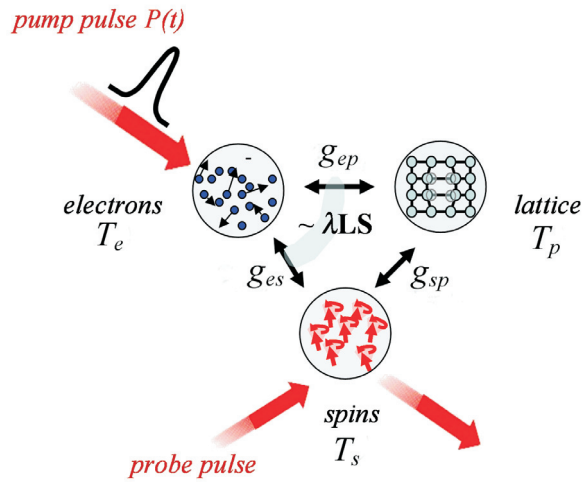


Figure 3.5: Schematical presentation of the three Temperature model. Figure adapted from [32].

The temporal evolution of these temperatures is given by the following system of coupled differential equations:

$$\begin{aligned} C_e(T_e) \frac{dT_e}{dt} &= -g_{ep}(T_e - T_p) - g_{es}(T_e - T_s) + P(t) \\ C_s(T_s) \frac{dT_s}{dt} &= -g_{es}(T_s - T_e) - g_{sp}(T_s - T_p) \\ C_p(T_p) \frac{dT_p}{dt} &= -g_{ep}(T_p - T_e) - g_{sp}(T_s - T_p) , \end{aligned}$$

in which C_e , C_s and C_p represent the heat capacities of the electron, the spin and

phonon system respectively and $P(t)$ denotes the laser field of the pump pulse. A closed-form expression can be given for the differential equation system [28, 32].

3.2.2 Induced magnetization precession

The absorption of the intensive pump-laser pulse not only induces the reduction of the magnetization amplitude, but also changes the easy axis of the system and triggers a precession of the magnetization. This effect was first observed in [32, 33]. The Anisotropy field pulse describes the ps pulse from the sudden temperature rise which starts the precession of the magnetization. The anisotropy field pulse is shown in Fig. 3.6.

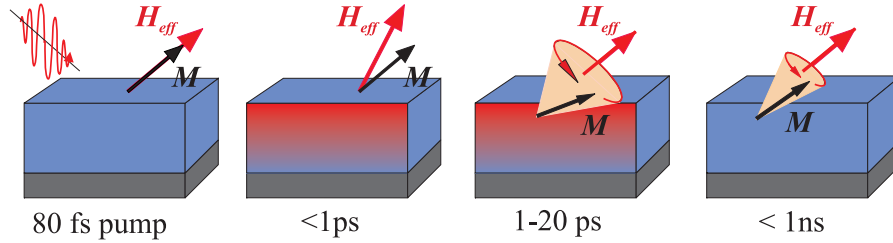


Figure 3.6: Anisotropy field pulse in all-optical pump-probe experiments.

The absorption of the intensive laser pulse will briefly increase the temperature of the sample under the pump-laser spot. This temperature rise changes the anisotropy of the sample and thereby the easy axis of the magnetization, for a couple of ps. The magnetization then starts to precess around the new easy axis with a tendency to align with the new effective field. Nevertheless, the thermally induced anisotropy change takes only a couple of ps, after which the easy axis is returned to the orientation from before the pump laser illuminated the sample. The magnetization, already out of equilibrium, is not aligned with the effective magnetic field and begins to precess around it. The magnetic damping determines the timescale on which the magnetization aligns with the effective field. Therefore, the magnetization precession is determined by the constant effective magnetic field and not by the anisotropy field pulse, which only triggers the magnetization precession and determines the opening angle of the magnetization torque.

3.3 Magneto-optical Kerr Effect

Materials which exhibit magneto-optical phenomena can be separated into two distinct classes by the nature of the interaction. In the first class, the magneto-optical effect results from the direct action of the magnetic field on the orbital motion of the electrons, such as the Faraday effect (polarization change of the transmitted light) or magneto-circular dichroism (different absorption frequen-

cies due to different polarizations). In the second class, the effect results from the direct spin-orbit coupling, known as the Kerr effect (polarization change of reflected light) in ferromagnetic materials. Since spin-orbit interactions are generally 100-1000 times larger than the maximum Zeeman splitting for a typical laboratory experiment, the "magnetic interaction" of the equally aligned spins leads to much larger effects on the orbital motion than the magnetic field itself.

The Kerr effect can be described as a change in the polarization of light reflected from a magnetic sample proportional to the internal magnetization in the sample itself. It originates from different optical absorption coefficients of the material for left and right circularly polarized light. The Kerr effect can be measured in polar, longitudinal and transverse configuration, as shown in Fig. 3.7.

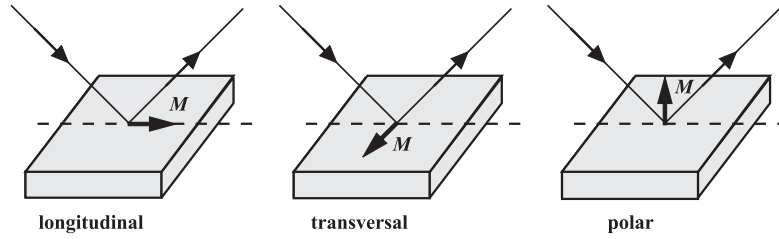


Figure 3.7: Configurations for measurement of the Kerr effect.

Per definition, the magnetic field \mathbf{H} is applied normal to the film plane for the polar Kerr effect. Thus it is sensitive to the perpendicular component of the magnetization. For the longitudinal Kerr effect \mathbf{H} is applied in the film plane and in the plane of the incident light, making it sensitive to the in-plane component of the magnetization. Finally, for the transverse Kerr effect \mathbf{H} is applied in the film plane, but perpendicular to the incident plane of the light. The polar and longitudinal Kerr effects are linear in the magnetization and yield to a complex rotation Θ_K of the polarization of the light. The polar signal is typically an order of magnitude larger than the longitudinal signal because of different optical prefactors.

3.3.1 Phenomenological origin

The optical response of the material is fully described by an optical susceptibility χ , which correlates the induced polarization \mathbf{P} with the electric field, or a dielectric tensor ϵ , which correlates the dielectric displacement \mathbf{D} to the electric field:

$$\begin{aligned} \mathbf{P} &= \chi \mathbf{E} \\ \mathbf{D} &= \epsilon \mathbf{E} \\ \epsilon &= 1 + 4\pi\chi . \end{aligned}$$

The dielectric tensor ϵ can be decomposed into a symmetric and anti-symmetric part[34]. The normal modes of the symmetric part of ϵ are left and right linearly polarized light, which do not contribute to the magneto-optical effects. Therefore, without losing generality, only the dielectric tensor for the isotropic materials is considered:

$$\epsilon = \epsilon_{xx} \begin{pmatrix} 1 & -iQm_z & iQm_y \\ iQm_z & 1 & -iQm_x \\ -iQm_y & iQm_x & 1 \end{pmatrix} .$$

where Q is the magneto-optical constant, defined as $Q = i\epsilon_{xy}/\epsilon_{xx}$ and $\mathbf{m} = (m_x, m_y, m_z)$ is the unit vector of the magnetization vector \mathbf{M} . The normal modes of ϵ are left and right circularly polarized light, with eigenvalues ϵ_L and ϵ_R , given by

$$\begin{aligned} \epsilon_L &= 1 - Q\mathbf{m} \cdot \mathbf{k} \\ \epsilon_R &= 1 + Q\mathbf{m} \cdot \mathbf{k} . \end{aligned}$$

The non-zero difference between those eigenvalues gives rise to magneto-optical effects such as the polarization change of the reflected light from the ferromagnet.

The expression for the Kerr effect is derived from the Fresnel reflection matrix \mathbf{R} , whose off-diagonal terms originate from spin-orbit coupling. In the basis of p - and s - polarized light, the Fresnel matrix is expressed as:

$$\mathbf{R} = \begin{pmatrix} r_{pp} & r_{ps} \\ r_{sp} & r_{ss} \end{pmatrix} .$$

The complex Kerr angle Θ_K for p - and s -polarized light is defined by:

$$\begin{aligned} \Theta_K^s &= \theta_K^s + i\epsilon_K^s = \frac{r_{ps}}{r_{ss}} \\ \Theta_K^p &= \theta_K^p + i\epsilon_K^p = \frac{r_{sp}}{r_{pp}} . \end{aligned}$$

The expression for the Kerr angle has been derived from the previous equations in [35]. Only the final expressions regarding the Kerr angle are presented here for the limit of optical thin magnetic film, shown in Fig. 3.8. The relevant optical parameters are incident and transmitted angles θ_0 , θ_1 and θ_2 and indexes of reflection n_0 , n_1 and n_2 in medium 0, magnetic medium 1 and medium 2. The expressions for the Kerr angle in polar and longitudinal configurations are presented first, followed by those for arbitrary orientation of the magnetization and obliquely incident light.

- Polar configuration ($m_z = 1$, $m_x = m_y = 0$)

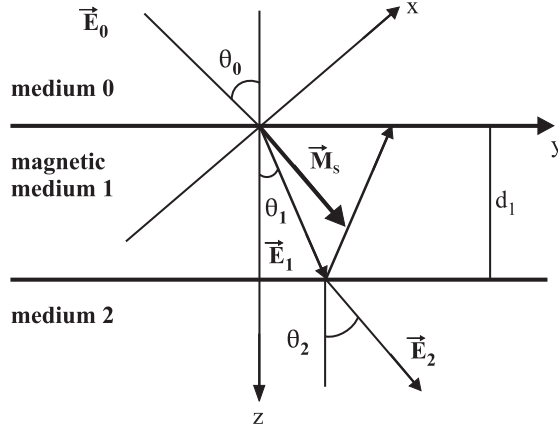


Figure 3.8: Schematical representation of the thin optical film and corresponding optical parameters. Figure taken from [35].

The complex Kerr angle is given by:

$$\Theta_{K,pol}^s = \left(\frac{r_{ps}}{r_{ss}} \right)_{pol} = \frac{-\cos \theta_0}{\cos(\theta_0 - \theta_2)} \cdot \cos \theta_2 \cdot \Xi$$

$$\Theta_{K,pol}^p = \left(\frac{r_{sp}}{r_{pp}} \right)_{pol} = \frac{\cos \theta_0}{\cos(\theta_0 + \theta_2)} \cdot \cos \theta_2 \cdot \Xi ,$$

where Ξ depends on the thickness d of the magnetic medium given by

$$\Xi = \frac{4\pi n_0 n_1^2 Q d}{\lambda (n_2^2 - n_0^2)} .$$

- Longitudinal configuration ($m_y = 1, m_x = m_z = 0$)

The complex Kerr angle is given by:

$$\Theta_{K,long}^s = \left(\frac{r_{ps}}{r_{ss}} \right)_{long} = \frac{\cos \theta_0}{\cos(\theta_0 - \theta_2)} \cdot \frac{\sin^2 \theta_1}{\sin \theta_2} \cdot \Xi$$

$$\Theta_{K,long}^p = \left(\frac{r_{sp}}{r_{pp}} \right)_{long} = \frac{\cos \theta_0}{\cos(\theta_0 + \theta_2)} \cdot \frac{\sin^2 \theta_1}{\sin \theta_2} \cdot \Xi .$$

- General case for the arbitrary magnetization orientation

The complex Kerr angle is given by:

$$\Theta_K^s = \frac{r_{ps}}{r_{ss}} = \frac{\cos \theta_0}{\cos(\theta_0 - \theta_2)} \cdot \left(m_y \frac{\sin^2 \theta_1}{\sin \theta_2} - m_z \cos \theta_2 \right) \cdot \Xi$$

$$\Theta_K^p = \frac{r_{sp}}{r_{pp}} = \frac{\cos \theta_0}{\cos(\theta_0 + \theta_2)} \cdot \left(\frac{m_y \sin^2 \theta_1}{\sin \theta_2} + m_z \cos \theta_2 \right) \cdot \Xi .$$

The experimental results agree with the formula presented for the magneto-optical Kerr effect.

3.3.2 Quantum mechanical origin

This chapter presents the quantum mechanical nature of the Kerr angle based on the microscopic electronic structure and the Fermi Golden rule for optical transitions[36]. Simultaneous occurrence of exchange splitting and spin-orbit coupling in the band structure of the sample causes a non-zero Kerr effect.

The optical transitions between the initial $|i\rangle$ and final state $|f\rangle$ of the ferromagnet, which give rise to the magneto-optical Kerr effect, are given by the off-diagonal component of the imaginary part σ'' of the conductivity tensor σ :

$$\sigma''_{xy}(\omega) = \frac{\pi e^2}{4\hbar\omega m^2 \Omega} \sum_{i,f} f(\epsilon_i)(1 - f(\epsilon_i)) \cdot \left(|\langle i | p_- | f \rangle|^2 - |\langle i | p_+ | f \rangle|^2 \right) \delta(\omega_{fi} - \omega), \quad (3.1)$$

where $p_{\pm} = p_x \pm ip_y$, $f(\epsilon)$ is the Fermi-Dirac function, Ω represents the total volume and $\omega_{fi} = (\epsilon_f - \epsilon_i)/\hbar$. Only vertical optical transitions which satisfy the following selection rules for the dipolar transitions are allowed:

$$\begin{aligned} \Delta l &= \pm 1 \\ \Delta m_l &= \pm 1. \end{aligned}$$

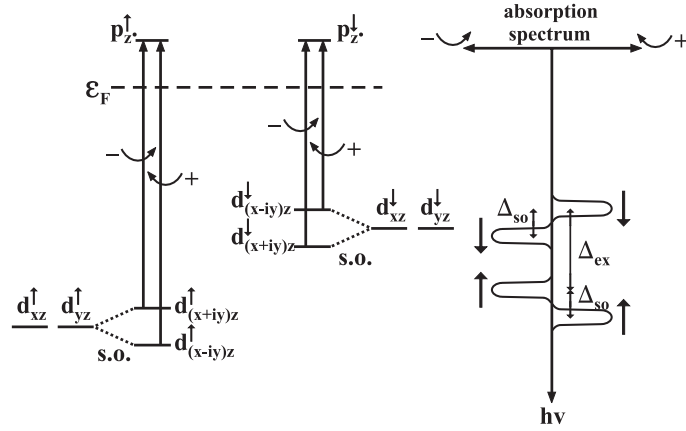


Figure 3.9: Allowed optical transitions for the transition metal ferromagnet and corresponding absorption spectra versus photon energy. Figure taken from [36].

The allowed optical transitions for the transition metal ferromagnet from the $3d$ to $4p$ level are schematically presented in Fig. 3.9. The energy degeneration of the d_{xz} and d_{yz} orbital is removed by spin-orbit coupling for energy Δ_{SO} . The angular momentum carried by the circularly polarized photons is transferred to the electron during the optical transition. The transitions from the d_{x+iy} orbital (having $m_l = 1$) and the d_{x-iy} orbital (having $m_l = -1$) to the p_z orbital (having $m_l = 0$) are excited by the absorption of left and right circularly polarized light, respectively. Due to the exchange interaction, the energy levels

of the $d_{x\pm iy}$ orbital for complementary spin orientations are shifted by the energy Δ_{EX} . The difference in the absorption spectra for the left and right circularly polarized light give rise to the Kerr effect described by Eq. 3.1.

3.4 Measurement setup

This section describes the experimental setup in detail. It first introduces measurement of the Kerr effect by the Photo-Elastic Modulator (PEM) for the various experimental configurations. Next, it describes time resolved magnetic measurements based on the double-modulation technique, in which the intensity of the pump beam and the polarization of the probe beam are modulated. It then briefly describes the femtosecond laser system and makes some final remarks concerning the specification of the electromagnet.

3.4.1 Detection of the Kerr Effect

For most of the ferromagnetic transition metals, the Kerr angle is in the range of a few mdeg. Mainly modulating techniques are used to measure this small polarization change. These techniques modulate the intensity or the polarization of light and record the enhanced magnetic signal with a lock-in amplifier. There are different approaches to measure the Kerr effect, including the crossed polarizer configuration, the balanced photodiodes method or using a photo-elastic modulator. In the first two approaches, the measurement signal is minimized with the polarizing optical elements and the small, intensity modulated signal, proportional to the magnetization of the sample, is recorded. A detailed explanation of those experiments can be found in [37, 38].

The photo-elastic modulator is an active optical element, which is periodically compressed in one direction by a piezo-electric crystal. The changed optical characteristics induce a phase shift for only one polarization component of the light. The PEM is described by a Jones matrix:

$$\mathbf{M} = \begin{pmatrix} e^{iA \sin \omega t} & 0 \\ 0 & 1 \end{pmatrix},$$

where $\omega/2\pi = 50\text{kHz}$ denotes the modulation frequency and $A = \pi/2$ represents the maximum phase shift.

The setup for measurements of the Kerr effect with the PEM is shown in Fig. 3.10. The sample is placed between the poles of the electromagnet, whose field is sufficient to align the magnetic moments of our dominantly in-plane magnetized samples. The linear polarized light under the angle α_P passes through the retardation plate. Depending on the orientation of the optical axis α_M of the retardation plate, the linearly polarized light can be rotated (by a $\lambda/2$ -plate) in polarization or it can be transformed to the elliptically polarized light (by a $\lambda/4$ -plate). The intensity of the reflected beam is measured after it passes

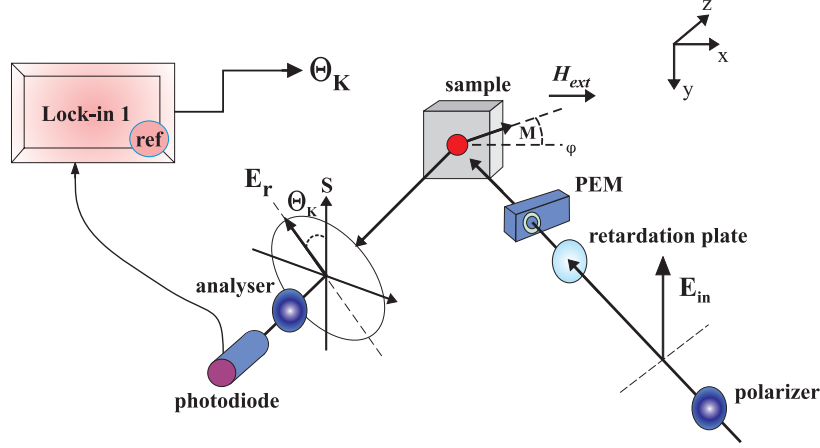


Figure 3.10: Setup for the measurements of the Kerr effect by the PEM.

through the analyzer (oriented at the angle α_A) by a lock-in amplifier. The relative orientation of the polarizer, the retardation plate, the optical axis of the PEM and the analyzer determine the amplitude of the magnetic signal. The measured signal can be analyzed by applying the Jones matrix to the described optical path.

Both Kerr rotation θ_K and Kerr ellipticity ϵ_K can be measured using this technique. The signal I measured by the lock-in amplifier has both a DC and AC contribution:

$$I = I_{DC} + I_{\omega} \cos^2 \omega t + I_{2\omega} \cos^2 2\omega t . \quad (3.2)$$

The following analyzes a brief summary of the final expressions for the measurement signal I for the case when 45° linearly polarized and right circularly polarized light enter the modulator. The details of the derivation procedure can be found in [38, 39].

- 45° linearly polarized light

The measurement signal for the 45° linearly polarized incoming beam, when the optical axis of the polarizer and analyzer are oriented at $\alpha_P = 0^\circ$ and $\alpha_A = 45^\circ$, is given by the following expressions:

$$I_{DC} = R \left(\frac{1}{2} + J_0 \left(\frac{\pi}{2} \right) \theta_K \right) \approx \frac{R}{2}$$

$$I_{\omega} = J_1 \left(\frac{\pi}{2} \right) R \epsilon_K$$

$$I_{2\omega} = J_2 \left(\frac{\pi}{2} \right) R (\theta_K - \rho \alpha_A) .$$

J_n represent the n th order Bessel function, R denotes the reflectivity for s-polarized light and ρ is the ratio of the reflectivity coefficients for p- and s-polarized light. The Kerr rotation is shown in Fig. 3.11.

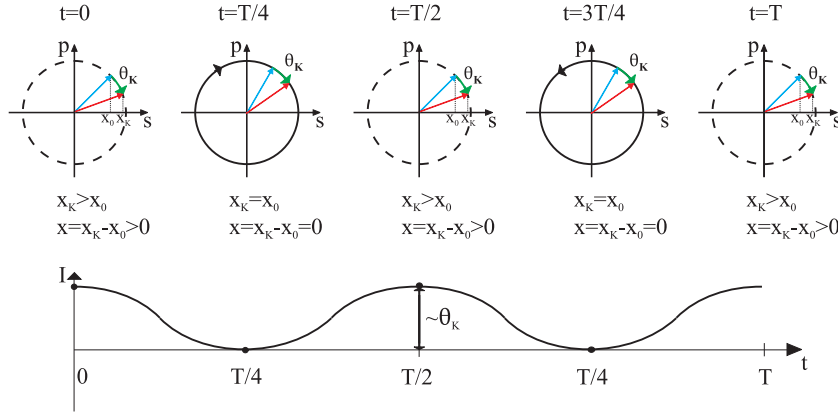


Figure 3.11: Kerr rotation during one oscillation period of the PEM for a 45° linearly polarized incoming beam. Kerr rotation is determined by the amplitude of the modulated signal at 2ω .

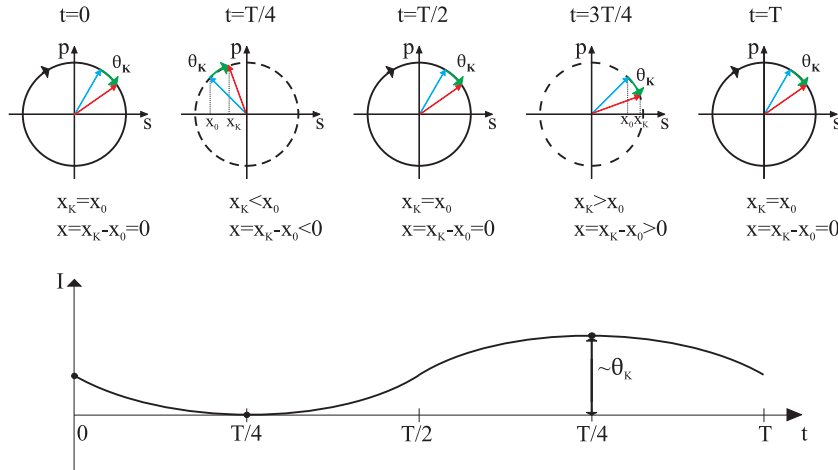


Figure 3.12: Kerr rotation during one oscillation period of the PEM for a right circularly polarized incoming beam. The Kerr rotation is determined by the amplitude of the modulated signal at ω .

- Right circularly polarized light

The measurement signal for a right circularly polarized incoming beam, when the optical axis of the polarizer and analyzer are oriented at $\alpha_P = 0^\circ$ and $\alpha_A = 90^\circ$, is given by the following expressions:

$$I_{dc} = \frac{R}{2}$$

$$I_{1\omega} = J_1\left(\frac{\pi}{2}\right) R(\alpha_A - \theta_K)$$

$$I_{2\omega} = -2J_2\left(\frac{\pi}{2}\right) R\epsilon_K.$$

The Kerr rotation is shown in Fig. 3.12.

3.4.2 Detection of the Time Resolved Kerr Effect

The laser induced magnetization dynamics are measured using the time resolved Kerr effect. The genuine time resolved magnetic signal is extracted with a double-modulation technique: the intensity of the pump beam is modulated by a chopper, and the polarization of the probe beam is modulated by the photo-elastic modulator. 80fs laser pulses with a central wavelength of 800nm, at a 250kHz repetition rate and $1\mu\text{J}$ energy per pulse are used to excite the ferromagnetic sample. A weakened pulse measures the magnetization relaxation.

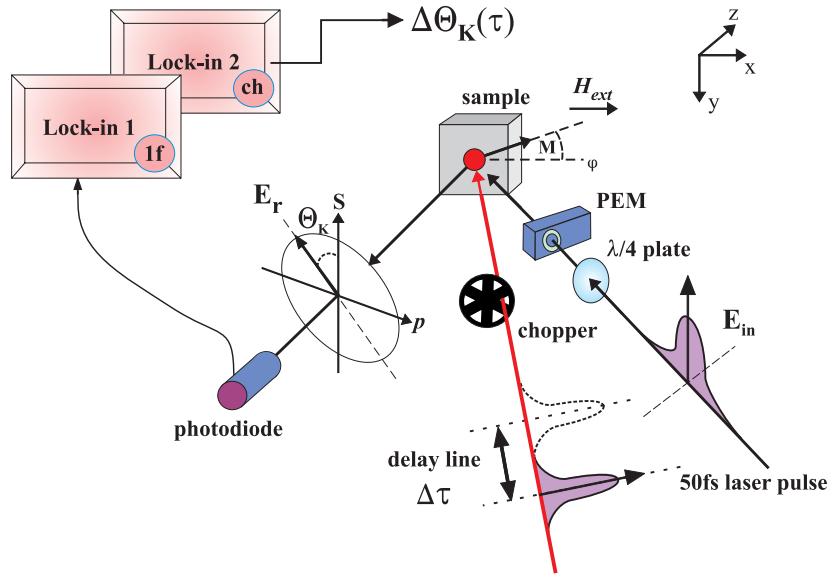


Figure 3.13: Setup for the time resolved magneto-optical Kerr effect.

The laser pulses are divided by a beam splitter into the intensive pump and the weaker probe beams at a ratio of 95:5. The pump pulse impinges orthogonal to the film surface, while probe beam is tilted at an angle of 25° . They are focused to spot sizes of $60\mu\text{m}$ and $30\mu\text{m}$, respectively. The probe pulse obeys the measurement scheme with the PEM, as described in the previous section, in configuration with circularly polarized light. The optical path of the linearly polarized pump pulse is adjustable using the delay stage with a retroreflector. This enables control of the time delay between the pump and the probe pulse. The signal of the photodiode is transferred to the lock-in amplifier with a reference frequency of $\nu_1 = 50\text{kHz}$ equal to the frequency of the modulator, which measures the Kerr rotation θ_K . The output signal from the first lock-in is transferred to the second lock-in amplifier with a reference frequency of $\nu_C = 800\text{Hz}$ equal to the frequency of the chopper. The output signal from the second lock-in amplifier measures the change in the Kerr rotation caused

by the pump beam $\Delta\theta_K(t)$. The sensitivity and time constant of both lock-in amplifiers are adjusted to achieve a maximal magnetic signal. An overview of lock-in specifications and measured variables is given in Tab. 3.1.

	ν_{ref}	Δt	V_{max}	variable
Lock-in 1	50kHz	10 μ s	20mV	θ_K
Lock-in 2	800Hz	100ms	100mV	$\Delta\theta_K$

Table 3.1: Lock-in specifications for the time resolved measurements: ν_{ref} is a reference frequency, Δt is a time constant and V_{max} denotes sensitivity. The first lock-in amplifier measures the Kerr rotation θ_K of the sample. The second measures the change in the Kerr rotation $\Delta\theta_K$ induced by the pump pulse.

The double-modulation technique has already been used in other all-optical pump-probe experiments[32, 38] using pulses with repetition rate of 80MHz. Our experiment has used the PEM with pulses at a repetition rate of 250kHz for an amplified Ti:Sapphire laser system.

The biggest problem in time resolved magnetic measurements is separating the magnetic signal from the pure optical contribution from the reflectivity[40]. Using the double-modulation technique, the non-polarized reflectivity contribution to the measurement signal is eliminated by the first lock-in, which measures the polarization modulated probe beam. The completely asymmetric signal relative to the orientation change of the external magnetic field implies that the magnetic contribution is the dominant factor in the measurement signal.

3.4.3 Femtosecond laser system

The femtosecond laser system in our laboratory comprises the self-built Ti:Sapphire oscillator[41, 42] and a commercial regenerative amplifier RegA 9030, both optically pumped by the solid state Verdi V18 laser. The solid state Verdi V18 laser, developed by Coherent, is one of the leading continuous wave lasers because of its large outgoing power of 18W at 514nm. The thermal and spatial stability of the outgoing beam in comparison with gas lasers, such as the *Argon*⁺ laser, is strongly enhanced. Due to the effective absorption of the Ti:Sapphire crystal, 5.2W are used to pump the Ti:Sapphire oscillator and 11.3W are directed into the RegA system.

The Ti:Sapphire oscillator, based on passive Kerr mode locking, produces 50fs pulses at $\lambda_c = 800$ nm at a repetition rate of 80MHz. The energy per pulse is approximately 1nJ, which is not enough to excite the ferromagnetic sample. Therefore, the pulses from the Ti:Sapphire oscillator are amplified with a regenerative amplifier by factor of 1000. To prevent damage of the optical elements at the amplification stage, the femtosecond pulses are first expanded in time to ps pulses and then amplified. At the end of the amplification stage, the pulses are compressed back to the femtosecond range. The regenerative amplifier model RegA 9030 from Coherent uses an active mode locked (by Q-switch) cavity at 250kHz to build up the amplified pulse seeded by the Ti:Sapphire

from the master oscillator[43]. The amplified Ti:Sapphire 80fs pulses at 800nm at a repetition rate of 250kHz have an energy of approximately $1\mu\text{J}$ per pulse. This energy is sufficient for the all-optical pump-probe experiments described in the following Chapters.

3.4.4 Electromagnet

The self-built electromagnet, which is used in our experiments, was constructed in the Central Mechanical Workshop at the Physics Faculty of University of Göttingen. This electromagnet can adjust the orientation of the external magnetic field by almost 360° relative to the sample surface without changing the pump-probe optics configuration.

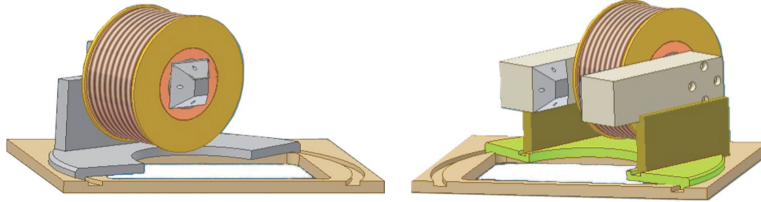


Figure 3.14: The self-built electromagnet in monopole (polar) and two-pole (longitudinal) configuration.

The electromagnet consists of a soft iron core surrounded by coils for the electrical current. A cylindrical reservoir of copper with cooling water is placed between the iron core and the coils to reduce the heat load at the coils. The electromagnet can be used in both polar and longitudinal configuration as shown in Fig. 3.14. In the longitudinal configuration two rectangular iron parts are added to close the magnetic field lines. In the polar configuration, the magnetic field lines are open at one end and directed out of the pole. The electromagnet is placed on a plate, which can be rotated up to 50° in each direction around the sample holder. This allows the orientation of the external field to vary by almost 360° relative to the sample surface.

The strength of the induced magnetic field was characterized by Hall probe measurements at the sample position. The dependence of the magnetic field amplitude on the electrical current through the coils is shown in Fig. 3.15. The linear dependence of the magnetic field is 7mT/A for the polar and 20mT/A for the longitudinal configuration. Magnetic fields of up to 90mT and up to 200mT can be induced in the polar and in the longitudinal configurations, respectively. For current densities higher than 10A , the cooling system of the coils is not efficient enough and the electromagnet heats up. In the longitudinal configuration, the magnetic field strength saturates at electrical currents larger than $I > 9\text{A}$.

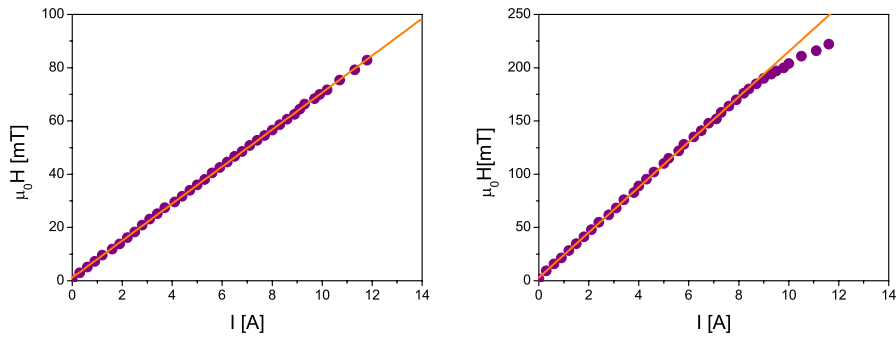


Figure 3.15: The current characteristics of the electromagnet: a) polar configuration, b) longitudinal configuration. The measurement points are fitted with the linear function.

3.5 Samples

This work investigates the magnetization dynamics of thin polycrystalline ferromagnetic samples upon laser excitation. Double layers ferromagnet/normal metal with varied thickness of the ferromagnetic layer were grown specifically to observe the spin pumping effect. All samples investigated in this thesis are made by our group.

The samples are grown by electron-beam evaporation in a UHV chamber with a base pressure of approximately $5 \cdot 10^{-10}$ mbar at room temperature. Low deposition rates of 0.1-0.5 Å/s are applied to increase the quality of the growth, by allowing diffusion on the film surface during the deposition process itself. The layers are deposited on a naturally oxidized silicon substrate (100). Due to the large pump fluencies used in the experiments, a high thermal conductivity of the substrate is a crucial prerequisite.

Fig. 3.16 is a schematical overview of the deposited samples. In general, the nickel layers are deposited with thicknesses from 2nm to 150nm. The non-magnetic layers with palladium, chromium, dysprosium, titanium, aluminum and copper are deposited with a thickness of 5nm. To prevent oxidation, a capping layer of 2-3nm copper or 2nm aluminum is deposited on top of the sample.

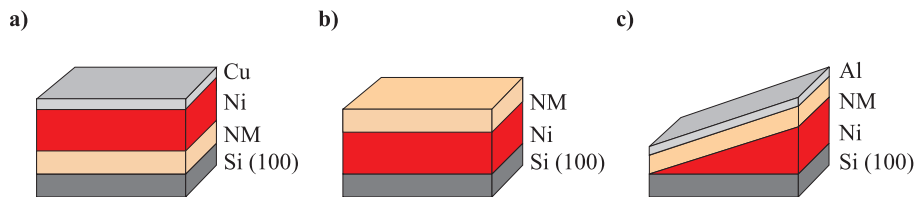


Figure 3.16: Schematical presentation of the multilayer samples: a),b) individual samples, c) wedge sample.

In order to have similar excitation by the pump pulse, the first set of samples is made with a nickel layer deposited on top of the normal metal layer. A comparison of the damping parameter for different Ni/NM samples reveals, that interface roughness and defects in growth of the nickel layer have a strong influence on the measurements. Therefore, a new set of samples was made with the nickel layer deposited directly on the silicon substrate and the normal metal layer on top. This ensures that the growth quality of nickel is similar for all samples.

To increase the homogeneity of the samples with varied ferromagnetic layer thickness and to avoid the slight differences in the growth conditions, a wedge sample is grown. This makes a nickel layer with comparable growth quality on the entire sample at various thicknesses. To prevent strong thickness variations within the laser spot, an extra long wedge sample is grown. The nickel layer with a varying thickness from 2nm to 60nm is made by slowly and continuously moving the shutter during the deposition on the 8mm length. This makes sure that the thickness variation of the investigated region defined by the $60\mu\text{m}$ laser spot is not larger than 0.4nm. The thickness profile of the nickel layer is confirmed by reflectivity measurements. A point of significant change in the optical constants of the silicon substrate and the sample itself determines the mark at which the wedge sample starts. Thereafter, the thickness of the nickel layer is extrapolated by assuming a monotone increase in the thickness of the entire wedge sample also monitored during growth with the shutter manipulation program. Fig. 3.17 shows the reflectivity coefficient for the Si/Ni/Al wedge sample as a function of thickness of the nickel layer. In the reflectivity spectrum the wedge shaped nickel layer can be easily recognized for thicknesses smaller than the optical penetration depth of the laser.

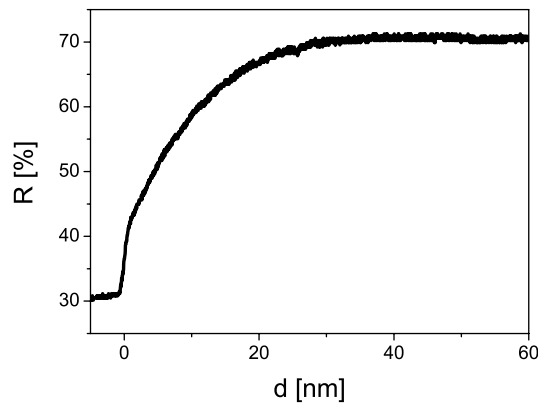


Figure 3.17: Reflectivity coefficient for the Si(100)/xnmNi/2nmAl wedge sample versus thickness of the nickel layer.

3.5.1 XRD characterization

The quality and smoothness of the surface and the interfaces are validated by the standard low angle X-ray reflectivity measurements. For small scattering angles, the intensity of the scattered X-rays contains information on the contrast in the scattering densities of the layer interfaces. This makes interface roughness and interdiffusion accessible. The XRD measurements are performed on the Bruker AXS D8 diffractometer in the First Institute of Physics at University of Göttingen.

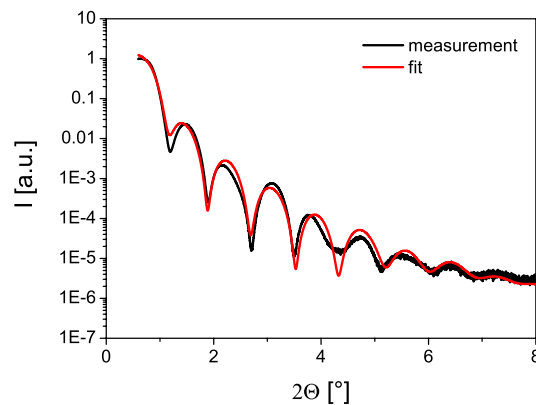


Figure 3.18: Low angle X-ray measurements and corresponding fit for the Si(100)/5nmCr/2nmNi/2nmCu sample.

The interface roughness of the various samples is characterized using this technique. The following discusses the characterization for one of the thinnest samples using low angle X-ray measurements. Fig. 3.18 shows the low angle X-ray measurements of a Si(100)/5nmCr/2nmNi/2nmCu sample. Due to the similar optical density of Cr and Ni in the X-ray range and the small thickness of each layer, the oscillation period mainly mirrors the CrNi double layer. The roughness of each layer can be determined by fitting the measurement data, as it done by fitting program Parratt32 and presented in Fig 3.18. The fit agrees well with the measurement data and reproduces all the important features. Tab. 3.2 lists the fit parameters

layer	Si	Cr	Ni	Cu
thickness	-	5nm	2nm	2nm
fit:thickness	-	5.7nm	2.2nm	2.4nm
fit:roughness	0.1nm	0.4nm	0.4nm	0.5nm

Table 3.2: Thickness specifications and fit parameters for the Si(100)/5nmCr/2nmNi/2nmCu sample.

3 Experimental technique

These data lead to the conclusion that roughness, even for the thinnest samples of the nickel layer, is not larger than 3-5Å. The interface roughness is significantly reduced for thicker layers.

CHAPTER 4

Ultrafast demagnetization

Only time resolved techniques can explore the magnetization dynamics down to the fs scale. The all-optical pump-probe approach using the Kerr effect is one of the most applicable of these techniques, in which the ferromagnetic sample loses its ferromagnetic order due to the absorption of the laser pulse on timescales of 100fs. The ultrafast demagnetization of the nickel layer was first observed in time resolved Kerr effect measurements by Beaurepaire[30], when they observed a sharp drop in the Kerr signal within a few hundred fs after the pump pulse was absorbed. Ultrafast demagnetization was explained by the thermalization of the electron, spin and phonon baths within the Three Temperature model. Later van Kampen showed that the Kerr effect cannot be directly interpreted as the genuine signature of magnetization before the electrons and lattice reach thermal equilibrium, because of optical bleaching[32, 33]. The theoretical calculations devoted to the electronic redistributions during the absorption of the intensive pump-laser pulse made by Oppeneer also concluded that optical bleaching in the first few hundred fs after excitation influences the magneto-optical Kerr effect[44]. On the other hand, measurements with time resolved second harmonic generation by Hohlfeld showed that spin temperature, which obeys the classical $M(T)$ curve, is established for delay times longer than the thermalization of the electron system[10]. The maximum of the demagnetization peak is observed before electron thermalization is complete. Similarly, Guidoni has shown that the magneto-optical Kerr signal mirrors the spin dynamics after the thermalization time of the electrons[45]. After ten years of research, the time resolved magnetization signal in the highly non-equilibrium state of the first ps after excitation by the pump pulse is still not completely understood.

This chapter presents experimental findings on ultrafast demagnetization of the

thin nickel films upon laser excitation. The beginning investigates the influence of the external magnetic fields and the pump fluencies on the demagnetization process. Then it covers microscopical simulations based on the oomf code which agree surprisingly well with measured time resolved spectra even at timescales smaller than 10ps. Finally, a theoretical explanation of the observed relaxation times is suggested. Some parts of this chapter are published in [46].

4.1 Variation of the external magnetic field

This section investigates dependence of the demagnetization process on the external magnetic field. The absorption of the intensive pump-laser pulse by a ferromagnet causes a highly non-equilibrium state in the electron and spin system. The thermal energy, which the laser pulse transfers to the electrons is dominantly higher than the Zeeman energy in an external magnetic field. Therefore, it is expected that the external magnetic field does not influence the demagnetization spectra. To the contrary, our experiments showed that the external magnetic field strongly influences the magnetization relaxation even during the first 5ps after excitation by a pump-laser pulse.

Fig. 4.1 shows time resolved spectra for the Si(100)/5nmCu/50nmNi/3nmCu

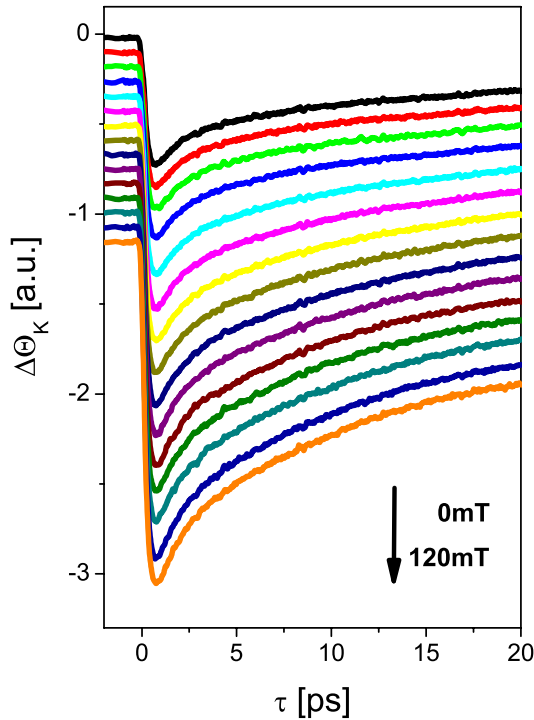


Figure 4.1: Time resolved spectra for the Si(100)/5nmCu/50nmNi/3nmCu sample at $0\text{mT} < \mu_0 H = 120\text{mT}$, $\varphi(H) = 25^\circ$ and $F_{\text{pump}} = 50\text{mJ}/\text{cm}^2$. The spectra are vertically shifted for clarity.

sample, in which the external magnetic field is varied from 0mT up to 120mT. The demagnetization peak depends strongly on the amplitude of the applied external field. When the external field increases, the magnetization relaxation is characterized by a larger demagnetization peak since the polar magnetization component also increases.

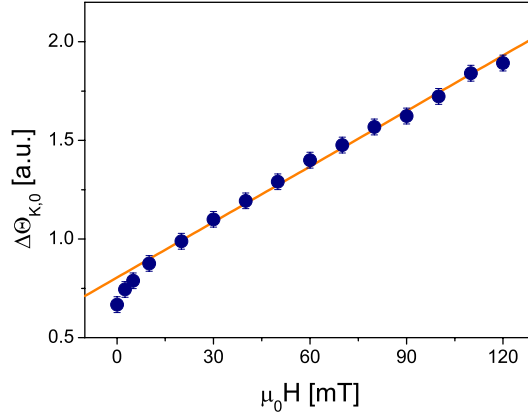


Figure 4.2: Demagnetization peak for the Si(100)/5nmCu/50nmNi/3nmCu sample at $0\text{mT} < \mu_0 H = 120\text{mT}$, $\varphi(H) = 25^\circ$ and $F_{pump} = 50\text{mJ}/\text{cm}^2$.

Fig. 4.2 plots the height of the demagnetization peak, extracted from the time resolved measurements, versus the amplitude of the external field. The linear dependence of the demagnetization peak on the amplitude of the applied external field can then be observed. The height of the demagnetization peak is smaller than the linearly extrapolated one only for external fields smaller than the saturation field $\mu_0 H_s \approx 7\text{mT}$. This dependence implies the magnetic nature of the magneto-optical Kerr signal even at timescales $< 1\text{ps}$ after excitation by a pump laser.

A similar effect is observed for all sample thicknesses. This means that an alignment of the magnetic moments with the external field during the demagnetization from absorption of the pump pulse is still important.

4.2 Variation of the pump fluence

This section investigates the dependence of the demagnetization process on the pump fluence. To control demagnetization of the ferromagnetic layer caused by absorption of the pump pulse, the laser fluence is varied systematically from $20\text{mJ}/\text{cm}^2$ to $60\text{mJ}/\text{cm}^2$. Fig. 4.3 presents the time resolved spectra for the Si(100)/5nmCu/50nmNi/3nmCu sample in which the pump fluence is varied and the external field of $\mu_0 H = 80\text{mT}$ is oriented $\varphi(H) = 25^\circ$ out-of-plane. The spectra are normalized to one and shifted vertically for clarity. For moderate pump fluencies the magnetization recovers within 3ps after the excitation.

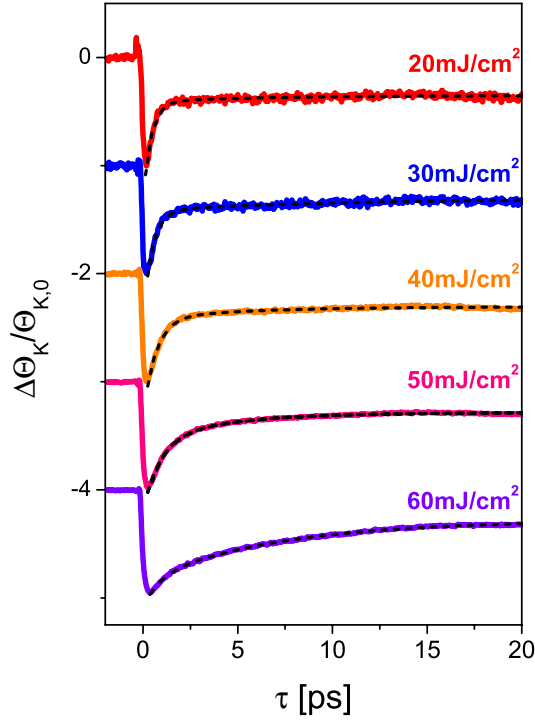


Figure 4.3: Time resolved spectra for the Si(100)/5nmCu/50nmNi/3nmCu sample at $\mu_0 H = 80\text{mT}$, $\varphi(\mathbf{H}) = 25^\circ$ and $20\text{mJ/cm}^2 < F_{\text{pump}} < 60\text{mJ/cm}^2$. The spectra are normalized and vertically shifted for clarity.

When the pump fluencies are larger than 50mJ/cm^2 , the remagnetization happens more slowly.

The time resolved spectra are fitted with the double exponential function, which includes two remagnetization times τ_1 and τ_2 . Tab. 4.1 lists the fitting results. Ultrafast relaxation dominates the remagnetization spectra for small pump fluencies on a 100fs timescale. Relaxation time varies from 420fs to 780fs, slightly increasing with the pump fluence. By increasing the pump fluence to over 50mJ/cm^2 , the slower remagnetization component with the decay times from

fluence [mJ/cm^2]	τ_1 [fs]	τ_2 [ps]
20	420	-
30	450	-
50	800	4.4
60	780	7.1

Table 4.1: Analysis of the restoration of the time-resolved Kerr rotation in the measured time resolved spectra, using two remagnetization times τ_1 and τ_1 .

4ps to 7ps contribute to the measurement signal. This additional decay time for highly perturbed systems is also observed for thinner samples at moderate pump fluencies and high external fields. To model the time resolved spectra for various pump fluencies, the remagnetization process is reproduced using micromagnetic simulations using a oommf code[47].

4.3 Modeling by micromagnetic simulations

The micromagnetic simulations can be used to follow the magnetization dynamics in a given effective field using the Landau-Lifshitz-Gilbert equation. The sample characteristics are incorporated by taking the appropriate terms of the magnetic energy, such as the anisotropy constant, the demagnetization field and the Zeeman term, and by defining the Gilbert damping parameter. With an appropriate temporal and spatial resolution micromagnetic simulations can describe the magnetization dynamics even in complicated structures. The details of the micromagnetic simulation principles can be found in [6, 42, 48, 49].

The demagnetization process itself is not included in the model. The highly non-equilibrium state resulting from the absorption of the pump pulse is represented

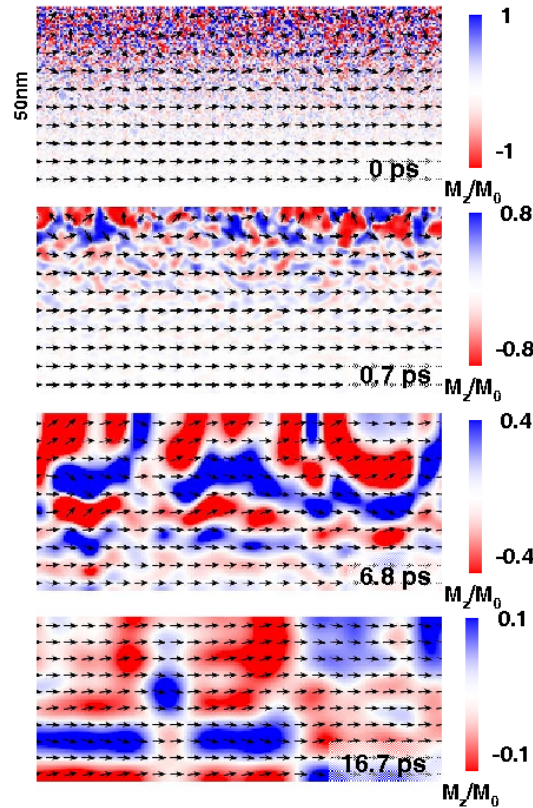


Figure 4.4: Micromagnetic simulation for a 50nm nickel film which is demagnetized 55%. The evolution of the remagnetization is shown at 0ps, 0.7ps, 6.8ps and 16.7ps after excitation.

by the randomly oriented magnetic moments at the sample surface below a thickness equal to the optical penetration depth λ_{opt} . The excitation rate can be implemented into the simulations by introducing a starting demagnetization rate at $\tau=0$. For $\tau > 0$ the simulations are driven in the corresponding effective field and no further heat transfer is introduced. Even though the temperatures, which the ferromagnet reaches during the absorption of the pump pulses, can approach the Curie temperature, the demagnetized surface layer describes the thermally induced demagnetization observed in the experiment well.

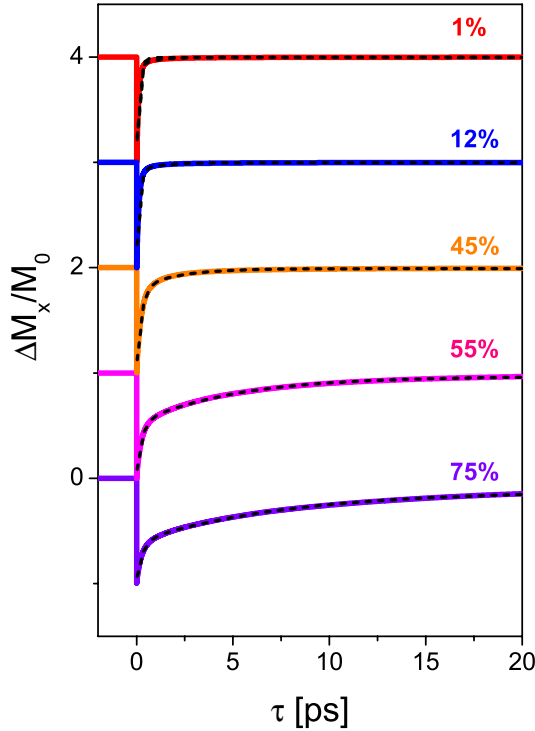


Figure 4.5: Micromagnetic simulation of the relaxation of the M_x magnetization component for a 50nm nickel film with various demagnetization rates. The spectra are normalized and vertically shifted for clarity.

Fig. 4.4 shows the microscopical cut through the by-plane for the 50nm nickel sample at time delays of 0ps, 0.7ps, 6.8ps and 16.7ps after excitation by the pump pulse. The demagnetization profile at zero delay mirrors the penetration profile of the laser light that decays exponentially on a length scale of $\lambda_{opt} = 25\text{nm}$. The surface layer is characterized by the grainy profile and the gradual change of the demagnetization. As the time evolves, small domains form and spin waves emanate from the excited surface. At a time scale of 700fs, domains in the range of 3-6nm have formed already. The spin-wave front has penetrated the entire film thickness of 50nm after 6.8ps. The long wavelength excitations with a typical wavelength of 15-20nm dominate the upper part of the film, while the dominating wavelength is much smaller, on the order

of 5nm, in the lower part. As the spin wave travels back and forth, standing waves are observed at a time delay of 16.7ps.

Fig. 4.5 plots the time resolved spectra of the magnetization component M_x versus delay time for various demagnetization rates. Similarly to the experimental results for different pump fluencies, the ferromagnetic order is recovered within a couple of ps at a moderate demagnetization rate. By increasing the demagnetization rate to more than 50%, much larger remagnetization times contribute to the signal. The time resolved spectra can be fitted with the double exponential function:

$$\frac{M}{M_0} = \eta \frac{\exp(-\tau/\tau_1) + \gamma \exp(-\tau/\tau_2)}{1 + \gamma}, \quad (4.1)$$

Where η denotes the degree of the demagnetization and γ denotes the contribution of each component. Tab. 4.2 lists the determined remagnetization times τ_1 and τ_2 .

Demagnetization [%]	τ_1 [fs]	τ_2 [ps]
12	140	-
45	240	-
55	250	5.1
75	300	7.7

Table 4.2: Analysis of the restoration of the M_x component from the micromagnetic model using two characteristic remagnetization timescales τ_1 and τ_2 .

There is very good agreement with the experimentally determined values shown in Tab. 4.1. Only τ_1 is underestimated by the micromagnetic model. This could be due to the reduced exchange interaction during the highly non-equilibrium magnetization state shortly after excitation, which is not incorporated into the simulation.

To evaluate the remagnetization process and the additional slow remagnetization time, the magnetic modes can also be extracted from the micromagnetic simulations. Fig. 4.6 presents the Fourier spectrum of the relative change of the M_x magnetization component at different time delays. High spatial frequencies dominate the magnetization relaxation at $\tau = 0$ ps. During the relaxation process, the center of the spectral weight moves towards lower spatial frequencies. At 6.7ps the center is around $k_z/2\pi = 0.1\text{nm}^{-1}$, which corresponds to the spatial spin-wave period of 10nm. This frequency spectrum shift to lower k -vectors for larger delay times describes the energy transfer from high-energy modes to low-energy modes within the spin-wave relaxation chain. In an ultrafast demagnetization experiment, the high-energy Stoner excitations are overpopulated by elementary relaxations of the hot electron system. These decay into short wave length spin excitations and gradually relax to lower spatial frequency excitations, towards the Kittel $k = 0$ precessional mode.

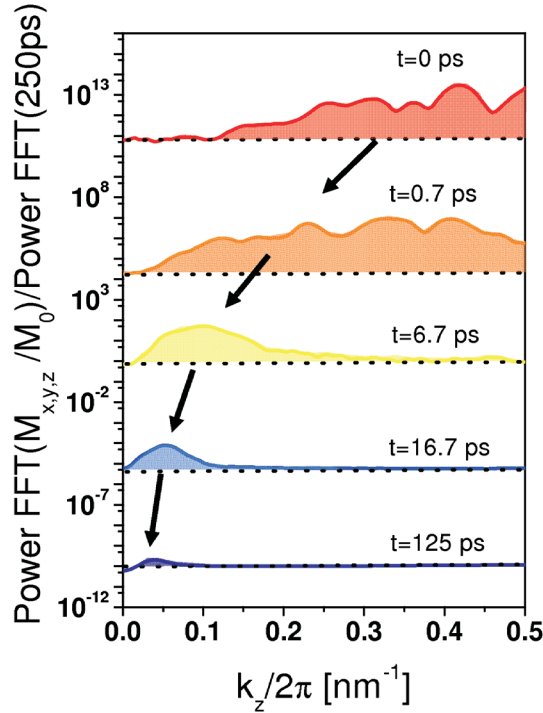


Figure 4.6: Cut through the micromagnetic simulation for a 50nm nickel film with a demagnetization of 55%. The corresponding Fourier transformation is presented as a function of the spatial frequency.

The slow recovery of magnetization for higher pump fluence is observed lately by Chantrell[50]. This approach is based on the Fokker-Plank equation which introduces a stochastic field term into the Landau-Lifshitz-Gilbert equation. The excitation mechanism is revealed by the increase in the electron temperature, which is directly related to the Gilbert damping parameter.

4.4 Conclusion

The time resolved experiments on the ps timescale reveal interesting features of the demagnetization processes upon laser excitation. The 50nm nickel sample was investigated by varying the external magnetic field and the pump fluence.

It is shown that the demagnetization peak height scales linearly with the external magnetic field larger than the saturation field. This implies that the Zeeman term cannot be neglected in the demagnetization process, even though it is much smaller than the thermal energy of hot electrons.

For higher pump fluencies applied, a slow recovery of the magnetization signal on the 10ps timescale is observed. Micromagnetic simulations are used to estimate the relaxation times of the magnetization upon the absorption of the

intensive laser pulse. So far, these simulations have appropriately reproduced experimental results on the sub ns range. The additional relaxation time on the scale of a few ps is attributed to energy transfer from the high energy spin-wave modes to modes with lower wave vectors and the Kittel $k = 0$ mode.

The observed ultraslow remagnetization connects the Stoner excitations, populated during the demagnetization process and attributed to high energy spin waves, with the coherent magnetization precessions on a longer timescale.

CHAPTER 5

Magnetization dynamics on a 100ps timescale

Magnetization relaxation after intensive pump-laser pulse excitation is followed by ultrafast demagnetization, which happens shortly after the pump laser reaches the sample, and by the coherent and incoherent collective relaxation modes, which happen on the ns time scale. The pump pulse energy enters the electron and phonon system and changes the anisotropy of the sample. This change shifts the orientation of the effective magnetic field and the magnetization aligns with the new easy axis. The thermally induced anisotropy field pulse lasts no longer than a couple of ps until electrons, phonons and spins achieve thermal equilibrium[51]. Once thermal equilibrium is established, the easy axis of the ferromagnet returns back to the position from before excitation and the magnetization starts to precess around a constant effective field. Parts of this chapter are published in [28, 52].

Fig. 5.1 shows a typical time resolved MOKE spectrum of the 50nm thin nickel film. The strong negative peak shortly after the pump pulse reaches the sample represents an ultrafast demagnetization. This is followed by a damped oscillation plus a background that decays on the nanosecond time scale, marked as the shaded region in Fig. 5.1. The former reflects coherence, while the later reflects incoherent relaxation processes, respectively. Lattice cooling through acoustic phonon emission is signatored in the reflectivity change, which also contributes to the magnetic signal as the phonon background. Nevertheless, this optical contribution to the TR MOKE spectrum is considerably smaller than the magnetic incoherent signal and can therefore be neglected, as shown later. The time resolved magnetic signal is thus the sum of the coherent and incoherent part:

$$\Delta\theta_K(t) = \Delta\theta_K^{co}(t) + \Delta\theta_K^{inco}(t) . \quad (5.1)$$

This thesis systematically investigates these two aspects of the magnetization

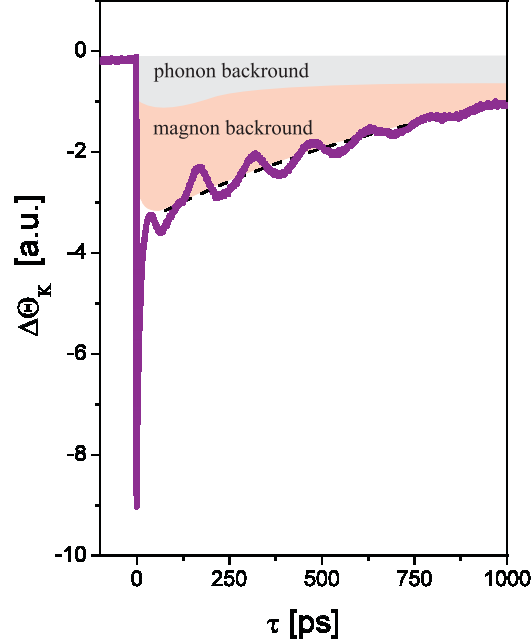


Figure 5.1: TR MOKE spectrum for a Si(100)/5nmCu/50nmNi/3nmCu sample at $\mu_0 H = -150\text{mT}$, $\varphi(\mathbf{H}) = 25^\circ$ out-of-plane and $F_{\text{pump}} = 50\text{mJ/cm}^2$

relaxation upon laser excitation. Controlled variation of the excitation mechanism and the effective magnetic field in the sample is achieved by varying the external magnetic field, in both amplitude and orientation relative to the sample surface, and by varying the intensity of the pump-laser pulse.

The main characteristics of both coherent and incoherent relaxation processes are first introduced on different samples by varying the external field amplitude. Different precession modes appear to depend on the thickness of the ferromagnetic sample. The basic Kittel mode is the dominant relaxation mode and is governed by the external magnetic field. The additional precession mode, attributed to the perpendicular standing spin wave, is observed for samples thicker than the optical penetration depth of the laser light. This mode is governed by the exchange interaction between spins, and shows weak dependence on the external magnetic field. Dipole dominated modes are observed for films considerably thicker than the optical penetration depth. These modes are present even without an external field.

Then the incoherent contribution to the time resolved MOKE spectra is analyzed. The magnetic nature of the background signal is implied by its dependence on the amplitude of the external field. It is attributed to the short wavelength magnons which do not contribute to the time resolved spectrum coherently. A phenomenological model is introduced to describe the magnon

background.

The time resolved measurements of the magnetization dynamic upon laser excitation give insight not only into the precession modes, which dominate the magnetization relaxation, but also the time scale of the energy dissipation processes. The energy of the magnetization torque dissipates throughout the lattice or distributes to the other magnetic modes. The Gilbert damping parameter is found to be dependent on the precession mode. A non-trivial frequency dependence on the damping parameter of the standing spin-wave mode is observed.

The thin ferromagnetic films investigated here have easy axes mainly in-plane. The out-of-plane component of the external field plays a significant role in triggering and controlling the magnetization precession. The angular dependence of the magnetization relaxation relative to the angle between the external field and the sample magnetization is then investigated by focusing on the following two aspects: First, the small angles between the magnetization and the external field, where the limit of triggering the magnetization precession are investigated. Second, the case in which the field is applied almost perpendicular to the sample, determining the explicit nature of different coherent modes.

The pump fluence determines the perturbation strength of the magnetization in the sample. Demagnetization, induced by the temperature increase from absorbed pump-laser pulse energy, governs the magnetization relaxation. Both coherent and incoherent magnetization relaxation channels are discussed within framework. This section is complementary to the discussion presented in the Chapter 4 concerning pump-fluence dependence on the short timescale.

5.1 Coherent precession modes

The coherent magnetization processes are characterized by the correlated behavior of the atomic magnetic moments. The neighbor spins do not relax independently in the local effective magnetic field. Rather the exchange correlation between them causes the coherent behavior observed in the time resolved magnetization relaxation spectrum. The precession modes are characterized by the precession frequency $\omega = 2\pi\nu$ and the Gilbert damping parameter α , which describes the timescale on which the magnetization aligns with the effective magnetic field.

In all-optical pump-probe experiments, the magnetization, disturbed from equilibrium by the intensive laser pulse, starts to precess in the effective magnetic field. Only the sample surface within the optical penetration depth λ_{opt} is directly excited by the pump-laser pulse. The various magnetic precession modes are triggered in samples with different ferromagnetic layer thicknesses. These modes can be classified by their origin into those led by the external magnetic field, by the exchange field and by the dipole field in the sample itself. This section investigates the dispersion relation of those three modes in external field amplitude dependence. For this purpose, ferromagnetic samples with thicknesses significantly smaller than λ_{opt} , larger than λ_{opt} and much larger

than λ_{opt} are considered separately. For nickel samples, the optical penetration depth at 800nm is $\lambda_{opt} \cong 25\text{nm}$.

The time resolved MOKE spectra can be directly analyzed in the time regime and also in the frequency regime using the Fourier transformations. Fitting the time resolved spectra to the damped sine function gives access to timescales of magnetization precession and magnetization torque energy dissipation. However, this fitting method is not effective for complicated time resolved spectra, which are composed from the different modes. On the other hand, using Fourier transforms yield the precession modes in the frequency regime. FWHM value of the Fourier peak in the frequency space gives the information on damping. The disadvantage of this method is our measurement range of 1ns, which gives relatively poor frequency resolution in the Fourier spectrum peaks. To solve this problem, the data can be interpolated with the zero value for delay times up to 10ns. Nevertheless, Fourier transforms are used only for the complicated TR MOKE spectra to determine the precession frequencies within this thesis. The damping parameter is only extracted from the fitting procedure in the time regime.

5.1.1 Kittel $k = 0$ mode

This section presents the magnetization dynamics of a 10nm thin nickel sample. The entire sample is excited directly by the pump-laser pulse. The probe pulse monitors the averaged magnetization of the entire sample because the thickness is significantly smaller than λ_{opt} . The strength of the excitation pulse is calculated from the demagnetization rate, which is extracted from the change of the hysteresis loops at the demagnetization peak maximum, measured with and without pump pulse. Fig. 5.2 shows these hysteresis measurements of the Si(100)/5nmPd/10nmNi/2nmCu sample, in which the external field \mathbf{H} is oriented 35° out-of-plane and a pump fluence of $F = 40\text{mJ}/\text{cm}^2$ is applied. Demagnetization induced by the pump-laser pulse is estimated from the relative

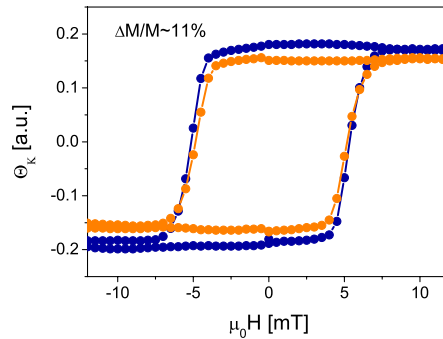


Figure 5.2: Hysteresis loops for the Si(100)/5nmPd/10nmNi/2nmCu sample with and without a pump-laser pulse at the maximum of the demagnetization peak. The external field is oriented 35° out-of-plane and the pump fluence is $40\text{mJ}/\text{cm}^2$.

change of the saturation magnetization of 11%. The rectangular shape of the hysteresis loops implies, that the easy axes of the magnetization lay in-plane.

Fig. 5.3 shows time resolved MOKE spectra of the Si(100)/5nmPd/10nmNi/2nmCu sample in which the external magnetic field \mathbf{H} is varied in amplitude from 0mT to 150mT. Only one precession mode contributes to the magnetization relaxation process. No precession is observed in absence of the external field. By increasing the external magnetic field amplitude, both amplitude and frequency of the magnetic precession increase. The external magnetic field shifts the direction of the effective field further out of plane, which is opposite to the tendencies of the demagnetization and anisotropy field to keep the magnetization in the plane. The frequency increase is expected due to the higher Zeeman term in the effective field (Eq. 2.36). The precession mode, which dominates the magnetization relaxation for this sample, is a volume homogenous coherent mode, which is often called the basic mode or Kittel mode. Here, the spins are aligned parallel to each other and there is no phase shift between the neighbor spins, which means that this mode can be characterized with the wavevector $k = 0$, due to the formalism of the spin waves.

The time resolved magnetic signal can be modeled with the oscillating function added to the linear background. The coherent term in Eq. 5.1 is represented

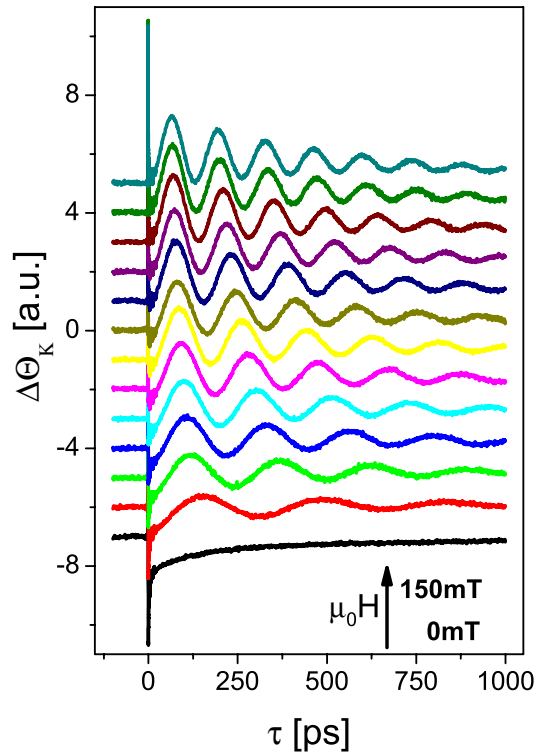


Figure 5.3: TR MOKE spectra for the Si(100)/5nmPd/10nmNi/2nmCu sample at $0\text{mT} < \mu_0 H < 150\text{mT}$, $\varphi(\mathbf{H}) = 35^\circ$ out-of-plane and $F_{pump} = 40\text{mJ}/\text{cm}^2$.

by the damped sine function:

$$\Delta\theta_K^{co} = \Delta\theta_0^{co} \sin(\omega t + \varphi_0) \exp(-t/\tau_\alpha), \quad (5.2)$$

where the precession at the frequency ω and the starting phase φ_0 is modulated by the precession amplitude $\Delta\theta_0^{co}$, which decays exponentially with the characteristic time τ_α .

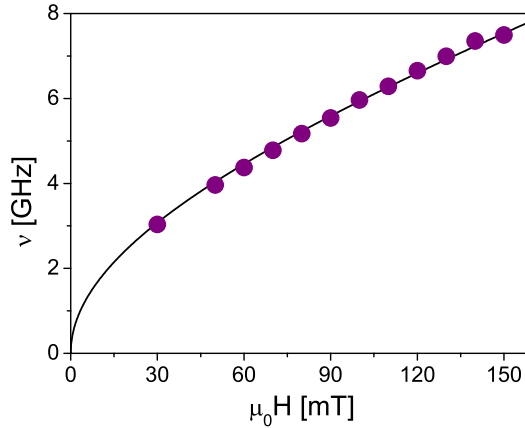


Figure 5.4: Frequency spectrum of the basic mode for the Si(100)/5nmPd/10nmNi/2nmCu sample at $0\text{mT} < \mu_0 H < 150\text{mT}$, $\varphi(\mathbf{H}) = 35^\circ$ out-of-plane and $F_{pump} = 40\text{mJ/cm}^2$.

Fig. 5.4 plots the precession frequency extracted from the TR MOKE spectra versus the amplitude of the external field. The applied magnetic field induces magnetization precession in the GHz regime, as already observed in the FMR experiments[53, 54]. By varying the external field from 30mT to 150mT, induced magnetization precession in the frequency range from 3GHz to 7.5GHz can be observed.

The frequency dispersion of the basic $k = 0$ mode is fitted to the Kittel formula, which, for the thin films with out-of-plane anisotropy K_z , is:

$$\nu_0 = \frac{\gamma}{2\pi} \sqrt{\mu_0 H \cos \phi \left(\mu_0 H \cos \phi + \mu_0 M_s - \frac{2K_z}{M_s} \right)} \quad (5.3)$$

where ϕ denotes the angle between the external magnetic field \mathbf{H} and the sample plane, and M_s represents saturation magnetization. The out-of-plane anisotropy constant $K_z = 5 \cdot 10^5 \text{J/m}^3$ is determined from the fit. The value is positive and considerably smaller than $1/2\mu_0 M_s^2$ as expected for the sample magnetized in-plane and therefore agrees with our experimental observation that the easy axis of the system is in-plane, as shown in the hysteresis loop in Fig. 5.2.

5.1.2 Standing spin-wave mode

This section presents the magnetization dynamics of a 50nm thin nickel sample. The time resolved spectra of the Si(100)/5nmCu/50nmNi/3nmCu sample, in which the external field is varied from 0mT to 100mT, are shown in Fig. 5.5. The field is oriented 25° out-of-plane and a pump fluence of 50mJ/cm² is applied. No

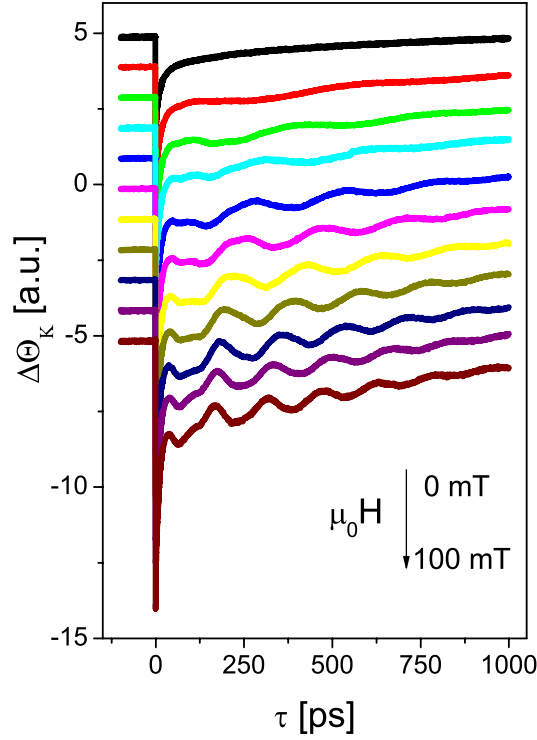


Figure 5.5: Time resolved spectra for the Si(100)/5nmCu/50nmNi/3nmCu sample at $0\text{mT} < \mu_0 H < 100\text{mT}$, $\varphi(\mathbf{H}) = 25^\circ$ out-of-plane and $F_{\text{pump}} = 50\text{mJ/cm}^2$.

precession is observed in absence of the external field. Increasing the amplitude of the external field enhances both the precession frequency and amplitude. The spectra contain the contribution of two oscillations. The lower frequency oscillation has a precession period of $T_1 \cong 100$ to 300ps for different values of the applied external magnetic field. The higher frequency oscillation, with a precession period of $T_2 \cong 40\text{ps}$, is clearly visible for larger \mathbf{H} .

The time resolved spectra in Fig. 5.5 are fitted with the function composed of the two damped sine functions and the linear expansion. Fig. 5.6 plots the fitting results for precession frequency of both modes versus the amplitude of the external field. The frequency ν_0 of the lower precession mode takes values from 2GHz up to 7GHz for the external fields $\mu_0 H \leq 100\text{mT}$. The second oscillation has frequencies ν_1 ranging from 11GHz up to 13GHz for the external fields $60\text{mT} \leq \mu_0 H \leq 100\text{mT}$.

The lower precession mode represents the volume homogeneous Kittel mode

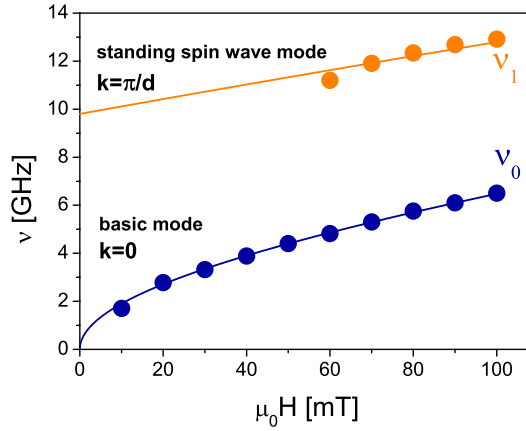


Figure 5.6: Frequency dispersion of the basic mode and standing spin wave for the Si(100)/5nmCu/50nmNi/3nmCu sample at $0\text{mT} < \mu_0 H < 100\text{mT}$, $\varphi(\mathbf{H}) = 25^\circ$ out-of-plane and $F_{\text{pump}} = 50\text{mJ/cm}^2$. The lines are appropriate fits given by Eq. 5.3 and Eq. 5.5.

introduced in the previous chapter. The precession amplitude of the basic $k = 0$ mode is significantly larger than that for higher oscillation, which implies that the Kittel mode is the dominant coherent channel for the magnetization relaxation. Kittel formula (Eq. 5.3) describes the frequency dependence of the main mode on the external field. The out-of-plane anisotropy constant $K_z = 4.2 \cdot 10^5 \text{J/m}^3$ is determined from the fit like before.

The higher precession mode can be attributed to the perpendicular standing spin wave (PSSW), shown in Fig. 5.7.

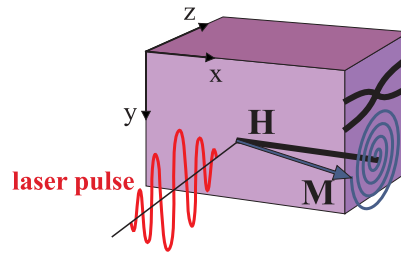


Figure 5.7: Standing spin-wave and $k = 0$ mode.

The spin waves excited on the sample surface by the pump-laser pulse propagate through the sample, until they reach the substrate and are then reflected back. The standing spin-wave mode forms if the film thickness is larger than the optical penetration depth λ_{opt} . The thickness of the ferromagnetic layer and the order of the standing wave then determine the wavevector \mathbf{k} of the spin wave as shown in Fig. 2.3. The standing first order spin-wave modes have been observed previously in time resolved pump-probe experiments by van Kampen et al.[32]. This study determined the dispersion relation of PSSW in regard

to the thickness of the ferromagnetic layer. Due to the exchange interaction between spins given by the constant D , the frequency of the standing spin-wave mode ν_1 is higher than the frequency of the basic mode ν_0 :

$$\nu_1 = \nu_0 + Dk^2, k = \pi/d. \quad (5.4)$$

For our experimental condition, where the external magnetic field \mathbf{H} is applied within an angle ϕ relative to the sample surface with the easy axis of the magnetization in-plane, the magnon dispersion relation is derived from the free magnetic energy, as described in one of Chapter 2. The frequency dispersion of the standing spin wave obeys the magnon dispersion relation determined by the exchange constant A :

$$\nu_1 = \frac{\gamma}{2\pi} \sqrt{\left(\mu_0 H \cos \phi + \mu_0 M_s - \frac{2K_z}{M_s} - \frac{2k^2 A}{M_s} \right) \left(\mu_0 H \cos \phi - \frac{2k^2 A}{M_s} \right)}. \quad (5.5)$$

The experimentally determined precession frequencies fit well with the previous equation, revealing that $2k^2 A/M_s = -180\text{mT}$.

The wave vector k of the PSSW can be determined by defining the boundary conditions at the sample surface and the interface with the substrate. Boundary conditions are defined by pinning the spins at the interfaces. For strong surface anisotropy fields, spins at the interface are fixed and the fixed boundary conditions are applied. In our case, however, it is reasonable to neglect pinning the spins and assume an open boundary condition at each interface. The first standing spin-wave mode is then characterized by the wavevector $k = \pi/d$. The fit results yield an exchange constant of $A = -1.2 \cdot 10^{-21} \text{J}\text{\AA}^{-1}$, slightly higher than the theoretical value $A^{th} = -7.8 \cdot 10^{-22} \text{J}\text{\AA}^{-1}$ for nickel.

Laterally confined standing spin waves are observed using Kerr microscopy in the time resolved pump-probe experiments with ultrashort magnetic pulses[20, 55–57]. Spin waves with small wave numbers are investigated in Brillouin light scattering experiments[27, 58, 59]. Neutron scattering is also a powerful method to investigate spin waves. Nevertheless, spin waves excited in all-optical pump-probe experiments have to be considered as one of several channels through which a highly excited ferromagnetic system tries to relax to the equilibrium upon laser excitation. Though this kind of experiment offers no new information about magnon scattering or complementary magnon dispersion relations, it defines standing spin waves as the process involved in magnetization relaxation upon laser excitation.

5.1.3 Dipole modes

Zeeman field and by exchange interaction dominate modes discussed in the previous sections. They are similar in that there is no excited mode in absence of an external field. Though magnon dispersion relation Eq. 5.5 allows the existence of the spin waves in absence of an external field, this mode has not been observed experimentally. Nevertheless, a new type of magnetization relaxation

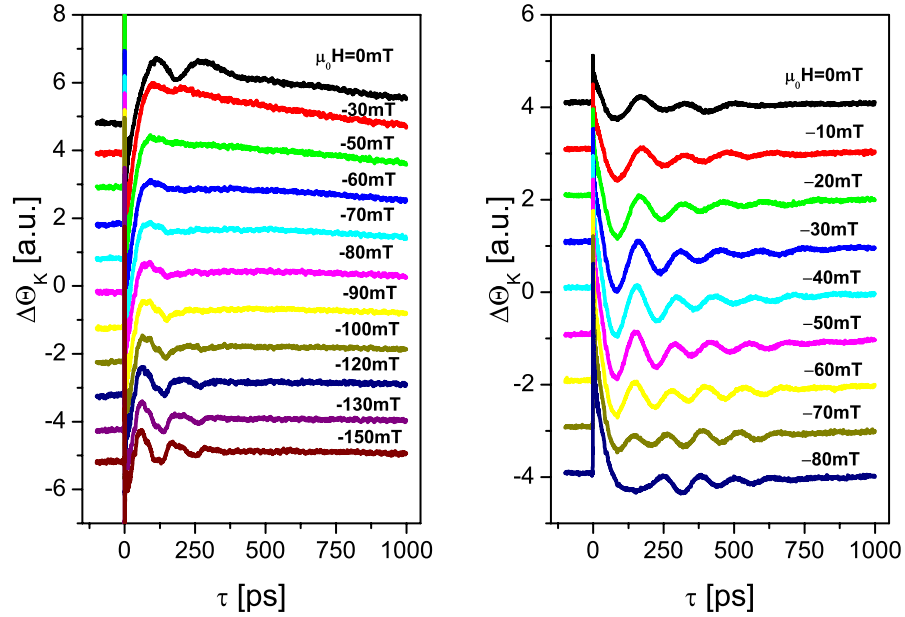


Figure 5.8: Time Resolved MOKE spectra for the a) Si(100)/5nmCr/100nmNi/2nmCu and b) Si(100)/5nmCu/150nmNi/3nmCu samples at a) $0\text{mT} < \mu_0 H < 150\text{mT}$, $\varphi(\mathbf{H}) = 35^\circ$ out-of-plane and $F_{\text{pump}} = 50\text{mJ/cm}^2$ and b) $0\text{mT} < \mu_0 H < 80\text{mT}$, $\varphi(\mathbf{H}) = 25^\circ$ out-of-plane and $F_{\text{pump}} = 40\text{mJ/cm}^2$.

in the absence of an external field is observed for ferromagnetic films with a thickness much higher than the λ_{opt} .

Fig. 5.8 shows the time resolved spectra of Si(100)/5nmCr/100nmNi/2nmCu and Si(100)/5nmCu/150nmNi/3nmCu samples with varied external field amplitude. Even in absence of an external field, clear precessional behavior of the magnetization is observed for both samples. When the external field increases, a new oscillation enters the time resolved spectra and the magnetic relaxation becomes quite complex. The unique property of the magnetization relaxation for those thick samples is ultraslow demagnetization, which is first achieved 100ps after the pump pulses reach the sample. This long demagnetization time is not reduced by increased external field amplitude.

To explain the existence of coherent precession modes without an external field, both the excitation mechanism and sample nature, have to be considered. The sample is a couple of times thicker than the optical penetration depth of the laser light. The magnetization precession is triggered by the anisotropy field pulse, which is caused by the temperature increase from pump pulse absorption on the sample surface. A strong depth profile of distributed thermal energy is present in the sample. Therefore the pump pulse affects mainly the magnetic moments at the sample surface leaving those deeper in the sample only slightly disturbed. Arranged like that, the magnetic moments at the surface lose their magnetic

order due to pump-laser pulse absorption, but still feel the magnetic field coming from the aligned magnetic moments buried deeper within the sample. The precession modes are then governed by the dipole interaction.

The magnetic relaxation of the 100nm nickel sample is characterized by the strong incoherent magnon background and by more than one magnetic oscillation in absence of the external magnetic field. When the external field increases, the magnetization relaxation spectrum changes in such a way that the external field suppresses both the incoherent magnon background and the magnetic precessions. By further increasing the external field to $\mu_0 H \geq 100\text{mT}$, two modes become clearly distinguishable in the spectrum. These can be attributed to the basic $k = 0$ mode and to the standing spin-wave mode.

Fig. 5.9 shows the Fourier transform of the time resolved spectra without incoherent magnon background is extracted, for a 100nm nickel film. The spectra are quite complicated with a number of modes owning similar frequencies. Nevertheless, the dominating relaxation modes can be recognized by comparing the spectra in the different external magnetic fields. Four frequencies are observed that systematically vary with the field. The main $k = 0$ mode dominates the magnetization precession for a higher external field. However, magnetization precession is given by a different mode in absence of the external field. This mode is suppressed by the Kittel mode, as observed for $\mu_0 H < 60\text{mT}$. Due to

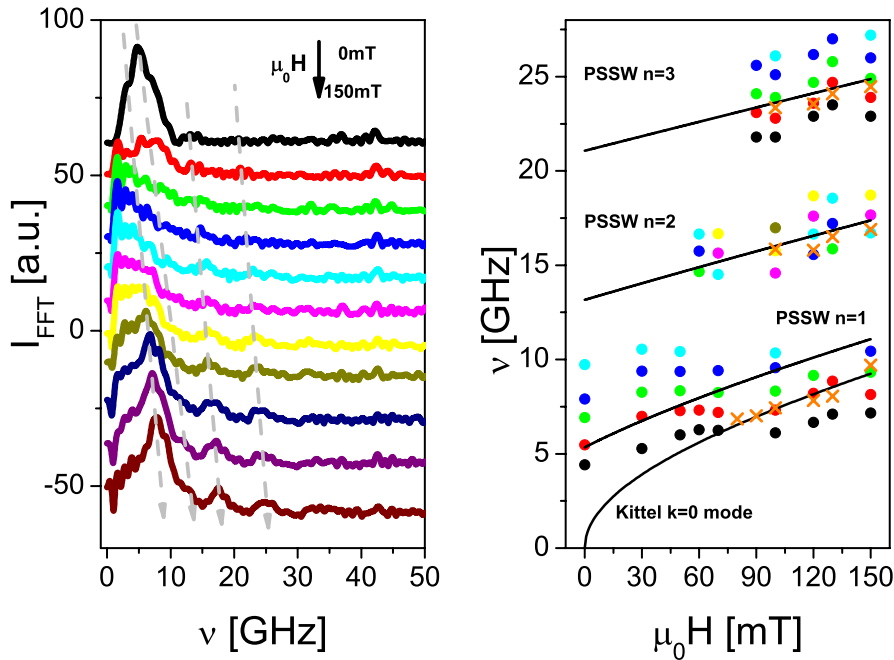


Figure 5.9: FFT spectra and main frequencies with attributed modes for a Si(100)/5nmCr/100nmNi/2nmCu sample.

their similar frequencies, these modes are almost indistinguishable for higher fields. Their nature is totally different. By increasing \mathbf{H} , two groups of higher frequencies can be recognized in the spectra. Their similar field dependence implies that they are governed by the same forces. The right side of Fig. 5.9 plots frequencies versus external field. The dominating precession mode is in good agreement with the Kittel formula (Eq. 5.3). The higher frequency modes are attributed to the perpendicular standing spin waves of the second and third order. The fitting function based on Eq. 5.5 perfectly describes the dispersion for higher frequencies. Although the main precession modes are identified, the rich frequency spectrum is not completely understood. The variety of modes probably originates from the complex magnetic structure of the chromium itself.

The magnetic relaxation of the 150nm nickel sample is less complicated than for the previous case, probably due to the lack of a Cr layer. It comprises a negligible magnon background and pronounced magnetic precession, which is again the sum of different oscillations in absence of \mathbf{H} . The increase in external field for this sample does not suppress the magnetization precession. In contrast, the amplitude of the dominating precession increases for fields of $\mu_0 H \leq 50\text{mT}$. Further increase of the external field leads to partially damped coherent magnetic relaxation.

The Fourier transformations are applied to the time resolved spectra in which

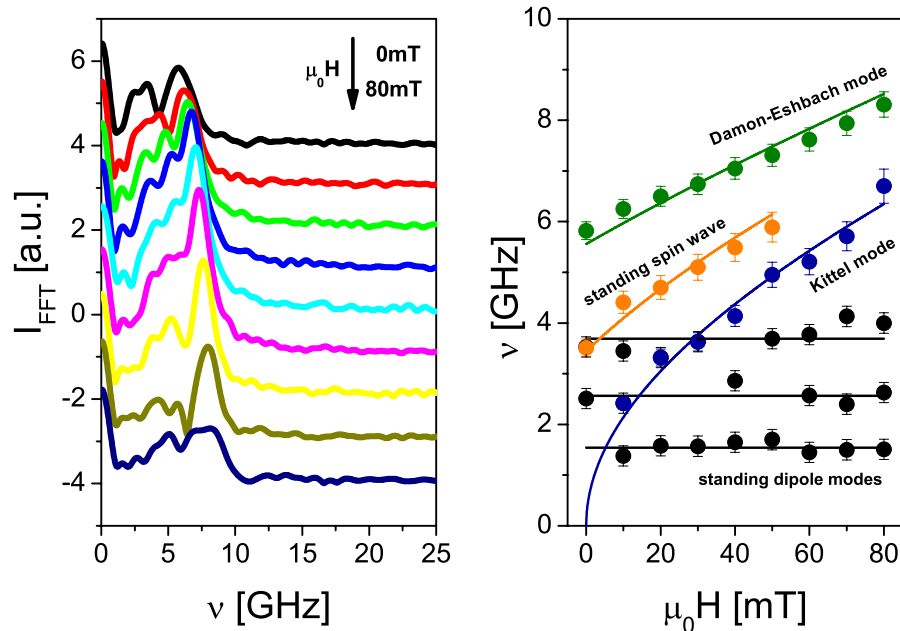


Figure 5.10: FFT spectra and main frequencies with attributed modes for the Si(100)/5nmCu/150nmNi/3nmCu sample.

the magnetic background, including the slow demagnetization peak, has been removed. Fig. 5.10 presents the resulting frequency spectrum as a function of external field. The left side shows the Fourier spectra and the right side shows the frequency spectrum. The observed modes can be classified by their intensity in the FFT spectrum. The precession mode with the highest intensity is the highest frequency mode, represented by olive circles, with values from 5.8GHz to 8.3GHz for the field $\mu_0 H \leq 80\text{mT}$ oriented 25° out-of-plane. The second highest intensity mode is mainly represented by blue points and for lower fields by the black and orange ones. The basic $k = 0$ mode has to be present within the spectrum. Due to good agreement with the Kittel formula, we attributed blue points to the Kittel mode. The frequencies take values up to 6.7GHz, and fitting estimates the out-of-plane anisotropy constant to $K_z \cong 0$. The small anisotropy constant implies that the easy axes of the system are not necessary in-plane, which agrees with the hysteresis measurements.

The frequencies attributed to the first order standing spin-wave mode are marked with orange circles. The exchange constant $A = -1.3 \cdot 10^{-21} \text{J}\text{\AA}^{-1}$, determined from the fit, agrees well with the exchange constant attributed to the standing spin wave of the 50nm thick nickel sample. This mode is present even in the absence of the external field, though with a significantly smaller intensity.

Since the Kittel and exchange modes are identified taking the values for the thinner films, the mode that dominates the time resolved relaxation spectra can only be attributed to dipolar modes. The excitation mechanism in all-optical pump-probe experiments assumes that energy of the pump-laser pulse is deposited to the sample surface within the penetration depth of the laser light. The non-uniformity of the energy profile within the sample thickness leads to the excitation of non-homogeneous dipole modes such as surface Damon-Eschbach mode[22]. The spin-wave vector is parallel to the sample surface and decays exponentially within the sample thickness. The spin waves belonging to this precession mode propagate perpendicular to the saturation magnetization on the sample surface. The dispersion relation of the Damon-Eschbach mode in external field \mathbf{H} is given by the following expression:

$$\nu^{DE} = \frac{\gamma\mu_0}{2\pi} \sqrt{H_x (H_x + M_s) + \frac{M_s^2}{4} (1 - \exp(-2qd))}, \quad (5.6)$$

where \mathbf{q} denotes the wave vector of the surface magnon mode, which is parallel to the sample surface. This equation can be used to fit the frequencies of the precession mode which dominates the spectrum. The agreement with the proposed frequency dispersion relation is good, as shown in Fig. 5.10. So it determines a spin-wave length of $\lambda = 2\pi/q = 4.2\mu\text{m}$. The resulting wave vector is much smaller than 10^8m^{-1} , which is the basic assumption of the dipole character of the observed mode.

In addition to these three modes (attributed to the Kittel mode, the standing spin-wave mode and the Damon-Eschbach mode), additional modes with significantly smaller intensity also contribute to the time resolved spectra. These modes are independent of external field and have constant frequencies of 1.5GHz,

2.5GHz and 3.7GHz. The small frequencies imply the dipole origin of those modes. However, the only standing dipole wave modes that can be formed within the demagnetization spot area are given by the beamwaist of the pump pulse. The ratio of the observed frequencies is $1.56 : 2.56 : 3.69 \cong 4^2 : 5^2 : 6^2$. The squared dependence of those modes implies that they are the volume modes. If we attribute those frequencies to the 4th, 5th and 6th order standing waves, the basic frequency is $\nu^0=0.065\text{GHz}$. Such a low frequency cannot be observed within our measurement range of 1ns. These modes can be attributed to volume backscattered dipole modes, as observed in the permalloy dots using Brillouin light scattering[59, 60]. The frequencies of the backscattered volume modes are smaller than the Kittel mode frequencies. The lateral confinement, in our case, is the beamwaist of the pump-laser spot, $\approx 60\mu\text{m}$.

5.2 Incoherent magnetic relaxation

The magnetization disturbed from equilibrium upon laser excitation, relaxes not only through the coherent precession, as described in the previous chapter, but also through incoherent processes. The shaded regions in Fig. 5.1 represent the incoherent magnon and phonon background. The magnetic contribution to the background signal has never been systematically investigated. Instead, the background signal is attributed mainly to thermal diffusion in the sample and creation of acoustic phonons which contribute to the signal both coherently, as stress waves, and incoherently, as a background. The phonon background enters the signal because of pure optical effects and is a signature of the lattice temperature change. It can be described by the thermal diffusion equation[28, 29]. Complementary time resolved reflectivity measurements on the same sample allow the phonon background to be approximated with the small linear contribution. To our knowledge, this is the first work observing the incoherent magnon background in time resolved magnetization dynamics experiments.

The incoherent magnetic relaxation is attributed to the short wavelength magnons with a short lifetime. The magnon distribution of the ferromagnet after excitation by a pump pulse can be found in [61]. Within this work, the magnon background is described by the following equation:

$$\Delta\theta_K^{inco} = \Delta\theta_0^{inco} \exp(-t/\tau_{mg}) , \quad (5.7)$$

where the amplitude $\Delta\theta_0^{inco}$ depends on the external field \mathbf{H} , the pump fluence and the adjustment of opening angle of the analyzer (shown in Fig. 3.10) similar to the precession amplitude $\Delta\theta_0^{co}$. The magnon decay time τ_{mg} is one phenomenological value that describes the characteristic decay time of the total magnon population number. The distribution of the frequency of the excited magnons is not directly observable in the background. Nevertheless, the micromagnetic simulations imply that spin waves with higher \mathbf{k} vectors are excited shortly after the pump-laser excitation. The scattering processes, involving phonons and multiple magnons, happen on a timescale of less than 10ps. Therefore, the magnon background, still significant for up to 1ns, is attributed

to spin waves with smaller \mathbf{k} and lower energy. τ_{mg} describes the time evolution of those magnons population numbers. The contributions from the magnons with higher wave vectors have to be considered for timescales smaller than 20ps. When the characteristic decay time τ_{mg} is large enough, which is half of the measurement range in the time resolved measurements, Eq. 5.7 is well approximated by the linear decay function:

$$\Delta\theta_K^{inco} = \Delta\theta_0^{inco} - \Delta\theta_{lin}^{inco}t, \quad (5.8)$$

where the coefficient $\Delta\theta_{lin}^{inco}$ is inversely proportional to the magnon decay time τ_{mg} . $\Delta\theta_0^{inco}$ will be considered a phenomenological constant at this point. The dependence on the sample nature and external field configuration will be additionally confirmed in the following experiments.

The magnon contribution to the time resolved MOKE spectrum in external magnetic field can be positive or negative with respect to the demagnetization curve in absence of \mathbf{H} . For a 50nm thin nickel sample, it contributes positively. The magnon background contributes negatively for thinner films such as 10nm nickel film. Last chapter presents also the systematic change of the magnon background dependence on the thickness of the ferromagnetic layer together with investigation of the non-local damping by spin currents on wedge samples.

The incoherent background in the time resolved spectra of the Si(100)/5nmCu/50nmNi/3nmCu and Si(100)/5nmPd/10nmNi/2nmCu samples, shown in Fig. 5.5 and Fig. 5.3, is well approximated by the linear function. The dependence on external magnetic field implies a magnetic origin of the incoherent background. Fig. 5.11 plots the offset and linear coefficient of the incoherent magnon background versus the amplitude of the external field for both samples.

The linear increase of the $|\Delta\theta_0^{inco}|$ with the external field originates from the excitation of additional spin-wave modes, which are available for that specific

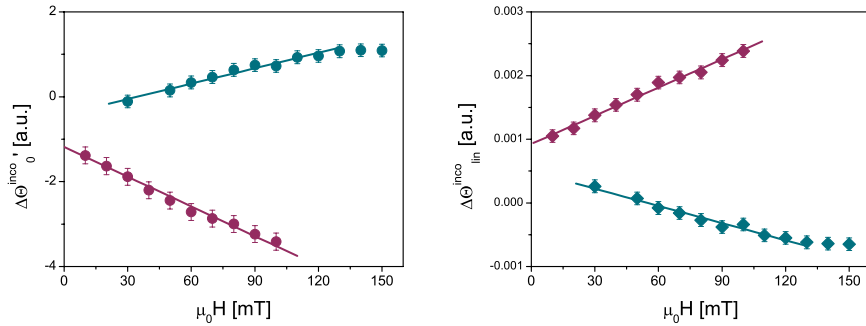


Figure 5.11: Incoherent magnon background for Si(100)/5nmCu/50nmNi/3nmCu (violet points) and Si(100)/5nmPd/10nmNi/2nmCu (turquoise points) samples. Both the amplitude and the linear coefficient of the magnon background scales linearly with the amplitude of \mathbf{H} . Opposite signs of the magnon contribution can be attributed to the thickness of the ferromagnetic layer.

H. By increasing the amplitude of the external field, the excitation spectrum of spin waves becomes broader, which contributes to the increased number of excited magnons. At the same time, the linear coefficient $|\Delta\theta_{lin}^{inco}|$ also increases by increasing the external field. This increase is attributed to the short lifetime of the excited high energy magnons. A further incensement of the external field leads to saturation of both the offset and the linear background. In that case, all available spin waves are excited and magnons cannot absorb the additional Zeeman energy.

The applied external field **H** cannot change the linear character of the magnon background. The exponential character of the magnon background is observed only for highly excited samples. This is only possible by increasing the excitation rate: either by increasing the pump fluence or reducing the thickness of the ferromagnetic layer. Deeper analysis is shown later on.

5.3 Mode dependent damping

Previous sections present magnetization relaxation upon laser excitation by means of magnetization precession modes and emission of short wavelength incoherent magnons. Nevertheless, the time resolved spectra contain timescales of the magnetic energy dissipation processes as well. Direct observable magnetic damping in the time domain is the main advantage of pump-probe experiments over other standard techniques used to investigate the magnetization dynamics, such as FMR[62]. This section presents the damping parameter of the main $k = 0$ mode and the standing spin-wave mode for the Si(100)/5nmCu/50nmNi/3nmCu sample.

The Landau-Lifshitz-Gilbert equation describes the magnetization vector, which follows the precession torque in \mathbf{H}_{eff} and continuously loses energy due to the damping term, characterized by the dimensionless damping constant α . The exponential decay time τ_α of the precession amplitude can be determined from the time resolved measurements. The relation between the characteristic exponential decay time τ_α and the Gilbert damping constant α depends on the sample properties and the applied external magnetic field **H**. The effective magnetic field, which governs the precession mode, explicitly determines the relation $\alpha(\tau_\alpha)$, as presented in the theory chapter. Therefore, the damping parameter α can be determined separately for each precession mode.

For the basic $k = 0$ mode, the effective magnetic field is composed of the Zeeman, demagnetization and crystalline-anisotropy term. For samples with out-of-plane anisotropy given by K_z , the damping parameter α_0 obeys the following relation:

$$\alpha_0 = \left(\tau_\alpha \gamma \mu_0 \left(H \cos \phi - \frac{K_z}{\mu_0 M_s} + \frac{M_s}{2} \right) \right)^{-1}, \quad (5.9)$$

where ϕ denotes the angle of the external magnetic field **H** relative to the sample plane. The anisotropy constant K_z can be determined by fitting the frequency spectrum of the basic mode with the Kittel formula.

For the standing spin-wave mode, the additional exchange interaction term contributes to the effective magnetic field Eq. 2.37. It can be derived from the magnetization vector of the perpendicular standing spin wave, as shown in Chapter 2. From the time resolved spectra in Fig. 5.5 the damping parameter of the standing spin-wave mode α_1 is expected to be significantly larger than α_0 . The relation between the characteristic exponential decay time τ_α of the standing spin-wave mode and the damping parameter α_1 is determined by:

$$\alpha_1 = \left(\tau_\alpha \gamma \mu_0 \left(H \cos \phi - \frac{K_z}{\mu_0 M_s} - \frac{2k^2 A}{M_s} + \frac{M_s}{2} \right) \right)^{-1}. \quad (5.10)$$

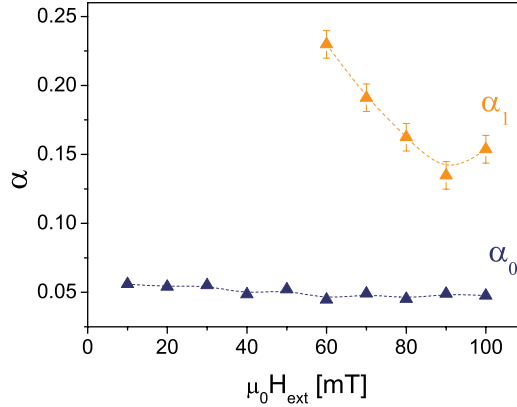


Figure 5.12: Damping parameter of the basic mode and standing spin wave for the Si(100)/5nmCu/50nmNi/3nmCu sample at $0\text{mT} < \mu_0 H < 100\text{mT}$, $\varphi(\mathbf{H}) = 25^\circ$ out-of-plane and $F_{\text{pump}} = 50\text{mJ/cm}^2$. The lines are guides for the eyes.

As with the case of the basic mode, the frequency spectrum of both basic $k = 0$ and the standing spin-wave mode have to be known to determine α_1 . The value of the anisotropy constant K_z and the exchange constant A can be determined by fitting those frequency spectra with Eq. 5.3 and Eq. 5.5.

Fig. 5.12 presents the damping parameters for the basic mode and for the standing spin-wave mode of the Si(100)/5nmCu/50nmNi/3nmCu sample versus the amplitude of the external magnetic field. The damping parameter of the basic mode $\alpha_0 = 0.050(5)$ is constant for applied magnetic fields $\mu_0 H \leq 100\text{mT}$. The standing spin-wave mode is more heavily damped. The damping parameter α_1 takes values from $0.135(2)$ in higher fields, up to $0.230(2)$ in lower fields. The pronounced frequency dependence of α_1 is a result of the two-magnon and related three-magnon scattering processes, in which the coherent precession mode scatters with frequency-dependent efficiency at the short wavelength magnons. The strong incoherent magnon background in the TR MOKE spectra implies a number of scattering channels, which leads to strong frequency dependence of α_1 . Those scattering processes can be excluded by orienting the external field further out-of-plane, as shown in the following section. The mode dependent

damping has been observed in time-resolved experiments with short magnetic pulses[20].

5.4 Dependence on external field orientation

To further explore the properties of the magnetization relaxation, both the amplitude of the external field and the orientation relative to the magnetization of the sample surface are varied. The maximum external field available in our experimental setup is insufficient to tilt the magnetization significantly towards the sample normal. Two configurations are considered. First the importance of the orientation of the external field in the excitation mechanism, in which H is mainly in-plane and tilted for the small angle towards the sample normal, is considered. Second, the other limit, where the field is oriented almost perpendicular to the sample surface, introducing new aspects of the magnetization relaxation with respect to both coherent and incoherent processes. The measurements presented in this chapter are on the Si(100)/5nmCu/50nmNi/3nmCu sample discussed in Section 5.1.2.

5.4.1 Small angles between magnetization and applied field

The demagnetization caused by the intensive pump-laser pulse is followed by both the coherent and incoherent magnetic relaxation processes, as seen in the previous chapters. The external field plays an important role in triggering the magnetization precession of the in-plane magnetized thin ferromagnetic sample. The out-of-plane component of the external field tries to cant the magnetization. Without a small out-of-plane magnetization component, there would be no observable precession in H_{eff} , because H_{eff} is directed dominantly in-plane due to the demagnetization field.

Fig. 5.13 shows the TR MOKE spectra of the Si(100)/5nmCu/50nmNi/3nmCu film in an external field of $\mu_0 H = -60\text{mT}$. The angle of the applied magnetic field varies from -25° up to 25° with respect to the sample plane. When H is completely in-plane, represented by the black curve in Fig. 5.13, the oscillations are almost negligible with a small precession amplitude. A field oriented only 5° out-of-plane already causes a considerably larger precession amplitude. By orienting the field further out-of-plane, a increase of the precession amplitude is observed. The increase of the precession amplitude comes from the larger opening angle of the magnetization torque induced by the higher out-of-plane field component. At the same time, the precession frequency $\nu_0=4.7\text{GHz}$ and the damping parameter $\alpha=0.048(2)$ of the magnetization precession stay constant for all angles of the applied field. The effective contribution of the Zeeman term does not significantly change for the different applied field orientations. Therefore, the optimal configuration to investigate the characteristic timescales of the magnetization relaxation processes from the in-plane magnetized samples occurs when H is oriented $\approx 30^\circ$ out-of-plane.

By rotating the external field from ϕ to $-\phi$ with respect to the sample plane,

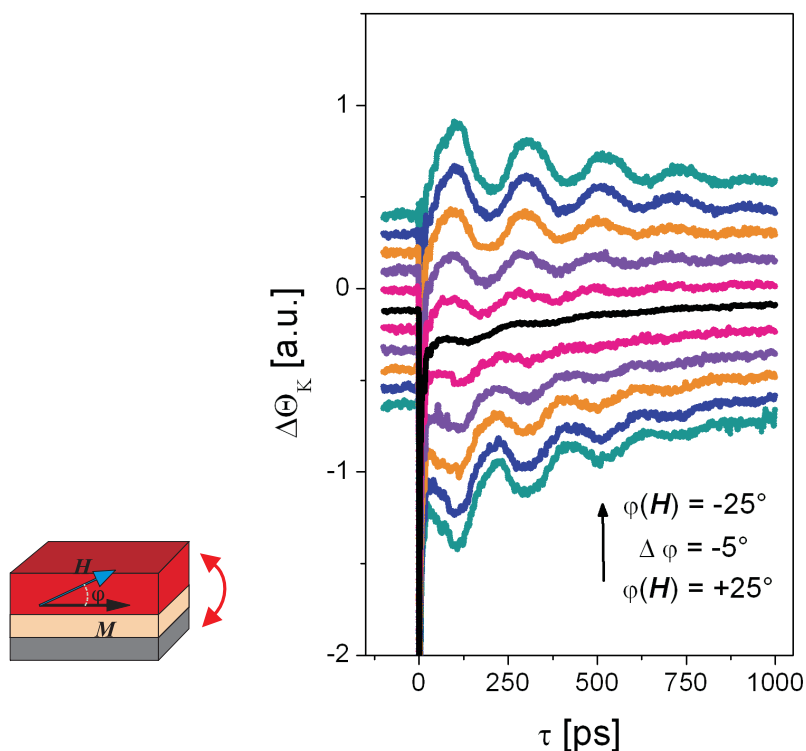


Figure 5.13: Time Resolved MOKE spectra for the Si(100)/5nmCu/50nmNi/3nmCu sample at $\mu_0 H = -60\text{mT}$, $-25^\circ < \varphi(H) \leq 25^\circ$ and $F_{\text{pump}} = 50\text{mJ/cm}^2$.

the phase of the magnetic precession is changed by π . Interestingly, the phase shift remains π even for the smallest tilting angle of only 5° . The time resolved spectra in Fig. 5.13 are fitted with the damped sine function plus linear expansion. Fig. 5.15 a) plots the beginning phase versus the tilting angle of the external field.

The change in magnetization precession starting phase results from the different

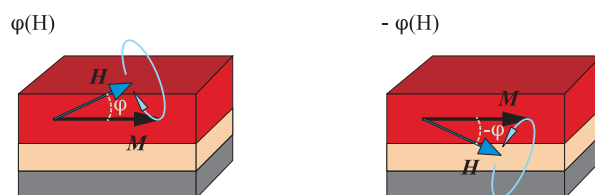


Figure 5.14: Schematic view of the magnetization precession when the external field is oriented φ or $-\varphi$ relative to the sample plane.

magnetization orientation relative to \mathbf{H}_{eff} , as shown in Fig. 5.14. The magnetization precesses clockwise or counterclockwise depending on the external field, directed at an angle ϕ or $-\phi$ relative to the sample surface. Also the incoherent

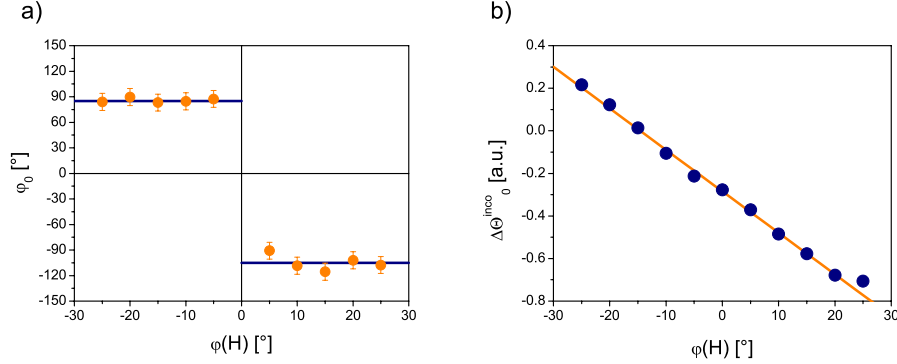


Figure 5.15: a) The starting phase of the precessing magnetization and b) the amplitude of the magnon background versus orientation of the external field $\phi(\mathbf{H})$

magnetic relaxation depends strongly on the orientation of the external field relative to the sample. It increases linearly with increasing the magnetization torque opening angle and even changes its sign for larger out-of-plane angles of H , as shown in Fig. 5.15 b). The absolute values of the incoherent magnon background depend on the orientation of the analyzer.

5.4.2 Large angles between magnetization and applied field

Fig. 5.16 gives a brief overview of the processes presented in this chapter. The time resolved spectra of the Si(100)/5nmCu/50nmNi/3nmCu sample are presented as a matrix, with the Kerr signal plotted versus the external field amplitude at a given time delay between pump and probe pulse. The intensity of the Kerr signal is indicated by the color.

The orientation of the external field varies from in-plane towards out-of-plane. Both the basic mode with $k = 0$ and the first standing spin-wave mode with $k = \pi/d$ are recognized in the matrix spectra. The basic mode is characterized with a higher oscillations intensity and a larger precession period. The standing spin-wave mode has a smaller precession period and smaller variations in intensity. For a field oriented 25° out-of-plane, the basic mode dominates the relaxation process and the standing spin-wave mode is hard to observe. By orienting the external field further out-of-plane, the frequency of the main mode lowers and the standing spin-wave mode dominates the relaxation spectrum. For the field oriented completely out-of-plane only the standing spin-wave mode is observed. The significant change in magnetization dynamics as a function of external field orientation relative to the sample plane of the main mode results from reduction of the in-plane component of the effective field. On the other hand, the standing

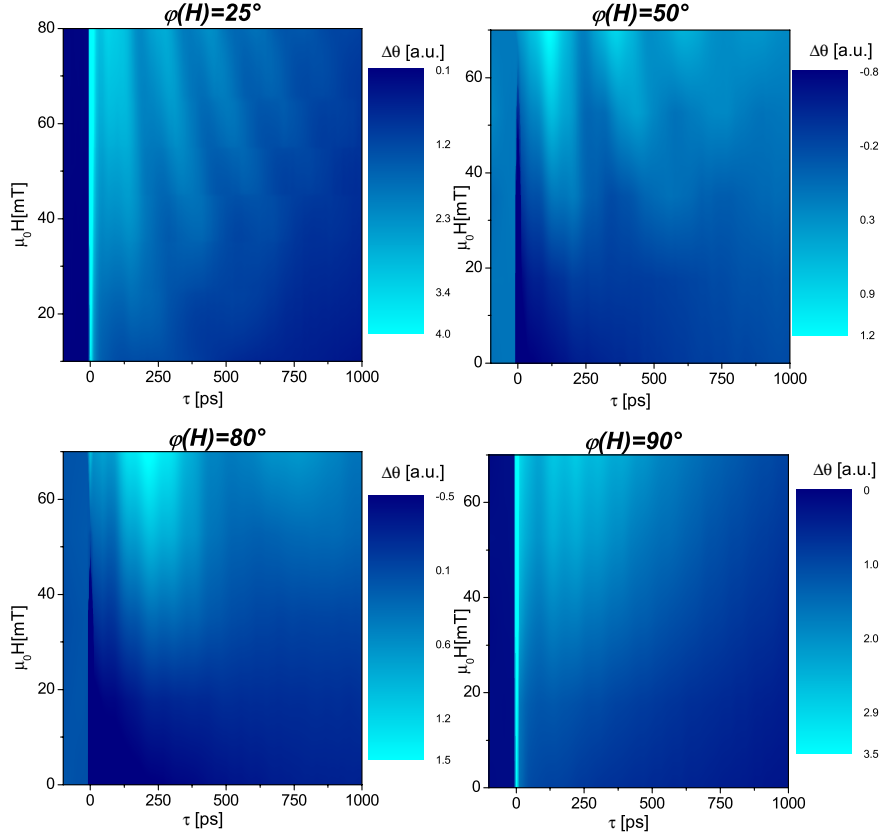


Figure 5.16: Matrix representation of the TR MOKE spectra for the Si(100)/5nmCu/50nmNi/3nmCu sample at $0\text{mT} < \mu_0 H < 80\text{mT}$ and $\varphi(\mathbf{H})=25^\circ, 50^\circ, 80^\circ$ and 90° and $F_{\text{pump}} = 50\text{mJ}/\text{cm}^2$.

spin-wave mode is almost independent of the external field orientation.

Fig. 5.17 shows the TR MOKE spectra of the Si(100)/5nmCu/50nmNi/3nmCu film in $\mu_0 H = -70\text{mT}$, where the angle of the applied magnetic field varies from in-plane to out-of-plane. The curves are normalized by their demagnetization peak amplitudes for better comparison. Again, both the short and the longer period oscillations can be recognized within the spectrum. When the external field is oriented with an angle of $\varphi(\mathbf{H}) \geq 50^\circ$, the period of the main precession mode changes significantly. It strongly increases by increasing the angle between the sample and \mathbf{H} up to a value comparable with our measurement range for $\varphi(\mathbf{H}) = 90^\circ$. On the other hand, the higher oscillations, attributed to the standing spin waves have a constant frequency for different external field orientations relative to the sample plane. Nevertheless, this mode, hardly observable when $\varphi(\mathbf{H}) \leq 25^\circ$, has a clear precession pattern. A number of periods are identified when the field is oriented more out-of-plane.

The maximum applied external field of $\mu_0 H = -70\text{mT}$ is not large enough for

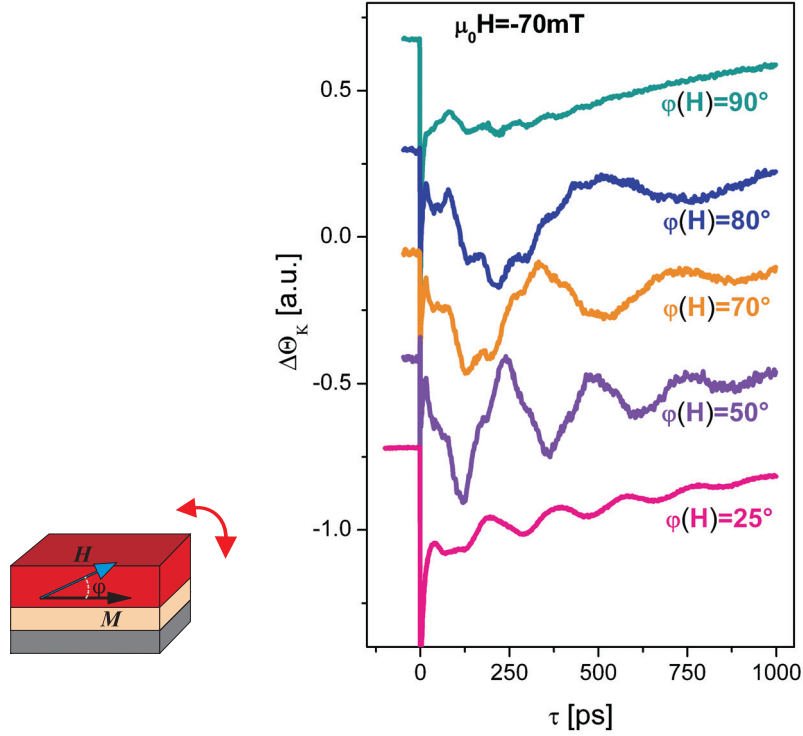


Figure 5.17: TR MOKE spectra for the Si(100)/5nmCu/50nmNi/3nmCu sample at $|\mu_0 H| = 70 \text{ mT}$, $\varphi(\mathbf{H}) = 25^\circ, 50^\circ, 80^\circ$ and 90° and $F_{pump} = 50 \text{ mJ/cm}^2$. The curves are normalized by the demagnetization peak amplitude for comparison.

the Zeeman term to overcome the demagnetization field, so the magnetization aligns with \mathbf{H} . The magnetization stays mainly in the sample plane with a maximum canting angle of 8° for a perpendicular external field. Complementary hysteresis measurements reveal an increase in saturation field from rotating the external field out-of-plane. Fig. 5.18 shows the hysteresis measurements of the Si(100)/5nmCu/50nmNi/3nmCu sample for different orientations of \mathbf{H} . The changes in the hysteresis loops are negligible for the external field oriented at $\phi(\mathbf{H}) \leq 35$. When the external field is oriented 25° out-of-plane, the coercive field is $\mu_0 H_c = 5 \text{ mT}$. By rotating the field further out-of-plane, the coercive field increases up to a value of $\mu_0 H_c = 50 \text{ mT}$ for almost perpendicular \mathbf{H} . In this case the finite value of H_c originates from the small experimental disalignment of the relevant field orientation. The coercive field H_c is plotted versus $\phi(\mathbf{H})$ in the inset in Fig. 5.18. The observed increase of the saturation field results from the demagnetization field, which works against the Zeeman term for systems with in-plane easy axes and demands more energy to align magnetic moments. Fig. 5.19 plots the frequency and the damping parameter of both precessing

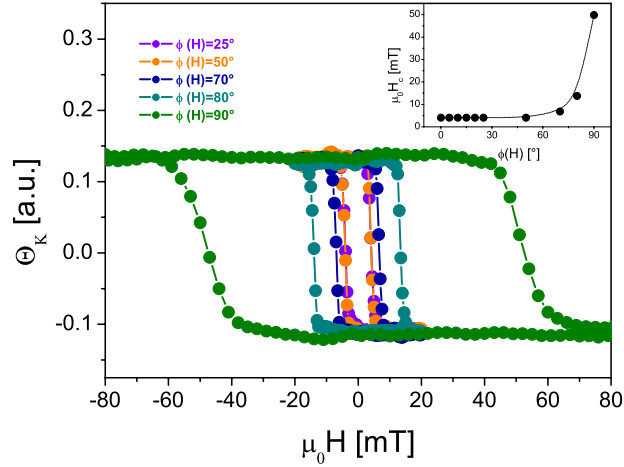


Figure 5.18: Hysteresis loops for the Si(100)/5nmCu/50nmNi/3nmCu sample versus the external field orientation. Inset: the saturation field versus the angle between sample and external field. The line is guide for the eyes.

modes extracted from the time resolved MOKE spectra versus the external field direction. The frequency of the main mode varies from $\nu_0 = 1.8\text{GHz}$ for $\phi(\mathbf{H}) = 80^\circ$ to 5.3GHz for $\phi(\mathbf{H}) = 25^\circ$ out-of-plane. On the contrary, the frequency of the higher precession mode $\nu_1 \approx 12\text{GHz}$ is almost independent of the field direction. Angular dependence of the basic $k = 0$ mode agrees well with the Kittel formula in Eq. 5.3 and the determined anisotropy constant, $K_z = 4.2 \cdot 10^5 \text{J/m}^3$. Fig. 5.19 shows a fit as a continuous line. This mainly mirrors the reduction of the in-plane component of the external field \mathbf{H} . The higher frequency mode can be considered almost constant at $\nu_1 = 11.8\text{GHz}$ due to its origin in exchange interaction. This makes the contribution of the Zeeman term negligible in this case.

The damping parameter of the basic mode α_0 is almost constant for all orientations of \mathbf{H} . The observed small increase of α_0 for the perpendicularly directed external field is unreliable because of the large precession period and the resulting uncertainty in determining the exponential decay time. On the contrary, the damping parameter of the standing spin-wave mode is strongly dependent on the direction of \mathbf{H} . This mode is less damped when the field is oriented further out-of-plane. There is a huge change in the damping parameter from $\alpha_1 = 0.190(5)$ with the field oriented 25° out-of-plane, down to $\alpha_1 = 0.050(5)$ for the field oriented at $\phi(\mathbf{H}) \geq 50^\circ$. In this case, the damping parameter of the standing spin-wave mode is the same as that for the basic mode, $\alpha_1 \approx \alpha_0$.

The strong reduction in damping parameter for α_1 is explained by the two-magnon scattering contribution to the damping parameter. Woltersdorf in [63] attributes the extrinsic damping to the mode conversion mechanism in which the coherent mode scatters into incoherent modes. The number of the available incoherent modes is strongly dependent on field orientation in respect to satura-

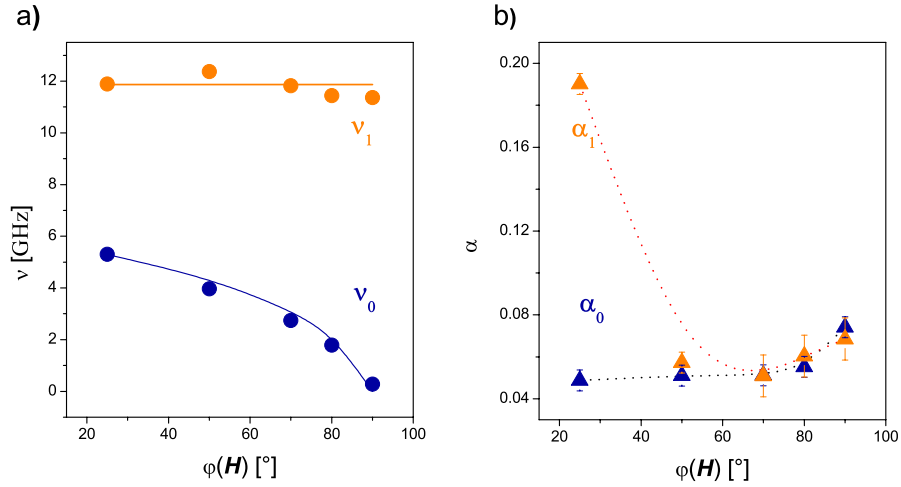


Figure 5.19: a) Precession frequency and b) damping parameter for the Si(100)/5nmCu/50nmNi/3nmCu sample at different orientations of the external field. The fit according to Eq. 5.3 is shown for ν_0 . Frequency ν_1 is fitted with a constant function. The lines in b) are guides for the eyes.

tion magnetization. When the angle between \mathbf{H} and the magnetization is more than $\pi/4$, there are almost no available modes to scatter[64]. Our experimental results confirm this exactly. The reduced number of the available scattering channels leads to the reduction of α_1 when the field is rotated out-of-plane.

A significant change in the ratio of the precession amplitude and the incoherent magnon background amplitude also occurs with changing orientation of the external field relative to the sample. It is much less than 1, if \mathbf{H} is oriented 25° out-of-plane, and grows to almost 3 for fields oriented out-of-plane. This ratio implies that the dominant relaxation processes are incoherent for in-plane applied fields, and coherent for out-of-plane applied fields. This also results from the absence of available incoherent magnon modes into which the coherent mode can scatter when the applied field is oriented towards larger angles relative to the magnetization of the sample. In that case, the incoherent magnon background contribution to the magnetization relaxation is much smaller than the contribution from coherent precession. This is exactly what our experimental results imply.

5.5 Dependence on the pump fluence

The previous sections discussed magnetization dynamics upon laser excitation as a function of external field, which determines together with the anisotropy and the demagnetization field, the constant effective field, which then governs the magnetization precession. However, it does not explicitly consider the

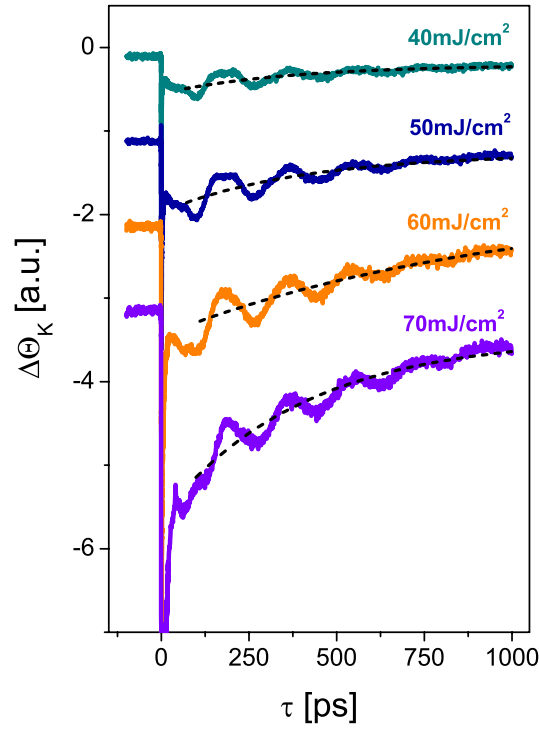


Figure 5.20: TR MOKE spectra for the Si/5nmCu/50nmNi/3nmCu sample at $\mu_0 H = 80\text{mT}$, $\varphi(\mathbf{H}) = 25^\circ$ and $40\text{mJ/cm}^2 < F_{\text{pump}} < 70\text{mJ/cm}^2$. The lines are exponential fits of the incoherent magnon background.

strength of the anisotropy field pulse, which triggers the magnetization precession. This section investigates the strength of the anisotropy field pulse and the related magnetization dynamics of the Si/5nmCu/50nmNi/3nmCu sample, by varying the pump fluence. For a higher pump-beam intensity, the temperature induced change in the anisotropy is larger, which leads to the enhanced magnetization disorder. The highly non-equilibrium ferromagnetic system then relaxes through a number of both coherent and incoherent relaxation processes. Fig. 5.20 shows the time resolved MOKE spectra of Si(100)/5nmCu/50nmNi/3nmCu sample in which the laser pump fluence is varied from 40mJ/cm^2 up to 70mJ/cm^2 .

Extra precaution is taken to prevent sample damage from the pump fluence. The sample surface, after hours of constant exposure to the pump laser, is controlled optically and no indication of damage is noticed. The magnetic signal is also strongly dependent on excitation. The increase of the sample temperature beyond the melting point would cause the disappearance of the magnetic contrast. Excitation by the pump-laser pulse is a cumulative effect which would lead to a noticeable difference between repeated time-resolved spectra of the overheated sample. None of these indications are present in our measurements. In identical repeated time-resolved spectra after hours of

exposure to the pump pulse, thermal damage of the sample can be excluded. One has to keep in mind that the energy of the laser pulse is given to the lattice within a few 100fs to ps and very high temperatures up to 1000K maximum on the sample surface are reached. Thereafter, the energy is distributed from the sample surface within 50ps, due to the high thermal conductivity of the substrate, which is needed for this kind of experiments. The rise of the sample temperature is not higher than a few 10K.

Both coherent and incoherent magnetization relaxation processes are dependent on the pump fluence. Fig. 5.21 plots the demagnetization peak amplitude and the basic mode amplitude versus the pump fluence. An increase in incoherent magnon background and precession amplitude of both the basic and standing spin-wave modes follow the increase of the pump fluence. The linear increase of those amplitudes again confirms that the high pump fluencies do not damage the sample.

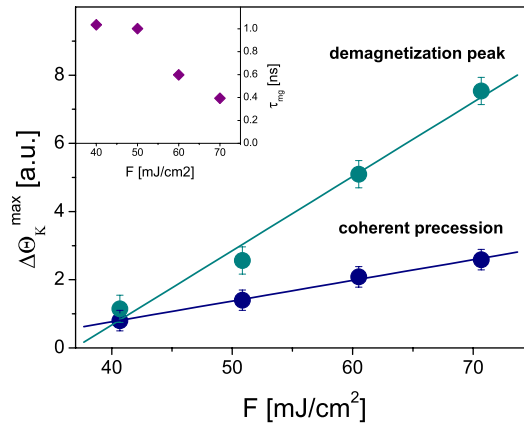


Figure 5.21: Amplitude of incoherent and coherent relaxation processes for the Si(100)/5nmCu/50nmNi/3nmCu sample at $\mu_0 H = 80\text{mT}$, $\varphi(\mathbf{H}) = 25^\circ$ and $40\text{mJ/cm}^2 < F_{\text{pump}} < 70\text{mJ/cm}^2$. Inset: The magnon exponential time τ_{mg} is plotted versus pump fluence.

The pronounced exponential character of the magnon background for higher pump fluencies indicates the high non-equilibrium state in which the main relaxation processes are the emission of incoherent magnons. The exponential decay time τ_{mg} can be used to quantify the time dependent magnon population. For a highly excited sample, $\tau_{mg} \approx 400\text{ps}$ is observed. By reducing the pump fluence, τ_{mg} increases and the exponential character of the magnon background disappears. Inset in Fig. 5.21 plots the magnon exponential decay time versus the pump fluence.

The magnetization relaxation through coherent precession modes does not significantly change for different pump fluencies. The Fourier transforms are applied to the TR MOKE spectra, for which the incoherent magnon background is removed. Fig. 5.22 shows the results. The Fourier spectrum is presented for

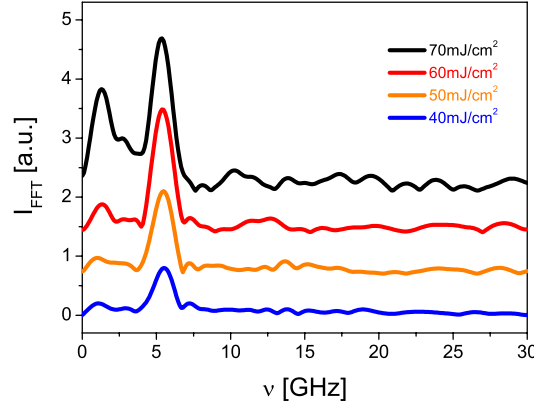


Figure 5.22: Frequency spectrum of the coherent precession for the Si(100)/5nmCu/50nmNi/3nmCu sample at $\mu_0 H = 80\text{T}$, $\varphi(\mathbf{H}) = 25^\circ$ and $40\text{mJ/cm}^2 < F_{\text{pump}} < 70\text{mJ/cm}^2$. The FFT spectra are vertically shifted for clarity.

the laser pump fluence from 40mJ/cm^2 up to 70mJ/cm^2 . First, one there is a systematic increase in the intensity of the Fourier peaks with increasing the pump fluence. Second, the positions of the Fourier peaks do not change for the applied pump fluencies. The observed modes can be grouped as follows: the main $k = 0$ mode with $\nu_0 = 5.4\text{GHz}$ dominating the precession spectrum. The two lower modes at 1.1GHz and 2.9GHz , which strongly vary in intensity, and can be attributed to the standing dipole modes. They are excited within the demagnetization spot area, which stays constant for all pump fluencies, hence the change in pump fluence originates only from the varied intensity of the pump pulse. As an approximation, the damping parameter can be estimated from the FWHM of the Fourier peak, which shows that the damping parameter of the main mode α_0 does not change with varying pump fluence.

5.6 Conclusion

All-optical pump-probe experiments are the powerful tool to follow magnetization dynamics completely, in respect of both coherent and incoherent relaxation processes and to determine the timescales of energy dissipation. Control of the optical excitation is achieved simply by varying the pump fluence. By varying the external field from in-plane to out-of-plane reveals new insight on the dominate relaxation modes.

The various precession modes are discussed for three regions of nickel layer thickness. The Kittel mode is present in all films. The magnetic moments in the entire sample precess in phase. Therefore, this mode has a wavevector $k = 0$. The standing spin-wave mode is observed for samples thicker than the optical penetration depth λ_{opt} of the pump laser. The wavevector \mathbf{k} is then determined from sample thickness. Nevertheless, even 2nd and 3rd order standing spin

waves are observed. Dipole modes dominate the magnetization dynamics of samples significantly thicker than λ_{opt} . Both the surface and volume dipole modes contribute to the spectra. The Damon-Eschbach mode laterally localized within the pump-laser spot and the backscattered volume modes of higher order are observed.

The magnetic damping is also discussed for various precession modes. The Gilbert damping parameter is found to be dependent on the precession mode. The standing spin-wave mode is more strongly damped than the Kittel $k = 0$ mode. The increased damping can be attributed to the additional energy dissipation from coherent to the incoherent mode conversion in spin waves with lower wavevectors. This assumption is confirmed by applying the external field towards the sample normal. This significantly reduces the two magnon scattering probability and causes the damping parameter of the standing spin-wave mode to approach the α value for the basic mode. The damping parameter of the Kittel mode is not significantly influenced by two magnon scattering.

The background in the time resolved spectra is found to have a magnetic origin. It results from the short wavelength magnons, which contribute to the magnetization spectra up to 1ns after excitation by the pump pulse. For strong excitation by the pump pulse, the magnon background decays exponentially within time. As seen in the micromagnetic simulations, this comes from the excitations of high energy magnons. Their short lifetime originates from the strong interaction with the Stoner band near the surface of the Brillouin zone. The high energy spin waves scatter into magnons with lower k vectors. A strongly excited state is observed when the pump fluence is higher than $50\text{mJ}/\text{cm}^2$ for the 50nm thin nickel sample. By reducing the sample thickness, less pump fluence is required to achieve the highly excited state. For small excitation power, the incoherent magnon background can be approximated by a linear function.

CHAPTER 6

The Gilbert damping parameter

The magnetization, disturbed from equilibrium by an intensive laser pulse, precesses around a magnetic field \mathbf{H} and tries to align with it on timescale τ_α , given by the macroscopic damping parameter α . The magnetization vector obeys the Landau-Lifshitz equation of motion:

$$\frac{d\mathbf{M}}{dt} = -\gamma_0 \mathbf{M} \times \mathbf{H} + \frac{\alpha}{M_s} \mathbf{M} \times \frac{d\mathbf{M}}{dt}, \quad (6.1)$$

with a Gilbert form of damping. This equation can be rewritten to the explicit equation for magnetization:

$$\frac{d\mathbf{M}}{dt} = -\frac{\gamma_0}{1 + \alpha^2} \mathbf{M} \times \mathbf{H} + \frac{\gamma_0 \alpha}{M_s (1 + \alpha^2)} \mathbf{M} \times (\mathbf{M} \times \mathbf{H}), \quad (6.2)$$

with a Landau-Lifshitz form of damping. Microscopically, the Landau-Lifshitz form of damping can be derived to agree with the principles of the statistical physics, contrary to the Gilbert form of damping. These slight differences between Landau-Lifshitz and Gilbert damping, explain the current induced domain wall motion experiments by Hayashi et al. [65, 66]. In this special case, the Gilbert form of damping does not imply energy minimization and introduces some additional non-adiabatic term in the equation of motion. The Landau-Lifshitz form of damping explains the experiment appropriately. This effect appears only for large magnetization precessions and has no relevance in our experiments. Therefore, the analysis in this work starts from Eq. 6.1, as presented in Chapter 2, and considers only the Gilbert damping parameter α .

This chapter presents the Gilbert damping parameter as follows: first, the microscopic origin of the damping is introduced with the associated classification of the magnetic dissipation processes. A detailed overview of the theories that

model the damping parameter is then presented. A comparison of the excitation mechanism by pump pulse for various samples gives the introduction to the experimental findings. To investigate non-local damping by emission of spin currents, double layers with nickel and various non-magnetic metals are compared in the same experimental conditions. The processes which contribute to the extrinsic magnetic damping are identified. Finally, the main experimental results, concerning the enhancement of the damping parameter due to the spin currents emission are presented for different samples and compared with the theoretical predictions.

6.1 Different origins of damping

Gilbert implemented the damping parameter α in the Landau-Lifshitz-Gilbert equation in analogy to a Rayleigh energy dissipation function, based on thermodynamic principles [67]. This work introduces the magnetic damping based on the Professor Föhnle's Lecture [67, 68]. To characterize the dissipation processes with the damping parameter, magnetization vector have to obey the known equation of motion. The equation of motion is appropriate for just one of the dynamic variables, while all other degrees of freedom are integrated out. This is why the damping is determined by energy and momentum transfer from the considered dynamic variable to the eliminated degrees of freedom. The Gilbert damping term in the Landau-Lifshitz-Gilbert equation is the first term in the evaluation of a non-local expression of the equation of motion.

The damping can be classified by the direction of energy transfer into indirect and direct. If energy is conserved within the magnetic system and redistributed between different magnetic degrees of freedom, the damping is indirect. Damping of spin waves by Stoner excitations and mode conversions are examples of indirect damping.

Direct damping specifies the transfer of energy from the magnetic system to the other nonmagnetic degrees of freedom, mainly the lattice. It originates from spin-orbit coupling, and can be classified into intrinsic and extrinsic direct damping. Magnon scattering on the unavoidable phonons determines the intrinsic damping. This is a material characteristic and cannot be reduced. Extrinsic damping is based on the additional magnon scattering from phonons, caused by defects and the geometry of the sample. The value of extrinsic damping can thus be strongly influenced by the sample pattern or by growth quality.

Dissipation of the magnetic energy by the above scattering processes considered can be characterized as a local process because scattering occurs in the ferromagnet itself. On the interfaces between the ferromagnet and other ferromagnets or normal metals, additional non-local scattering processes contribute to the damping. Emission of spin waves at the interface of two ferromagnets, or spin currents at the interface of a ferromagnet with a normal metal, leads to an increased energy dissipation. This additional non-local damping is strongly influenced by the adjacent layer thickness, since it occurs at the interfaces.

6.2 Theoretical modeling of damping

The derivation of the Gilbert damping parameter α is a challenging task for theorist. The direct signature of the damping is written in the equation of motion. Even without damping, there are no experimental variables that are constants of motion on the microscopic scale. Therefore, it is hard to define an appropriate equation of motion for the precessing magnetization. The choice of dynamic variables will primarily influence the quantity and the origin of the damping parameter. Magnetic damping is considered mainly within two types of theory.

The first class of theory is based on the direct transfer of magnetic energy to the lattice, mainly due to magnon-phonon scattering. Spin-orbit coupling is considered phenomenologically via magnetoelastic coupling between the magnetization, $\mathbf{M}(\mathbf{r}, t)$ and lattice strain, $\hat{\epsilon}(\mathbf{r}, t)$. The main damping mechanism is the scattering of magnons at phonons and defects.

The second class of the theory is based on the energy transfer from magnons to electrons and then to the lattice via electronic scattering. In this case, electrons inherit the magnetic moments from the spin waves, and then pass them to the lattice. The transfer from spin to electrons can be based on spin-current interactions (damping by Eddy currents), Coulomb interactions (Breathing Fermi Surface model) and magnon-electron interaction (s-d model for damping). Electronic scattering transfers energy and magnetic momentum from the electrons to the lattice.

The electronic scattering takes place between the spin-up and spin-down states, which are not orthogonal to each other due to spin-orbit coupling. This results in non-vanishing amplitudes of the scattering potential at inhomogeneities such as phonons or defects.

In order to explore different contributions to damping, electronic scattering is classified by the conservation of spin and the corresponding energy band, as follows.

- Ordinary scattering or scattering without a spin-flip describes transitions between states in different bands with the same spin. The transfer of momentum is relatively small.
- Spin-flip scattering describes transitions for which the initial and the final state have a different spin. A molecular field strongly reduces this effect in ferromagnets. The matrix elements of the spin-flip interactions are calculated by Yafet. Here, the transfer of the magnetic moment is quite large.
- Intraband scattering describes transitions between the states in the same energy band. For short relaxation times τ , this scattering dominates the damping processes and leads to a damping parameter proportional to the conductivity σ .

$$\alpha \propto \sigma \propto \tau.$$

- Interband scattering describes transitions between the states in different energy bands. Scattering relaxation times τ are large, and the main contribution to damping is proportional to the resistivity ρ :

$$\alpha \propto \rho \propto 1/\tau.$$

The most important models, which describe how to derive the damping of the precessing magnetization, are presented in the following sections. Damping by spin-flip scattering is an interesting but indirect approach to determine the damping parameter. The model includes the results of Yafet's and Elliot's work and explains the experimental results regarding damping from the 1970s well. The s-d current model and the Breathing Fermi surface model are two later complementary approaches on the newest state of theory. They belong to the second set of theories on damping, as classified above, in which the damping mechanism is based on the electronic scattering by phonons. All these theories consider only the near-adiabatic regime, and are therefore valid only for the magnetic relaxation of slow magnetic degrees of freedom. So far, there is no theory that considers magnetic damping in the high non-equilibrium phase in which the fast magnetic degrees of freedom and the Stoner excitations comprise the main damping mechanisms. Nevertheless, there is a remarkable approach by Koopmans et al.[69] to unify the characteristic damping scale of coherent precessions with the demagnetization time. Finally, the magnetostatic circuit theory approach is presented, which is used to determine the enhancement of the damping parameter from spin current emission.

6.2.1 Damping by spin-flip scattering

Kambersky was one of the first in the 1970s to explore the origin of the magnetic damping[70]. This chapter presents energy dissipation of the magnetization torque from spin-flip scattering of itinerant electrons. Damping is derived from the generalized damping term, which is directly related to the susceptibility of the system. This model includes contributions from different theories, such as spin-flip scattering in semiconductors by Yafet, or results of Elliot's theory of electronic scattering in metals. Experimental findings are presented at the end of the section.

Landau-Lifshitz-Gilbert equation describes the magnetization dynamics in an external magnetic field \mathbf{H} :

$$\frac{\partial \mathbf{M}}{\partial t} = -\gamma \mathbf{M} \times \left(\mathbf{H} - \frac{\lambda}{\omega_M^2} \cdot \frac{d\mathbf{M}}{dt} \right), \quad (6.3)$$

where γ denotes the magnetomechanical ratio, $\omega_M = \gamma M$, and λ is a damping constant. This is related with the Gilbert damping constant α by simple relation $\lambda = \alpha \omega_M^2 / \gamma M_s$. In the presence of a transverse harmonic field, the linear response of the ferromagnet results from the susceptibility:

$$\chi(\omega) = \frac{-\omega_M}{\omega - \omega_0 + i\lambda\omega/\omega_M}, \quad (6.4)$$

where ω denotes the modulation frequency of the external field and ω_0 is the eigenfrequency of the non-perturbed system. The damping constant λ is determined from Eq. 6.4 using the known susceptibility tensor $\chi(\omega)$. This macroscopic expression for the susceptibility can be derived from microscopic scattering processes. The macroscopic damping constant λ from Eq. 6.3 is related to the time constants for the relevant energy dissipation processes. Scattering of itinerant electrons followed by spin-flipping of scattered electrons is the main damping mechanism considered in this chapter. This process can be described by the Hamiltonian H_{sf} , given by:

$$H_{sf} = \sum_{k,q} (D_{k,q} c_{k,q\uparrow}^+ c_{k\downarrow} + D_{k,-q}^* c_{k\downarrow}^+ c_{k-q\uparrow}) (b_q + b_{-q}^+), \quad (6.5)$$

where $c_{k\sigma}$ and b_q describe electron and phonon creation operators, with wave vectors k and q respectively. $\hbar D_{k,q}$ are the matrix elements of the spin-flip interaction in a semiconductor, derived by Yafet[71].

The susceptibility can also be derived from the equations of motion for the creation, S^+ , and annihilation spin operator, S^- , using the retarded Green's functions, G , suggested by Zubarev[72]:

$$\begin{aligned} \chi(\omega) &= - \left(\frac{\gamma \hbar}{2} \right)^2 G(S^-, S^+, \omega) \\ \omega G(S^-, S^+, \omega) &= \langle [S^-, S^+] \rangle + G([S^-, H], S^+, \omega). \end{aligned}$$

Where H denotes the total Hamiltonian of the system, which includes the spin-flip scattering Hamiltonian H_{sf} . Square brackets $[\]$, denote a commutator while arrow brackets $\langle \ \rangle$ indicate the equilibrium mean value.

The damping mechanism includes decay of the collective excitations into phonon and band-electron excitations. The electron velocity is dominantly higher than the group velocity of phonons, which implies that the majority of energy transfer is to phonons and only a much smaller fraction transfers to band electrons.

The damping term Γ is derived from the previous equations. It has a complicated form as an integration of spin-flip scattering rates over the Fermi surface and is not explicitly written here. The damping parameter λ is simply related to the damping term by:

$$\Gamma = \lambda \frac{\omega}{\omega_M}.$$

The damping parameter λ is then derived as:

$$\lambda = \chi_P \Gamma_S,$$

where $\chi_P = \mu_B^2 Z_F$ represents the Pauli susceptibility, from the density of states at the Fermi level Z_F . Γ_S equals the "uncorrelated" spin-flip rate and relaxation time in a nonmagnetic band based on Yafet's calculations:

$$\Gamma_S = \frac{1}{2\pi} \int \left\langle \frac{|D_{k,q}|^2}{v} \right\rangle_F (2n_q + 1) q dq.$$

Arrow brackets, $\langle \rangle_F$, denote an average over the Fermi surface. v is the electron velocity and n_q is the occupation number for the states with wave vector q .

The previous equation can be further simplified according to the estimation of the Γ_S given by Elliot[73]:

$$\Gamma_S \approx (\delta g)^2 / \tau,$$

where δg is the deviation of the g factor from the free electron value and τ is the electron-phonon scattering time.

The final form of the damping parameter λ , derived from the previous equations, depends explicitly on the total density of states at the Fermi level, Z_F :

$$\lambda = \left(\frac{\gamma \hbar}{2} \right)^2 Z_F \frac{(g-2)^2}{\tau}. \quad (6.6)$$

The damping parameter λ , due to the spin-flip scattering, is inversely proportional to the electron-phonon scattering time τ . Hence, it is expected that λ increases with increasing temperature.

The damping parameters of iron and nickel, based on the previously described mechanism, is estimated at about $4 \cdot 10^7 \text{s}^{-1}$ and $2 \cdot 10^8 \text{s}^{-1}$, respectively. Heinrich and Frait[74] measured damping parameters of nickel and iron films by the ferromagnetic anti-resonance (FMAR) in microwave transmission experiments: $\lambda(Fe) = 3 \cdot 10^7 \text{s}^{-1}$ and $\lambda(Ni) = 3 \cdot 10^8 \text{s}^{-1}$. Furthermore with increasing temperature, iron shows an almost linear increase of the damping parameter at temperatures around 420K, as predicted by Eq. 6.6. Nickel samples, however, show no temperature dependence of the damping parameter for a wide temperature range from 200K up to 500K, implying that the spin-flip scattering on phonons is the dominating damping term in iron and a less important factor in nickel.

6.2.2 s-d current model

Conduction electrons with energies near the Fermi surface carry spin-dependent transport processes. Localized electrons with energies far below the Fermi level determine the magnetization dynamics. Magnetization of both conduction and localized electrons is considered without orbital moments. The damping mechanism is based on the electronic scattering of conduction electrons only. Theory presented in this section is based on [67, 75, 76].

The localization of d electrons leads to localized magnetic moments, which are now able to polarize conduction electrons. Therefore, both d ($\mathbf{M}_d(\mathbf{r}, t)$) and s electrons ($\mathbf{m}_s(\mathbf{r}, t)$) contribute to the magnetization \mathbf{M} :

$$\mathbf{M}(\mathbf{r}, t) = \mathbf{M}_d(\mathbf{r}, t) + \mathbf{m}_s(\mathbf{r}, t) . \quad (6.7)$$

Fig. 6.1 shows the orientation of both magnetizations for a homogeneous FMR mode. With no spin-flip scattering of conduction electrons, the d electrons and s electrons align from the $s-d$ exchange interaction and precess in phase.

With spin-flip scattering of conduction electrons, part of the magnetization of s electrons $\delta\mathbf{m}_s$ will be orientated perpendicular to \mathbf{M}_d . The s and d magnetic moments are then not aligned. This induces an extra torque, perpendicular to the precessing d magnetization, which tries to align the s magnetization with the precessing d moments. The conduction s electrons follow the d electrons with a phase delay. This causes additional damping which increases for larger spin-flip rates.

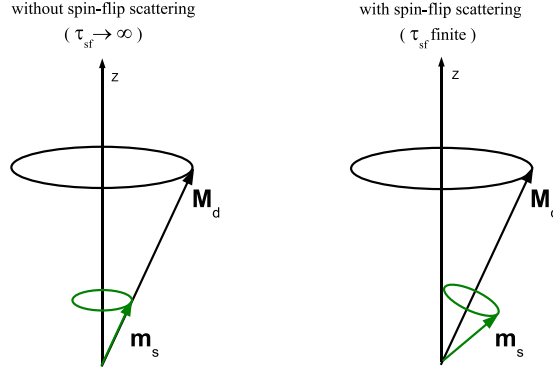


Figure 6.1: $s-d$ model of a homogeneous FMR mode: orientations of the magnetizations of s and d electrons

The Gilbert equation of motion for the magnetic moment of d electrons is a starting point of this model:

$$\frac{d\mathbf{M}_d}{dt} = -\gamma(\mathbf{M}_d \times \mathbf{H}_{eff,d}) + \frac{1}{M_d} \mathbf{M}_d \times \alpha \frac{d\mathbf{M}_d}{dt} + \mathbf{T}. \quad (6.8)$$

The $\mathbf{H}_{eff,d}$ is the effective field influencing the d electrons. The second term describes the direct damping of the d electrons, and the last term represents an additional torque due to scattering of conduction electrons. The torque \mathbf{T} originates from the non-colinearity of \mathbf{m}_s and \mathbf{M}_d and can be expressed as:

$$\mathbf{T} = -\frac{1}{\tau_{ex} M_d} \mathbf{M}_d \times \mathbf{m}_s, \quad (6.9)$$

with τ_{ex} as the period of precession of \mathbf{m}_s around \mathbf{M}_d . To calculate the induced magnetization \mathbf{m}_s of the s electrons, the continuity equation has to be applied:

$$\frac{\partial \mathbf{m}_s(\mathbf{r}, t)}{\partial t} + \nabla \cdot \mathfrak{S} = -\mathbf{T} - \Gamma_{rel},$$

where \mathfrak{S} is the expectation value of the spin-current density tensor operator and Γ_{rel} represents the spin relaxation term due to spin-flip scattering. The four main contributions to the torque \mathbf{T} are derived from Eq. 6.8. Two of them originate from the d electron magnetization variation in time and the other two come from the spatial variation of \mathbf{M}_d and the transport current.

Considering these terms, which are not explicitly stated here, Eq. 6.8 can be simplified to an equation of the Gilbert type:

$$\frac{d\mathbf{M}_d}{dt} = -\gamma(\mathbf{M}_d \times \mathbf{H}_{eff,d}) + \frac{1}{M_d} \mathbf{M}_d \times \alpha' \frac{d\mathbf{M}_d}{dt}$$

with a renormalized gyromagnetic ratio γ and the damping parameter α' . Without transport current of electrons, γ and α' are expressed as follows:

$$\gamma = \frac{\gamma}{1 + \eta} \quad (6.10)$$

$$\alpha' = \frac{\alpha + \xi\eta}{1 + \eta}. \quad (6.11)$$

The parameters ξ and η are defined as $\xi = \tau_{ex}/\tau_{sf}$ and $\eta = m_s^0 ((1 + \xi^2)M_d)^{-1}$. τ_{sf} represents the spin-flip time of conduction electrons, and m_s^0 represents the adiabatic part of induced magnetization in conduction electrons, \mathbf{m}_s . Fig. 6.2

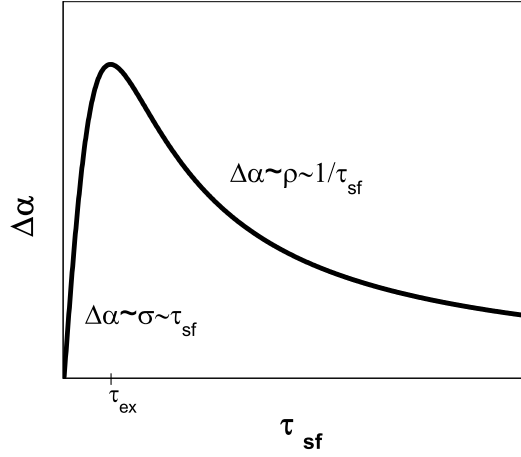


Figure 6.2: Additional damping in metals versus the spin-flip time of the conduction electrons

shows the two main regimes of the damping parameter with respect to the spin-flip scattering time of the conduction electrons. Eq. 6.12 gives the limit values of the damping parameter for infinitely small and infinitely large spin-flip scattering times. For lower spin-flip scattering times, the damping parameter is directly proportional to the spin flip scattering time, τ_{sf} . For higher spin-flip scattering times (overcritical damping), α is inversely proportional to τ_{sf} . Thus,

$$\alpha' = \left(\alpha + \frac{\tau_{ex}}{\tau_{sf}} \cdot \frac{m_s^0}{1 + \left(\frac{\tau_{ex}}{\tau_{sf}}\right)^2 M_d} \right) \left(1 + \frac{m_s^0}{1 + \left(\frac{\tau_{ex}}{\tau_{sf}}\right)^2 M_d} \right)^{-1}$$

$$\tau_{sf} \rightarrow 0 \Rightarrow \alpha' \rightarrow \alpha + \frac{\tau_{sf}}{\tau_{ex}} \cdot \frac{m_s^0}{M_d}$$

$$\tau_{sf} \rightarrow \infty \Rightarrow \alpha' \rightarrow \alpha + \left(2\alpha + \frac{m_s^0}{M_d} \right) \frac{\tau_{ex}}{\tau_{sf}}.$$

A higher spin flip rate ($\tau_{ex} \gg \tau_{sf}$, $\alpha \propto \tau_{sf}$) implies, that the transfer of angular momentum to the lattice will be fast. Further more, the energy dissipation will be faster and the damping parameter will be larger for a higher spin-flip relaxation rate.

In the low spin-flip rate regime ($\tau_{ex} \ll \tau_{sf}$) the origin of damping is the same as it is in the model for non-local damping by spin currents at the interface of the ferromagnet and normal metal described by Tserkovnyak et al.[77], (See Section 6.2.4). The precessing magnetization in the ferromagnetic layer induces spin current and spins are "pumped" into the normal metal layer. The spin polarization of the conduction electrons is conserved for a long time and leads to the conduction electrons damping of the magnetization in the normal metal layer. In the $s - d$ model, the spins are "pumped" into their own delocalized states rather than delocalized states outside the ferromagnet.

If the spin-flip scattering time scales monotonically with the temperature, then the dependence $\alpha(\tau_{sf})$ can be interpreted as follows: At lower temperatures and smaller spin-flip relaxation times, the damping parameter is proportional to the conductivity σ . At higher temperatures and larger spin-flip relaxation times, α is proportional to the resistivity ρ . Experiments have shown that the temperature dependence of α includes contributions proportional to the conductivity and resistivity. Experiments on pure nickel samples with FMAR (ferromagnetic anti-resonance) showed, that the experimentally determined damping parameter fits perfectly with the model composed of two damping contributions[78]. One of them is proportional to the conductivity and dominates at lower temperatures while the other is proportional to the resistivity and dominates at higher temperatures. The universality of this law could not be confirmed by measurements in other ferromagnetic materials.

For transition metals the $s - d$ model predicts typical values of the damping parameter $\Delta\alpha \propto 10^{-5} - 10^{-3}\text{s}^{-1}$. Experimental values are more on the order of 10^{-2}s^{-1} . The model underestimates the energy dissipation of the precessing magnetization by neglecting the d electrons contribution to damping and results in a much smaller Gilbert parameter α than experimentally determined.

The $s - d$ model adequately describes the effect of current transport in a metal. To describe damping quantitatively, it is applied to metallic systems with $3d$ or $4f$ impurities, but not to transition metals. d electrons scattering then becomes significant contribution to damping and cannot be neglected. The Breathing Fermi surface model, in contrast, considers the damping mechanism from scattering both s and d electrons on equal footing. This is presented in detail in the following chapter.

6.2.3 The breathing Fermi surface model

Dipolar, Zeeman and spin-orbit interaction energies determine the Fermi surface of a ferromagnet in an external magnetic field. Fig. 6.3 presents the transformations of the Fermi surface in an external electric and magnetic field. Changes in the magnetization direction during the precession of magnetization or prop-

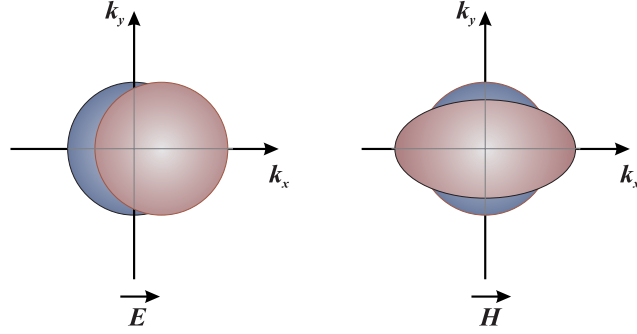


Figure 6.3: Deformations of Fermi surface in an external electric and magnetic field

agation of spin waves cause deformations of the Fermi surface from spin-orbit interaction[79]. The electrons near the Fermi surface try to repopulate the changing Fermi sea by scattering. The energy redistribution of scattered electrons introduces damping. The model does not identify the microscopic mechanisms of the spin energy dissipation. This is incorporated by the phenomenological electron relaxation times.

Kambersky introduced this new approach to the theory of magnetic damping in the 1970s[70]. It includes energy estimations based on Clogston's "valence-exchange" semiclassical method in ferrites. Fähnle and his coworkers further improved the model by introducing the *ab initio* density-functional electron theory with a single electron description[67, 80]. Results of their work are presented below.

In effective single-particle theory, the electron in a band with the index j and a wavevector \mathbf{k} is described by a spinor wavefunction $\Psi_{j\mathbf{k}}$. The orbital momentum in metals is mostly quenched by molecular fields. The spin magnetization density at point \mathbf{r} and time t is:

$$\mathbf{m}_s(\mathbf{r}, t) = -\frac{g\mu_B}{2} \sum_{j, \mathbf{k}, s, s'} n_{j, \mathbf{k}}(t) \Psi_{j\mathbf{k}s}^*(\mathbf{r}, t) \hat{\sigma}_{ss'} \Psi_{j\mathbf{k}s'}(\mathbf{r}, t), \quad (6.12)$$

where $n_{j\mathbf{k}}$ is the occupation number for the electronic state, $j\mathbf{k}$, $\hat{\sigma}_{ss'}/2$ is the spin operator and $\Psi_{j\mathbf{k}s}$ is the corresponding spin component of the spinor $\Psi_{j\mathbf{k}}$. The band structure energy is the sum of the single electron energies $\epsilon_{j\mathbf{k}}$,

$$E_{band}(t) = \sum_{j\mathbf{k}} n_{j\mathbf{k}}(t) \langle \Psi_{j\mathbf{k}}(t) | \hat{H} | \Psi_{j\mathbf{k}}(t) \rangle = \sum_{j\mathbf{k}} n_{j\mathbf{k}}(t) \epsilon_{j\mathbf{k}}(t),$$

where \hat{H} represents the effective single-particle Hamiltonian in the density-functional theory.

The adiabatic approximation is introduced here. The time dependent wavefunction $\Psi_{j\mathbf{k}s}(\mathbf{r}, t)$ is not a solution to the time dependent wave equation, but a solution to the time independent wave equation for the effective potential which depends on the momentary directions of the atomic magnetic moments $\{\mathbf{e}_i(t)\}$.

Therefore, the wavefunction, single electron energies and occupation numbers also depend on the orientation of the atomic magnetic moments:

$$\begin{aligned}\Psi_{j\mathbf{k}}(\mathbf{r}, t) &= \Psi_{j\mathbf{k}}(\mathbf{r}, \{\mathbf{e}_i(t)\}) \\ \epsilon_{j\mathbf{k}}(t) &= \epsilon_{j\mathbf{k}}[\{\mathbf{e}_i(t)\}] \\ n_{j\mathbf{k}}(t) &= f(\epsilon_{j\mathbf{k}}(\{\mathbf{e}_i(t)\})) = f_{j\mathbf{k}}(t) .\end{aligned}$$

$f_{j\mathbf{k}}$ are the Fermi-Dirac equilibrium occupation numbers, appropriate for the Fermi energy $\epsilon_F[\{\mathbf{e}_i(t)\}]$ and the corresponding Fermi surface.

$\epsilon_{j\mathbf{k}}$ depends on $\{\mathbf{e}_i\}$ because of spin-orbit coupling, even for a homogeneous magnetization. Small changes of $\{\mathbf{e}_i\}$ in time induce variations in $\Psi_{j\mathbf{k}}$, $\epsilon_{j\mathbf{k}}$ and ϵ_F and the Fermi surface itself. This small modification of the Fermi surface from the direction change of the atomic magnetic moments give meaning to the breathing Fermi Surface model.

Changes in the shape of the Fermi surface cause electron scattering, in which electrons try to repopulate the Fermi sea. These scattering processes provoke temporal change in the occupation numbers. In a strictly adiabatic approximation, $n_{j\mathbf{k}}$ is equivalent to the equilibrium Fermi-Dirac distribution at all times. The Breathing Fermi surface model allows $n_{j\mathbf{k}}$ to follow $f_{j\mathbf{k}}$ with the characteristic relaxation time $\tau_{j\mathbf{k}}$ for the corresponding electronic state $j\mathbf{k}$:

$$\frac{dn_{j\mathbf{k}}(t)}{dt} = -\frac{1}{\tau_{j\mathbf{k}}} [n_{j\mathbf{k}}(t) - f_{j\mathbf{k}}(t)]. \quad (6.13)$$

In this slightly non-adiabatic situation, for very small relaxation times $\tau_{j\mathbf{k}}$ (in comparison with the time needed for the changes of the momentary directions \mathbf{e}_i), the previous relaxation ansatz can be simplified to

$$n_{j\mathbf{k}}(t) = f_{j\mathbf{k}}(t) - \tau_{j\mathbf{k}} \frac{df_{j\mathbf{k}}(t)}{dt}.$$

In the strictly adiabatic approximation, the equation of motion is:

$$\frac{d\mathbf{M}}{dt} = -\gamma \mathbf{M} \times \mathbf{H}_{eff}, \quad (6.14)$$

with an adiabatic effective field

$$\mathbf{H}_{eff} = -\frac{1}{M} \cdot \frac{\delta E}{\delta \mathbf{e}_i}. \quad (6.15)$$

There is no energy dissipation in this regime. In the slightly nonadiabatic situation, the following assumption is valid:

$$\mathbf{H}_{eff} = -\frac{1}{M} \cdot \frac{\delta F_{dis}}{\delta \mathbf{e}_i},$$

where F_{dis} denotes the dissipative free-energy magnetization functional. Föhnle constructed this in analogy to the band energy functional by including Eq.6.13:

$$\mathbf{H}_{eff} = -\frac{1}{M} \sum_{j,\mathbf{k}} n_{j\mathbf{k}}(e(t)) \frac{\partial \epsilon_{j\mathbf{k}}(e(t))}{\partial \mathbf{e}}.$$

The effective magnetic field can be divided into the anisotropy field, which gives non-dissipative precession, and the damping field, which determines the energy dissipation processes.

$$\begin{aligned} \mathbf{H}_{eff} &= \mathbf{H}_{ani} + \mathbf{H}_{damp} \\ \mathbf{H}_{ani} &= -\frac{1}{\gamma M} \sum_{j,\mathbf{k}} f_{j\mathbf{k}} \frac{\partial \epsilon_{j\mathbf{k}}(\mathbf{e})}{\partial \mathbf{e}} \\ \mathbf{H}_{damp} &= -\frac{1}{\gamma M} \boldsymbol{\alpha} \cdot \frac{d\mathbf{M}}{dt} \end{aligned}$$

The damping matrix $\boldsymbol{\alpha}$ is defined as

$$\alpha_{lm} = -\frac{1}{\gamma M} \sum_{j\mathbf{k}} \tau_{j\mathbf{k}} \frac{\partial f_{j\mathbf{k}}}{\partial \epsilon_{j\mathbf{k}}} \frac{\partial \epsilon_{j\mathbf{k}}}{\partial e_l} \frac{\partial \epsilon_{j\mathbf{k}}}{\partial e_m}. \quad (6.16)$$

The expression is similar to Drude's conductivity tensor σ ,

$$\sigma_{lm} = -e_0^2 \sum_{j\mathbf{k}} \tau_{j\mathbf{k}} \frac{\partial f_{j\mathbf{k}}}{\partial \epsilon_{j\mathbf{k}}} \frac{\partial \epsilon_{j\mathbf{k}}}{\partial k_l} \frac{\partial \epsilon_{j\mathbf{k}}}{\partial k_m}. \quad (6.17)$$

The relaxation time $\tau_{j\mathbf{k}}$ for processes at the Fermi surface should be independent of state $j\mathbf{k}$, $\tau_{j\mathbf{k}} = \tau$. The main temperature dependence of both $\boldsymbol{\alpha}$ and $\boldsymbol{\sigma}$ comes from the temperature dependence of τ . The relaxation time τ can be determined from the corresponding conductivity measurements. For metals it decreases roughly with T^2 as temperature decreases to a limit determined by the residual resistivity. Experimentally, the temperature dependence of α implies that damping has contributions proportional to the conductivity and resistivity[78].

The main difference between the Kambersky and Föhnle model is in how the damping matrix $\boldsymbol{\alpha}$ is calculated. Kambersky divided contributions to damping into those from the degenerate and non-degenerate bands. For nearly degenerate states, only states of the "hole-pockets" on the Fermi surface are considered. The contribution from the large non-degenerate bands is estimated from the spin-orbital perturbation energy. The damping parameter in Kambersky's model is then

$$\alpha = \frac{\gamma}{4M} Z_F \lambda_{SO}^2 (g-2)^2 \tau, \quad (6.18)$$

where Z_F denotes the density of states at the Fermi level and λ_{SO} is the spin-orbit coupling constant.

Fähnle further developed the model by including the damping matrix α in the equation of motion Eq. 6.14. The new equation of motion is of the Gilbert type for homogeneous magnetization. Only the damping scalar α is replaced by damping matrix α .

$$\frac{d\mathbf{M}}{dt} = -\gamma\mathbf{M} \times \mathbf{H}_{ani} + \frac{1}{M}\mathbf{M} \times \left(\alpha \cdot \frac{d\mathbf{M}}{dt} \right). \quad (6.19)$$

The damping matrix depends on the orientation of the magnetization. For magnetization oriented along z-direction, it has the following form:

$$\alpha = \begin{pmatrix} a^2 & ab & 0 \\ ab & b^2 & 0 \\ 0 & 0 & 0 \end{pmatrix}. \quad (6.20)$$

In general, the magnetization change vector $d\mathbf{M}/dt$ is not parallel to the damping field \mathbf{H}_{damp} . The Gilbert equation derives from Eq. 6.19 for the special case when $d\mathbf{M}/dt$ corresponds to the eigenvectors of the damping matrix α . The Gilbert damping parameter α is then represented by the eigenvalues $\alpha_{1,2}$ of the damping matrix α . When magnetization is aligned parallel to a threefold or fourfold symmetry axis, Eq. 6.19 again reduces to the Gilbert equation. In bulk samples the damping matrix already has two different eigenvalues. For systems with reduced dimensionality the difference between α_1 and α_2 is even more pronounced. In monatomic layers and wires, damping parameters can even be zero for one specific magnetization orientation. Fig. 6.4 presents the

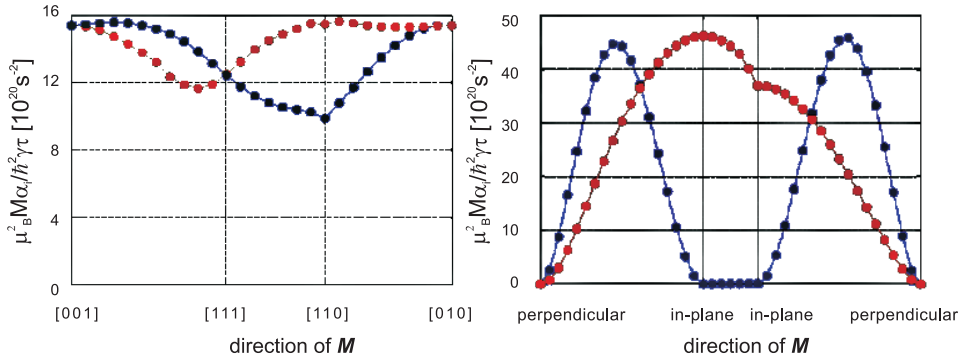


Figure 6.4: Breathing Fermi surface model: two eigen values of α for nickel for a) bulk sample and b) monatomic layer[80].

two damping matrix eigenvalues in bulk nickel sample and nickel monolayer. This method might offer a new approach to optimize trajectories of precessing magnetization in nanostructured devices in future spintronics.

The damping is mainly assumed to be dependent on the magnetic anisotropy: the larger the damping parameter, the larger the magnetic anisotropy. The breathing Fermi surface model implies that there is no simple relation between damping and anisotropy fields. The anisotropy is linearly dependent on the derivatives $\partial\epsilon_{j\mathbf{k}}/\partial e$, which effectively compensate for each other in the sum in Eq. 6.16. On the other hand, by calculating diagonal components of the damping matrix α , those derivatives contribute quadratically to the sum in Eq. 6.16, which tangles the simple relation between α and \mathbf{H}_{ani} .

Fähnle also included the contribution of orbital moments to the magnetization in the breathing Fermi surface model. The details can be found in [80].

Only the scattering of electrons near the Fermi surface is considered within this model, which means that only intraband scattering contributes to the damping. Relaxation of hot electrons, which are optically excited in much higher energy bands, dominate the demagnetization process in femtosecond pump-probe experiments. The near adiabatic regime, assumed in the breathing Fermi surface model, cannot be applied in this case. Therefore, this model can be applied only on the sub-ns timescale of magnetization dynamics in pump-probe experiments.

6.2.4 Non-local damping

Only local damping mechanisms are considered in the previous models, in which magnetization energy dissipates within the electron and phonon system of the ferromagnet itself. This chapter presents the theory of the non-local damping. Magnetic energy dissipates from the ferromagnetic to the neighboring nonmagnetic layer. The magnetization torque in the ferromagnet causes emission of a spin current at the interface with the normal metal. These spins transfer angular momentum to the normal metal layer and enhance the damping parameter. The transport theory approach is applied to characterize this damping enhancement for different multilayer structures[77, 81–84].

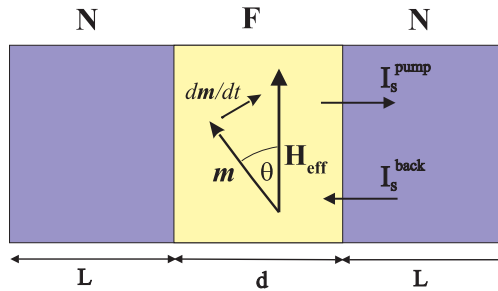


Figure 6.5: Non-local damping in trilayer N/F/N: N denotes normal metal layers with electrochemical potential μ . F denotes ferromagnetic layer with precessing magnetization m and with thickness d

The dissipation term is based on spin dependent scattering at the interface between the ferromagnet and the normal metal layer. It is derived for the model structure N/F/N, in which the ferromagnetic layer is embedded into

the normal metal medium. Spin pumping to the nonmagnetic layer is then characterized based on the properties of the ferromagnet, F, and normal metal, N.

The Gilbert equation of motion for the magnetic unit vector $\mathbf{m} = \mathbf{M}/M$, in which the non-local dissipation processes are neglected, is:

$$\partial_t \mathbf{m} = -\gamma_0 \mathbf{m} \times \mathbf{H}_{eff} + \alpha_0 \mathbf{m} \times \partial_t \mathbf{m} , \quad (6.21)$$

with an effective magnetic field \mathbf{H}_{eff} derived from the free energy F

$$\mathbf{H}_{eff} = -\partial_{\mathbf{m}} F(\mathbf{m})$$

and a damping constant α_0 . Fig. 6.5 shows a trilayer, N/F/N. F denotes the ferromagnetic layer of thickness d while N denotes the normal metal layer of thickness L . θ is the azimuthal magnetization angle. The energy change due to the scattering at the N/F interface is:

$$E(L, \theta) = \frac{1}{2\pi i} \int_{-\infty}^{\epsilon_F} \epsilon \frac{\partial}{\partial \epsilon} \ln \det \mathbf{s}(L, \theta, \epsilon) d\epsilon ,$$

where \mathbf{s} denotes the scattering matrix of the trilayer N/F/N. The summation is over all energies up to the Fermi energy ϵ_F .

The precession of the magnetization in the ferromagnet induces an exchange torque τ , which acts on the spins. τ is responsible for the angular momentum transfer by electron spins from the ferromagnet into the normal metal. In non-equilibrium situations, it is the derivative of the energy change over the magnetization precession angle θ :

$$\tau = -\frac{\partial}{\partial \theta} E(L, \theta) .$$

The conservation of angular momentum demands that τ corresponds to the spin injection current \mathbf{I}_s . Slonczewski[85] incorporates the spin-current effect on the magnetization dynamics using the additional term in the equation of motion:

$$\partial_t \mathbf{m} = -\gamma_0 \mathbf{m} \times \mathbf{H}_{eff} + \alpha_0 \mathbf{m} \times \partial_t \mathbf{m} + \frac{\gamma_0}{M_s V} \mathbf{I}_s . \quad (6.22)$$

V denotes the volume and M_s is the saturation magnetization of a ferromagnet.

The spin-dependent scattering for electrons from the normal metal layers at the interface is described by scattering matrix, \mathbf{s} :

$$\mathbf{s} = \begin{pmatrix} \mathbf{r} & \mathbf{t}' \\ \mathbf{t} & \mathbf{r}' \end{pmatrix} .$$

$\mathbf{r}(\mathbf{r}')$ and $\mathbf{t}(\mathbf{t}')$ denote the reflection and transmission matrices of the right(left) normal metal layer. The matrix elements $r_{nn'}^\sigma$ and $t_{nn'}^\sigma$ are the reflection and transmission amplitudes for spin-resolved incoming n and outgoing n' states

at energy ϵ and spin orientation σ . The scattering matrix depends on the magnetization direction \mathbf{m} over the projection matrices $\hat{\mathbf{u}}^\uparrow$ and $\hat{\mathbf{u}}^\downarrow$:

$$\hat{\mathbf{u}}^{\uparrow(\downarrow)} = \frac{1}{2} (\hat{\boldsymbol{\sigma}}_0 \pm \hat{\boldsymbol{\sigma}} \cdot \mathbf{m})$$

$$\hat{s}_{nn',ll'} = s_{nn',ll'}^\uparrow \hat{\mathbf{u}}^\uparrow + s_{nn',ll'}^\downarrow \hat{\mathbf{u}}^\downarrow.$$

$\hat{\boldsymbol{\sigma}}_0$ is the 2x2 unit matrix and $\hat{\boldsymbol{\sigma}} = (\hat{\sigma}_x, \hat{\sigma}_y, \hat{\sigma}_z)$ is the Pauli matrices vector. The conductance parameters are grouped into two pairs of 2x2 matrices, \mathbf{g} and \mathbf{t} , defined by:

$$g^{\sigma\sigma'} = \sum_{nn'} \left[\delta_{nn'} - r_{nn'}^\sigma (r_{nn'}^{\sigma'})^* \right] \quad (6.23)$$

$$t^{\sigma\sigma'} = \sum_{nn'} t_{nn'}^\sigma (t_{nn'}^{\sigma'})^*, \quad (6.24)$$

where the summation over n' denotes all channels in the right normal metal layer while the summation over n denotes all channels in the right lead in Eq. 6.23 and left lead in Eq. 6.24. All scattering coefficients and corresponding conductance parameters are evaluated at ϵ_F .

In general, the mixing conductance coefficients, $g^{\uparrow\downarrow}$ and $t^{\uparrow\downarrow}$, are the complex quantities with real part $g_r^{\uparrow\downarrow}$, $t_r^{\uparrow\downarrow}$, and with imaginary part $g_i^{\uparrow\downarrow}$, $t_i^{\uparrow\downarrow}$:

$$g^{\uparrow\downarrow} = g_r^{\uparrow\downarrow} + i g_i^{\uparrow\downarrow}$$

$$t^{\uparrow\downarrow} = t_r^{\uparrow\downarrow} + i t_i^{\uparrow\downarrow}.$$

The precession of magnetization in the ferromagnet triggers emission of spin currents \mathbf{I}_s into the normal metal layer. Total current consists of the DC current I_s^0 , current due to imported spins from the ferromagnet I_s^{pump} , and current returned back to the ferromagnet I_s^{back} :

$$\mathbf{I}_s = \mathbf{I}_s^0 + \mathbf{I}_s^{pump} + \mathbf{I}_s^{back}. \quad (6.25)$$

For the case without net current flow through the structure the DC contribution in Eq. 6.25 can be neglected. The current at the interface with right normal metal resulting from spins injected from the ferromagnet is:

$$\mathbf{I}_{s,R}^{pump} = \frac{\hbar}{4\pi} \left(A_r^{\uparrow\downarrow} \mathbf{m} \times \frac{d\mathbf{m}}{dt} + A_i^{\uparrow\downarrow} \frac{d\mathbf{m}}{dt} \right), \quad (6.26)$$

where $A^{\uparrow\downarrow}$ denotes the spin pumping coefficient

$$A^{\uparrow\downarrow} = A_r^{\uparrow\downarrow} + i A_i^{\uparrow\downarrow} = g^{\uparrow\downarrow} - t^{\uparrow\downarrow}. \quad (6.27)$$

If the magnetization is constant over time, e.g. $d\mathbf{m}/dt = 0$, there is no spin current emission. The spin pumping strength is determined from the $A^{\uparrow\downarrow}$ coefficient. It comprises contributions from reflected electrons from the right metal

layer and transmitted electrons from the left metal layer. For ferromagnetic layers thicker than the spin coherence length λ_{sc} ,

$$d > \lambda_{sc} = \frac{\pi}{k_F^\uparrow - k_F^\downarrow} \quad (6.28)$$

where $k_F^\uparrow(k_F^\downarrow)$ represents the spin-dependent Fermi wave vectors. The conductance coefficient from transmitted electrons $t^{\uparrow\downarrow}$ can be neglected. For transition metals the coherence length is on the order of the lattice constant, a few Å. Therefore, the condition in Eq. 6.28 is fulfilled for all experiments in magnetization dynamics. The spin pumping coefficient $A^{\uparrow\downarrow}$ is equivalent to the DC conductance parameter $g^{\uparrow\downarrow}$. As shown in [86], the imaginary part $g_i^{\uparrow\downarrow}$ of the conductance parameter is much smaller than the real part $g_r^{\uparrow\downarrow}$ for realistic F/N interfaces. Therefore,

$$A^{\uparrow\downarrow} \approx g^{\uparrow\downarrow} \approx g_r^{\uparrow\downarrow} .$$

To simplify future analysis, one of the normal metal layers can be fully neglected leaving only one F/N interface for consideration.

The spins, which are pumped out from the ferromagnet, can accumulate at the F/N interface or relax through spin-flip scattering. The current that is returned back to the ferromagnet \mathbf{I}_s^{back} is governed by the spin accumulation at the interface and depends on the properties of the normal metal layer. Implicitly it is:

$$\mathbf{I}_s^{back} = -\beta g_r^{\uparrow\downarrow} \mathbf{I}_s , \quad (6.29)$$

with the "backflow" factor β defined by

$$\beta \equiv \frac{\tau_{sf} \delta_{sd} / \hbar}{\tanh(L / \lambda_{sd})} .$$

λ_{sd} is the spin-flip diffusion length and δ_{sd} denotes the effective energy-level spacing of the states that participate in the spin-flip scattering.

The derived results for spin current \mathbf{I}_s are incorporated into the equation of motion Eq. 6.22. Thus, the precessing magnetization \mathbf{m} in the trilayer N/F/N obeys:

$$\partial_t \mathbf{m} = -\gamma_0 \mathbf{m} \times \mathbf{H}_{eff} + \left(\alpha_0 + \frac{\gamma_0 \hbar}{4\pi M_s V} \frac{g_r^{\uparrow\downarrow}}{1 + \beta g_r^{\uparrow\downarrow}} \right) \mathbf{m} \times \partial_t \mathbf{m} . \quad (6.30)$$

The additional damping term originates from the energy dissipation due to non-local damping processes at the N/F interface and depends directly on the mixing interface conductance $g_r^{\uparrow\downarrow}$. The real part of the mixing conductance is expressed as:

$$g_r^{\uparrow\downarrow} = \frac{1}{2} \sum_{nn'} \left| r_{nn'}^\uparrow - r_{nn'}^\downarrow \right|^2 ,$$

and is always positive. Therefore the damping is enhanced through spin current emission by

$$\Delta\alpha = \frac{\gamma_0 \hbar}{4\pi M_s V} \frac{g_r^{\uparrow\downarrow}}{1 + \beta g_r^{\uparrow\downarrow}} . \quad (6.31)$$

The non-local damping strength is defined by $g_r^{\uparrow\downarrow}$ and the factor β . The largest damping enhancement is observed when $\beta \rightarrow 0$, which means, that there is no back scattered spin current or that it can be neglected. When \mathbf{I}_s^{back} becomes significant, $\Delta\alpha$ reduces from the maximum value. In the other extreme when $\beta \gg 1/g^{\uparrow\downarrow}$ there is no damping enhancement at all. The spin current, which is pumped to the normal metal layer, is then completely returned back to the ferromagnet.

For most metals with a low impurity concentration, the factor β can be estimated as:

$$\beta = \left(2\pi N_{ch} \sqrt{\frac{\epsilon}{3}} \tanh(L/\lambda_{sd}) \right)^{-1},$$

where N_{ch} denotes the number of transverse channels in the normal metal and ϵ is the spin-flip probability at each scattering. N_{ch} in the first approximation is estimated from the conductance parameter $g_r^{\uparrow\downarrow} \approx N_{ch}$. The enhancement of the damping parameter is then

$$\Delta\alpha = \frac{\gamma_0 \hbar}{4\pi M_s V} g_r^{\uparrow\downarrow} \left(1 + \pi \sqrt{\frac{\epsilon}{3}} \tanh(L/\lambda_{sd}) \right)^{-1}. \quad (6.32)$$

The maximal $\Delta\alpha$ is found for normal metal layers with a high spin-flip probability and film thickness of at least double the spin-diffusion length. Normal metal layers with those features represent ideal spin sinks. The spin-flip relaxation rate is then high enough to overcome spin accumulation at the interface with the normal metal. The rough estimation of the spin-flip relaxation time τ_{sf} is

$$\frac{1}{\tau_{sf}} \propto Z^4,$$

where Z represents the atomic number. The heavier materials, with $Z \geq 50$ and p or d electrons in the conduction band, have a spin-flip probability $\epsilon \geq 10^{-1}$, making them ideal spin sinks. Therefore, large damping parameter enhancement is expected for N/F films in which the normal metal layer is Pd or Pt. In contrast, for light materials such as Al and Cu and heavier metals with only s electrons in the conduction band such as Ag, Au or Ta, the spin-flip probability is considerably smaller, $\epsilon \leq 10^{-2}$, making them less effective spin sinks. To reduce the spin accumulation at the N/F interface, the thickness L of the normal metal layer should be a couple of times higher than λ_{sd} . Due to the saturating behavior for the $\tanh(x)$ function for $x > 3$, further enhancement of $\Delta\alpha$ from increasing the L , is sparing.

On the other hand, Eq. 6.32 implicates that the ferromagnetic layer must be kept small in volume to observe additional damping from spin current emission. This is not completely true. The spin current is pumped through the entire cross section of the F/N interface, so the spin-current induced damping cannot be dependent on this quantity. The spin pumping coefficient A should be replaced by the more appropriate normalized interface conductance parameter G , which is normalized to the cross section S of the F/N interface,

$$G^{\uparrow\downarrow} = \frac{A^{\uparrow\downarrow}}{S},$$

in units of $\Omega^{-1}\text{m}^{-2}$. The enhanced damping parameter α for the ideal spin sink, is then

$$\alpha = \alpha_0 + \Delta\alpha = \alpha_0 + \frac{\gamma_0 \hbar}{4\pi M_s d} G_r^{\uparrow\downarrow}. \quad (6.33)$$

A thinner ferromagnetic layer should lead to a higher $\Delta\alpha$.

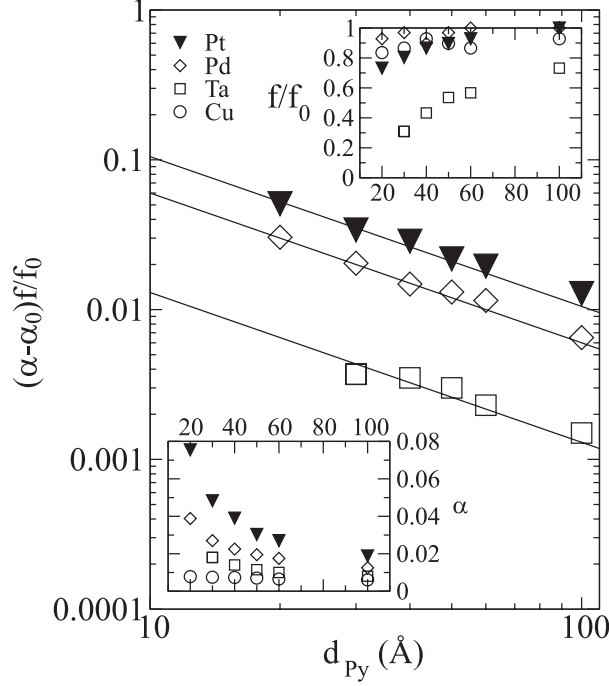


Figure 6.6: Damping parameter for the Pt/Py/Pt, Pd/Py/Pd, Ta/Py/Ta and Cu/Py/Cu trilayers, in which the thickness of the Py layer is varied from 2nm to 10nm, and the thickness of the Pd, Pt, Ta and Cu layer is 5nm[77].

FMR experiments carried out by Mizukami et al. revealed increased damping of trilayers with thin permalloy and different normal metals layers, such as platinum, palladium, titanium and copper[21]. Enhancement of the damping parameter was inversely proportional to the thickness of the ferromagnetic layer. Tserkovnyak et al.[77] estimate the change of the damping parameter due to the emission of spin currents as follows: assuming $g_r^{\uparrow\downarrow}$ is the conductance of the isotropic normal metal layer,

$$\alpha(d) \approx \kappa \frac{1.1}{d} \frac{f_0}{f(d)}.$$

f_0 and $f(d)$ are the atomic magnetization of the permalloy bulk and of the permalloy films with thickness d , expressed in \AA . κ is an adjustable parameter representing the number of scattering channels in units of one channel per interface atom, $\kappa \propto 1$. Experimental data of Mizukami fits well with the suggested model shown in Fig. 6.6. Experimental data is presented for the trilayers Pd/Py/Pd, Pt/Py/Pt, Ta/Py/Ta and Cu/Py/Cu. The thickness of the normal metal layer is 5nm for each sample, while permalloy varies from

2nm to 10nm. Fitting determines κ to be 1.0, 0.6 and 0.1 for Pt, Pd and Ta, respectively. The spin pumping effect agrees with the increased spin-flip relaxation rate for metals with higher atomic numbers. For a trilayer with Cu, the damping parameter is independent of permalloy layer thickness. Due to large spin-flip relaxation time for a light material such as Cu, 5nm is not enough to prevent spin accumulation at the interface with Py, so no significant increase of damping is observed.

The non-local damping theory, based on spin-dependent scattering at the N/F interface, also predicts change in gyromagnetic ratio γ_0 from spin current emission. In an ideal spin sink the change of gyromagnetic ratio is:

$$\frac{\gamma_0}{\gamma} = 1 + \frac{\hbar\gamma_0}{4\pi M_s d} G_i^{\uparrow\downarrow} . \quad (6.34)$$

The imaginary part of the conductance parameter $G_i^{\uparrow\downarrow} \approx (0.01 - 0.06) \cdot 10^{15} \cdot \Omega^{-1} \text{m}^{-2}$ is significantly smaller than the real part $G_r^{\uparrow\downarrow}$ and makes up only 2–8% of the real part $G_r^{\uparrow\downarrow}$ for a clean and smooth F/N interface[86]. The interface disorder enhances the mixing conductance mainly through the increase of $G_i^{\uparrow\downarrow}$ by a factor of 3. A change in precession frequency from spin current emission is not yet observed.

When the gyromagnetic ratio change cannot be neglected, the enhancement of the damping parameter $\Delta\alpha$ is described with the following expression for an ideal spin sink:

$$\alpha \frac{\gamma_0}{\gamma} = \alpha_0 + \Delta\alpha = \alpha_0 + \frac{\gamma_0 \hbar}{4\pi M_s d} G_r^{\uparrow\downarrow} . \quad (6.35)$$

6.3 Experimental approach

The all-optical pump-probe experiments give unique insight into the timescales of the magnetization relaxation processes. The characteristic times for the energy dissipation of the magnetization torque, and thus the damping itself are directly observed. This is a powerful tool to investigate damping processes in thin layers.

This work aims to investigate damping enhancement through spin current emission. A double layer F/N structure using nickel as the ferromagnetic layer is investigated. Due to the highest intrinsic damping of the transition metals, which could screen the non-local damping, only few experiments are performed on the nickel samples. The permalloy and iron films are mainly investigated by FMR or BLS.

The theory of the non-local damping, Eq. 6.32, predicts that the following properties determine the damping parameter enhancement:

1. the F/N interface conductance,
2. the thickness of the ferromagnetic layer,
3. the spin-flip relaxation rate and the thickness of the normal metal layer.

These properties cannot be considered independent from each other. The spin-flip relaxation rate and the majority of the conductance at the nickel interface are determined by the choice of the normal metal. Non-local damping originates from the scattering at the N/F interface. Thence, matching the crystalline structures and the growth qualities of both layers strongly influence previous parameters. Following chapter presents additional damping dependence on the roughness of the F/N interface and number of defects in the layers, by investigating double layers with different metals Pd, Al, Cr, Cu, Ag, Ti, Dy.

All experiments in this work are done on thin continuous films without any structuring. To enable relatively comparison of the spin sinks efficiency, the thickness of the normal metal layer is held constant at 5nm. It is estimated that this is thickness enough for heavier materials to become ideal spin sinks. For lighter materials, 5nm is insufficient to cause the same effect. The thickness of the ferromagnetic layer should be small enough to avoid energy dissipation in the ferromagnet itself. For a thicker ferromagnet, the non-local contribution to the damping hides behind the intrinsic damping constant, even for the ideal spin sink. The main objective of this work is to systematically investigate the non-local damping enhancement by varying ferromagnet thickness from 50nm to 2nm.

To make systematic and comparative measurements, the experiments are carried out as follows: The samples are measured in longitudinal configuration, keeping the orientation of the external field constant. The pump fluence is kept constant for different samples. Special attention is paid to compare the damping for the exactly same precession mode in samples with different ferromagnetic layer thicknesses.

The following sections details the magnetization relaxation processes in dependence on ferromagnetic layer thickness. An excitation mechanism in an all-optical pump-probe approach is the energy transfer from the pump beam to the electron system, which disturbs the magnetic order of the sample. For samples thinner than the optical penetration depth, a significant difference in the deposited energy is observed depending on sample thickness. The same pump fluence disturbs more the magnetic order in the thinner samples. The following presents the change of the demagnetization rate in dependence on the sample thickness. Thereafter, the magnetization relaxation for samples with different thickness is compared.

6.3.1 Variation of the demagnetization rate

The energy of the pump pulse is distributed within the ferromagnet according to the thermal profile defined by the optical penetration depth, λ_{opt} . The rate of the sample demagnetization induced by the pump pulse depends on the ferromagnetic sample thickness. Comparison of the hysteresis loops made with and without pump beam, at the maximum of the demagnetization peak, allows estimating the demagnetization rate in our experiments. Fig. 6.7 shows the hysteresis loops for Si(100)/5nmCr/xnmNi/2nmCu samples with varied nickel

layer thicknesses. The measurements are normalized so that the magnetization of the non-perturbed system is equal to one. The coercive field H_c increases by

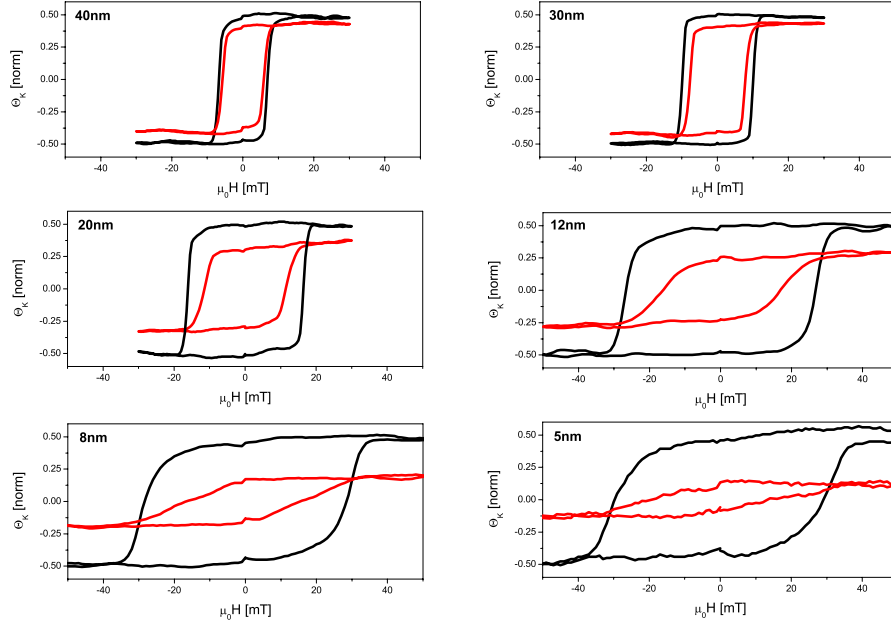


Figure 6.7: Hysteresis loops without (black line) and with (red line) pump pulse for Si(100)/5nmCr/xNi/2nmCu samples, at the maximum of the demagnetization peak. Pump fluence $F_{pump} = 50\text{mJ}/\text{cm}^2$, external field \mathbf{H} is oriented 35° out-of-plane.

reducing the nickel layer thickness. $\mu_0 H_c < 10\text{mT}$ for a 30nm thin nickel sample and $\mu_0 H_c = 40\text{mT}$ for a 5nm thin sample. This increase mainly originates from the growth induced defects in the nickel layer, which are significantly reduced in thicker samples. By applying the pump pulse, both saturation magnetization and the coercive field change significantly. Fig. 6.8 plots the demagnetization rate, extracted from the hysteresis measurements, versus the thickness of the nickel layer. The pump fluence of $F_{pump} = 50\text{mJ}/\text{cm}^2$ causes demagnetization of 20% for nickel samples thicker than 30nm. Reducing the thickness of the ferromagnetic nickel layer increases the demagnetization rate to 80% in a 5nm nickel sample. The higher demagnetization rate for thinner samples is expected from the corresponding increase in electron and spin temperature. Thermally induced decrease of anisotropy significantly reduces the coercive field under the pump pulse for measured samples.

The laser induced demagnetization of the ferromagnetic sample is a rather complicated process which cannot be characterized with one parameter such as the demagnetization rate. Therefore, measurements carried out in this work are made under identical excitation conditions i.e. external magnetic field and pump fluence. The magnetic relaxation for the various samples is then analyzed to compare dynamic magnetic variables of special interest.

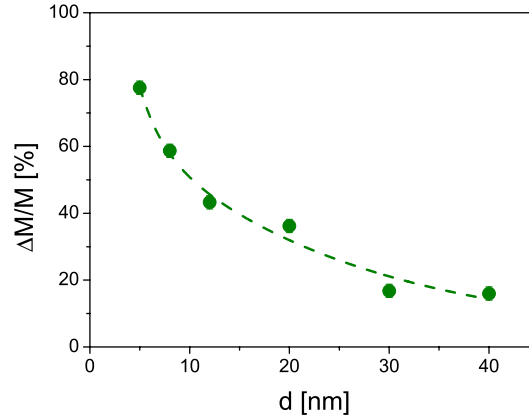


Figure 6.8: Demagnetization rate for Si(100)/5nmCr/xnmNi/2nmCu samples plotted versus thickness of the nickel layer. The line is a guide for the eyes.

6.3.2 Different magnetization relaxation channels

Fig. 6.9 shows the TRMOKE spectra of a Si(100)/1-60nmNi/5nmDy/2nmAl wedge sample for different nickel layer thicknesses. The pump fluence is held constant at $50\text{mJ}/\text{cm}^2$ with constant external field $\mu_0 H = -150\text{mT}$ oriented $\varphi(\mathbf{H}) = 30^\circ$ out-of-plane. The Kerr signal changes significantly depending on ferromagnetic layer thickness, so the analyzer angle is optimized for 10nm nickel layer and held constant for all other measurements. To eliminate the reflectivity contribution, measurements are taken at $\mu_0 H = -150\text{mT}$ and $\mu_0 H = 150\text{mT}$ and the asymmetric magnetic signal is extracted.

The magnetization relaxation comprises the coherent precession and incoherent magnon background. Depending on the thickness of the ferromagnetic layer, one of those two channels dominates the TRMOKE spectra. For ferromagnetic layers thinner than 6nm, the short wave magnons that incoherently contribute to the spectra are the main relaxation mechanism. The exponential character of the incoherent background indicates the highly perturbed magnetization state. By increasing the thickness of the nickel layer, the exponential character of the incoherent magnon background disappears, similarly its behavior to experiments with a varying pump fluence on the 50nm nickel sample. However, the emission of short wave magnons is still the dominant relaxation process. The maximum demagnetization peak occurs in the 7nm thin nickel sample. The largest incoherent magnon background is in the 13nm nickel sample. Further increasing nickel layer thickness reduces both the incoherent magnon background and the precession amplitude. As discussed in the previous chapter, the Kittel $k = 0$ mode dominates the precession of magnetization for samples thinner than the optical penetration depth λ_{opt} . The perpendicular standing spin-wave mode contributes the relaxation spectra for thicker samples. For samples thicker than 40nm there is no significant change in the relaxation pattern other than slightly different oscillations attributed to the standing spin wave.

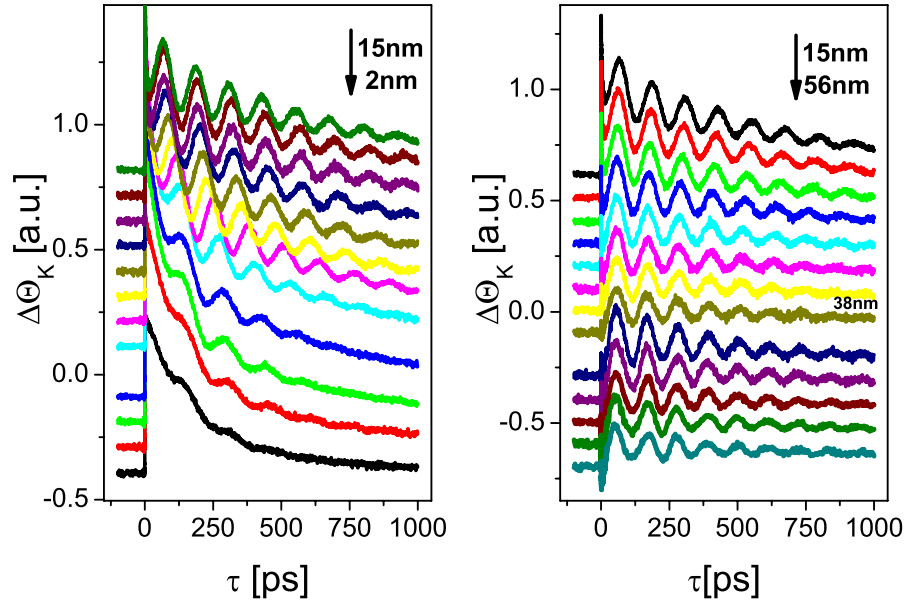


Figure 6.9: Time resolved spectra for different nickel layer thicknesses, on the Si(100)/1-60nmNi/5nmDy/2nmAl wedge sample. External field $\mu_0 H = -150\text{mT}$ is oriented 30° out-of-plane.

In all-optical pump-probe experiments, it is impossible to extract one magnetization relaxation process by which the perturbed ferromagnetic systems relax to equilibrium. Depending on the sample properties, the thermally induced anisotropy field pulse causes magnetization relaxation through various mechanisms. The incoherent magnon background can be extracted to observe clear oscillation pattern of the coherent magnetization rotation, from which the relevant magnetic parameters can be derived. Details of magnetization relaxation upon laser excitation have been discussed in the Chapter 5.

6.4 Extrinsic damping for F/N samples

As a preliminary experiment to the investigation of the thickness dependent non-local damping, the damping parameter for F/N double layers is investigated. Previously described theories modeled damping in a perfect crystal. The experimentally determined values are higher than theoretical predictions even for the pure samples, which implies that the calculations do not include all contributions to the damping. For the F/N structure with polycrystalline thin layers of different optical and thermal properties, experiment is the only way to estimate the relevant contributions to the damping.

The 10nm ferromagnetic layer of nickel is held constant, and 5nm normal metal layer is varied for the following materials: aluminum, copper, palladium, silver

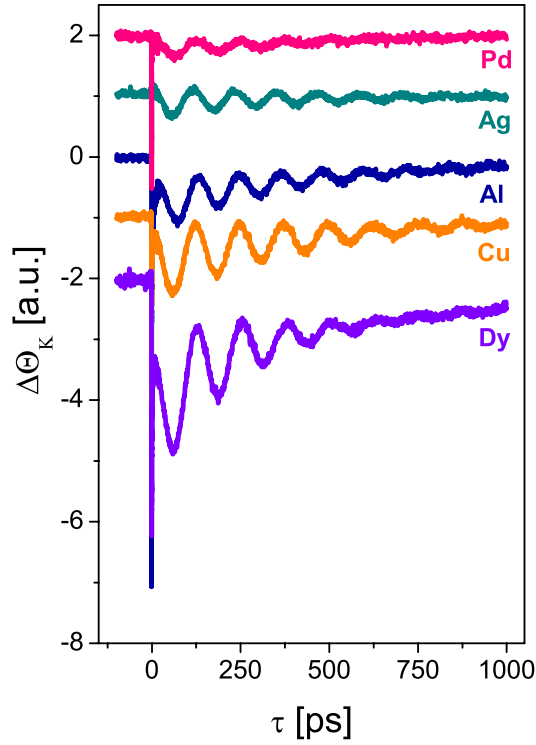


Figure 6.10: TR MOKE spectra for Si (100)/10nmNi/5nmX double layers, where X = Pd, Ag, Al, Cu, Dy. The measurements are made with $\mu_0 H = -150\text{mT}$, $\varphi(\mathbf{H}) = 35^\circ$ out-of-plane and $F_{\text{pump}} = 40\text{mJ}/\text{cm}^2$.

and dysprosium. The experimental conditions were the same for all measurements: The external magnetic field was $\mu_0 H = -150\text{mT}$, oriented $\varphi(\mathbf{H}) = 35^\circ$ out-of-plane with pump fluence of $F_{\text{pump}} = 40\text{mJ}/\text{cm}^2$.

The spectra presented in Fig. 6.10 show a clear difference in precession amplitude and incoherent magnetic background. This implies that the nickel layer perceives different strengths of the anisotropy pulse for each sample. The smallest precession amplitude occurs in the Si/Ni/Pd double layer and the largest in the Si/Ni/Dy. The large magnon backgrounds dysprosium and aluminum show that incoherent processes are an important channel for the magnetization relaxation for those samples.

Fig. 6.11 plots the precession frequencies of the double layers versus external magnetic field. The frequencies of the Kittel $k = 0$ mode for all samples are in the same range, of 6GHz to 8.5GHz for applied magnetic fields. The small equidistant changes are observed, from slightly different crystalline anisotropies from sample growth.

Fig. 6.12 shows the damping constant of the double layers for different values of external magnetic field. The damping parameter for the double layer ranges from 0.039(3) for the Si/Ni/Ag sample, up to 0.067(3) for the Si/Ni/Dy sample.

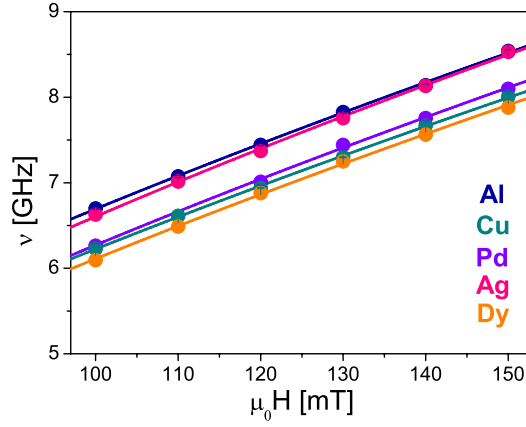


Figure 6.11: Frequency spectrum of basic mode for Si(100)/10nmNi/5nmX double layers, where X= Pd, Ag, Al, Cu, Dy. The lines are fits with the Kittel formal.

The Si/Ni/Al sample has $\alpha=0.041(2)$ while Si/Ni/Pd and Si/Ni/Cu samples have similar damping parameter 0.048(4). The highest damping is expected in double layers with dysprosium due to strong spin-orbit coupling for such a heavy material and additional damping by $4f$ electrons. The relatively small damping for the double layers with aluminum, copper and silver results from electronic configurations with only one s electron in the valence band. Surprisingly, the damping by silver is the smallest even though it is the heaviest metal of the three with a completely filled $4d$ orbital. The damping by the palladium layer should be higher for such a strong spin sink.

The measured distribution of the damping parameters for double layers with

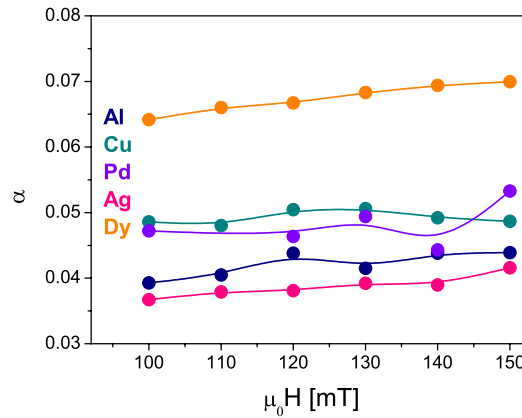


Figure 6.12: Damping parameter for Si(100)/10nmNi/5nmX double layers, where X=Pd, Ag, Al, Cu, Dy.

Al, Cu, Pd, Ag and Dy results not only from different spin-relaxation rates, but also from interface roughness between the nickel and normal metal layer. A similar effect is observed in thin permalloy films[87, 88]. Therefore, it is classified as extrinsic damping, which is more suitable for these F/N samples even though it mainly originates from the additional scattering sources at the N/F interface. To observe non-local damping by emission of spin current, the thickness of the nickel layer should be reduced to less than 10nm.

6.4.1 Influence of roughness

This section investigates two samples with identical ferromagnetic and normal metal layers: Si(100)/10nmNi/5nmAl and Si(100)/5nmAl/10nmNi/2nmCu, with the deposition order of nickel and aluminum layer switched. The samples are examined using X-ray diffraction and both static and dynamic magnetic measurements to determine the influence of the different growth conditions and interface roughness on the relevant magnetic parameters such as ν and α . The

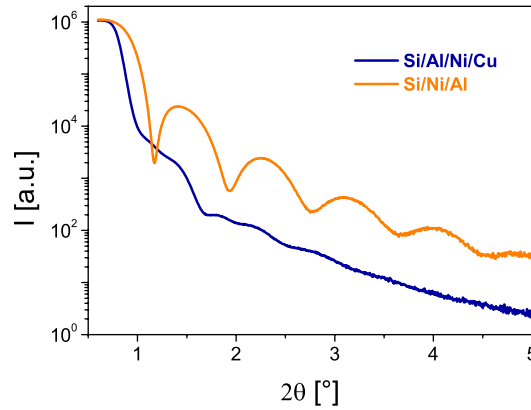


Figure 6.13: Low angle XRD measurements for Si(100)/5nmAl/10nmNi/2nmCu and Si(100)/10nmNi/5nmAl samples.

growth and interface qualities depend on matching materials crystalline properties. Both aluminum and nickel grow as face centered cubic crystals with lattice constants of 4.05\AA and 3.52\AA , respectively. The lattice mismatch is 13% percent for nickel grown on aluminum and -15% for aluminum grown on nickel. The samples are characterized by low angle X-ray diffraction measurements. Fig. 6.13 plots the scattered X-ray intensity versus incident angle θ . The roughness of the Si/Ni/Al sample is estimated to be $3\text{-}4\text{\AA}$. The thickness oscillations for Si/Al/Ni/Cu sample are insufficient to determine the interface roughness. Nevertheless, X-ray intensity decay at higher scattering angles mirrors the increased roughness at the interface. One can conclude albeit only qualitatively, that the sample with nickel grown on aluminum has a much rougher interface and therefore more growth defects than the sample in which the nickel is grown directly on to the silicon substrate.

Fig. 6.14 shows the hysteresis measurements of both samples. The coercive field strength is extracted for $\mu_0 H_c = 4\text{mT}$ in Si/Al/Ni/Cu and $\mu_0 H_c = 8\text{mT}$ in Si/Ni/Al. The higher coercive field results from increased interface roughness in the last sample, already implicated by the low angle X-ray measurements. Interface roughness between nickel and aluminum layers causes an inhomogeneous surface anisotropy field, which can locally rearrange the magnetic moments at the interface and within the nickel layer. Thus a higher external field must be applied to achieve ferromagnetic alignment of nickel magnetic moments. The strength of the observed increase in the coercive field results from the pronounced interface effect in thin samples.

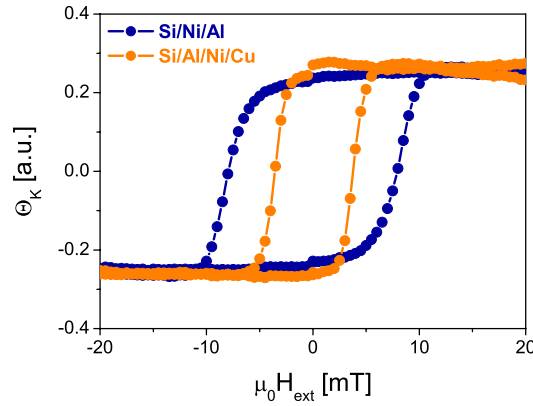


Figure 6.14: Hysteresis loops for Si(100)/5nmAl/10nmNi/2nmCu and Si(100)/10nmNi/5nmAl samples. The external magnetic field is oriented 30° out-of-plane.

Fig. 6.15 shows the Time Resolved MOKE spectra with identical experimental conditions for both samples: $\mu_0 H = -150\text{mT}$, $\varphi(\mathbf{H}) = 35^\circ$ out-of-plane and $F_{pump} = 40\text{mJ/cm}^2$. The magnetization precession for the 10nm nickel layer is totally different for both samples. The main precession mode frequency $\nu_0 = 6.7\text{GHz}$ for the Si/Al/Ni/Cu sample is smaller than that of $\nu_0 = 8.6\text{GHz}$ for the Si/Ni/Al sample. The effective magnetic field, composed of the Zeeman, demagnetization and volume crystalline anisotropy term, governs the spins and determines the precession frequency. The variations in the volume anisotropy term from nickel layer growth defects for both samples cannot lead to such a large change in the precession frequencies. Therefore the frequency decrease in the Si/Ni/Al/Cu sample is attributed to the additional surface anisotropy field, which reduces the effective field with respect to the Si/Al/Ni/Cu sample. The temperature increase from the intensive laser pulse influences the surface anisotropy more than the volume anisotropy, which leads also to higher precession amplitude in the Si/Al/Ni/Cu sample, compared to the amplitude of the demagnetization peak.

The time resolved measurements show that the amplitude of the precessing magnetization for the same sample decays faster than it does in the Si/Ni/Al sam-

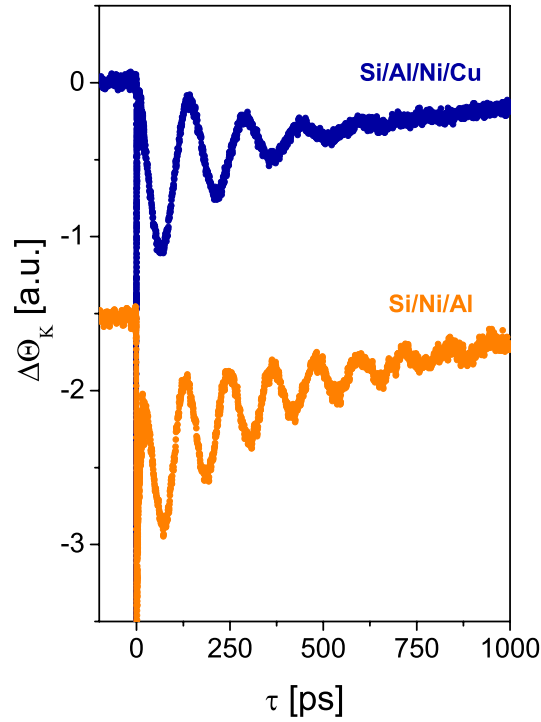


Figure 6.15: TR MOKE spectra for Si(100)/5nmAl/10nmNi/2nmCu and Si(100)/10nmNi/5nmAl samples at $\mu_0 H = -150\text{mT}$, $\varphi(H) = 35^\circ$ out-of-plane and $F_{\text{pump}} = 40\text{mJ/cm}^2$. Spectra are normalized to the same precession amplitude for the comparison.

ple. The characteristic exponential decay time of $\tau_\alpha = 185\text{ps}$ for the Si/Al/Ni/Cu and $\tau_\alpha = 300\text{ps}$ for Si/Ni/Al sample is observed. Eq.2.56 determines the corresponding damping parameters $\alpha = 0.110(2)$ and $\alpha = 0.044(2)$. It is noted that the energy dissipation described by the Gilbert damping parameter α refers to the energy dissipated in one precession period. An 26% increase in precession frequency alone would decrease the τ_α from 300ps to 238ps, hold α constant. The primary difference between damping parameters can then be attributed to both the precession frequency difference and characteristic decay time difference due to magnetic scattering at defects.

The main precession mode, which governs the magnetization relaxation upon the laser excitation, loses homogeneity due to the defects in the nickel layer caused by the roughness at the aluminum interface. It scatters into non-uniform modes, which carry away part of the magnetization torque energy and cause the additional damping. This mechanism is already proposed in [63], in which the authors attributed damping enhancement to two-magnon scattering mechanism for GaAs(001)/Fe/Pd/Au/Fe(001)/Au samples with a self-assembled network of misfit dislocations. The angular distribution of the damping parameter depending on the external magnetic field, as observed in the experiment, agrees with the two-magnon scattering theory of Mills[64]. The theory predicts that

there would be no non-uniform modes available for angles larger than $\pi/4$, which leads to the minimal damping parameter if the external field is perpendicular to the saturation magnetization. The presence of non-uniform modes is allowed in our experimental configuration, but an enhancement of the number of defects in the nickel layer, on which the homogeneous mode can be scattered, reduces the exponential decay time τ_α .

The roughness of the Ni/Al interface and resulting nickel layer defects for the Si/Al/Ni/Cu sample enhance the coercive field H_c by a factor of two, significantly reduce the precession frequency and enormously enhance the damping parameter to $\alpha=0.110$.

6.5 Non-local damping

This section presents in detail the experimental results of the non-local damping by spin currents emission on the ferromagnet/normal metal interface. The dynamic spin current excited by a precessing moment result from static spin polarization at the interface following a dynamic movement of a collective magnetic excitation. By introducing spin scattering within the non magnetic layer on a characteristic decay length, the layer acts as a spin-current sink. For each precession the pumping of a spin current results in a corresponding loss of magnetization and damps the precession of the magnetic moment. Double layers with nickel as the ferromagnet and various spin sinks are made for that purpose.

The effective emission of spin current through a ferromagnet/normal metal interface strongly depends on the thicknesses of both the ferromagnet and the normal metal layers. The thickness of the ferromagnetic layer has to be small enough to avoid the extrinsic damping already present in the ferromagnetic layer itself. On the other hand, the ferromagnetic layer has to have a magnetic order, so the smallest thickness is determined by the coherence spin length, which is, on the order of the lattice constant in a ferromagnet. This work investigates ferromagnetic layers with thicknesses from 1nm to 60nm. The thickness of the normal metal is determined by the spin flip scattering length and spin accumulation at the ferromagnet interface. An ideal spin sink, as presented in Chapter 6.2.4, is characterized by the total absorption of the spin current transmitted through the interface. To avoid spin accumulation at the FM/NM interface, the spins, pumped from the ferromagnetic layer have to diffuse relatively fast into the normal metal. The interface conductance and spin-flip time are the main parameters in determining the thickness of the normal metal layer. Within this work a constant spin sink thickness of 5nm is investigated. The rough estimation implies that the characteristic scattering length in heavy materials, such as Cr, Pd, Ag, Au, Dy, is $\approx 1-2\text{nm}$. Therefore, a 5nm thick normal metal layer is enough to observe spin dissipation. On the other hand, the characteristic scattering length in light materials, such as Al, Cu and Ti is $\approx 50\text{nm}$, so 5nm layers of those materials will not significantly increase the magnetization torque energy dissipation from ferromagnetic layer.

First, the measurements on individual samples are presented with palladium as

a spin sink. An increase in damping parameter α for samples thinner than 15nm is observed. At the same time, a systematic decrease in precession frequency is observed. To avoid the slight differences in the growth conditions and to increase the number of measurement points at different nickel layer thicknesses, the wedge samples are made with continuously varied nickel layer thickness. Measurements on the Ni/Pd wedge sample are presented below. A giant increase in damping parameter for nickel layers thinner than 10nm is observed. There is non-uniform frequency behavior for the main $k = 0$ precession mode: a slight increase for thicknesses larger than 10nm and a sharp drop for thicknesses smaller than 10nm. The measurements are repeated on Ni/Dy wedge samples with similar results. The additional damping is attributed to the spin current emission at the Ni/M interface, which increases the magnetic dissipation processes in an ideal spin sink such as the 5nm Pd and the 5nm Dy layers. Measurements on the individual Ni/Cr samples are presented at the end of section. In contrast to previous samples, additional damping from the Ni/Cr interface is not Gilbert like and shows strong frequency dependence. Nevertheless, a significant increase in the damping parameter is observed for thinner nickel layers due to the spin current emission from the nickel into the chromium layer.

6.5.1 Si/Pd/Ni/Cu individual samples

Experiments were performed on Si(100)/5nmPd/xNi/2nmCu layers, where the thickness of the nickel layer varies among $x=20\text{nm}$, 15nm , 10nm and 8nm . To access all details of demagnetization dynamics, measurements are taken in a large range of external fields, from 0mT to 150mT.

The TRMOKE measurements on the 10nm thin nickel layer are shown in Fig. 6.16. The external field is oriented $\varphi(H) = 35^\circ$ out-of-plane and the pump fluence is $F_{pump} = 40\text{mJ}/\text{cm}^2$. With no external field, there is no magnetic precession. Increasing the external field increases the frequency of the magnetization precession.

Fig. 6.17 plots the extracted precession frequency versus external field amplitude for all samples. The frequency dispersion versus external field is almost equivalent for samples with 20nm and 15nm thin nickel layers. For thinner samples the precession frequencies shift to lower values, leading to the smallest frequency for the thinnest sample with a 8nm nickel layer. The frequency spectrum over the external magnetic field enables measurement of the anisotropy constant, which is necessary to derive the damping parameter α from the directly observable exponential decay time τ_α , in Eq. 5.9.

Fig. 6.18 shows the damping parameter extracted from the TRMOKE spectra and its dependence on external magnetic field. The damping parameter is constant over a larger frequency range. This is a signature of the Gilbert like character of the damping constant. There are some small variations from the constant value in lower external fields due to the large precession period and induced higher damping parameter uncertainty. A clear increase of the damping

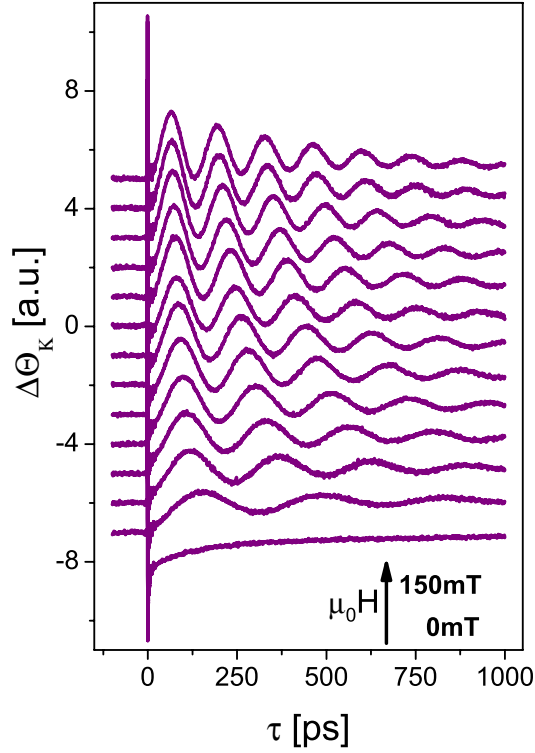


Figure 6.16: TR MOKE spectra for Si(100)/5nmPd/10nmNi/2nmCu sample at $0\text{mT} < \mu_0H < 150\text{mT}$, $\varphi(\mathbf{H}) = 35^\circ$ out-of-plane and $F_{\text{pump}} = 40\text{mJ}/\text{cm}^2$.

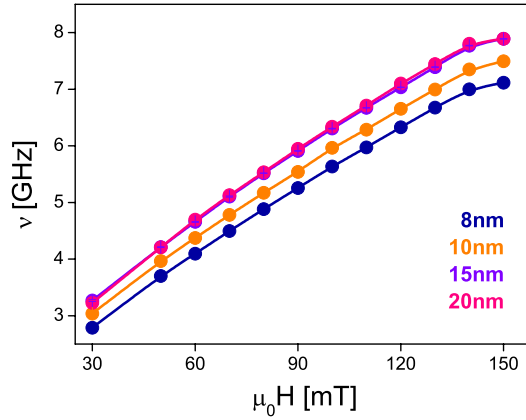


Figure 6.17: Frequency spectra versus external magnetic field for the Si(100)/5nmPd/xNi/2nmCu samples, with $x=20\text{nm}, 15\text{nm}, 10\text{nm}$ and 8nm at $0\text{mT} < \mu_0H < 150\text{mT}$, $\varphi(\mathbf{H}) = 35^\circ$ out-of-plane and $F_{\text{pump}} = 40\text{mJ}/\text{cm}^2$. The lines are fits with the Kittel formula.

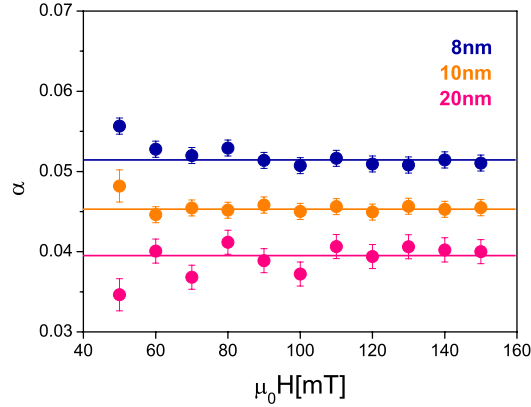


Figure 6.18: Gilbert damping parameter versus external magnetic field for Si(100)/5nmPd/xNi/2nmCu samples, with x=20nm,10nm and 8nm at $0\text{mT} < \mu_0 H < 150\text{mT}$, $\varphi(\mathbf{H}) = 35^\circ$ out-of-plane and $F_{\text{pump}} = 40\text{mJ/cm}^2$. The lines are guides for the eyes.

parameter for thinner films is observed. The damping constant takes values starting from 0.040(2) for the 20nm nickel layer, up to 0.052(1) for the 8nm nickel layer.

The thickness dependence of the damping parameter is presented in Fig. 6.19. The increase of the damping constant for samples with a thinner nickel layer is

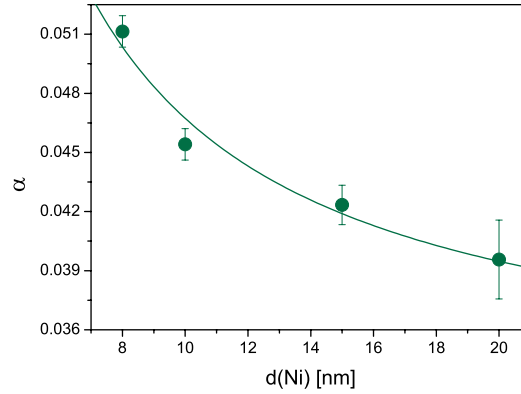


Figure 6.19: Damping parameter versus nickel layer thickness for the Si(100)/5nm Pd/x Ni/2nm Cu samples. The line is fit according to Eq. 6.36.

quantified with the fit function of Eq. 6.36, which is inversely proportional to the thickness d of the ferromagnetic layer

$$\alpha(d) = \alpha_0 + \frac{a}{d} . \quad (6.36)$$

α_0 represents the intrinsic damping and a is the spin pumping strength coefficient. The intrinsic damping $\alpha_0=0.032$ and the spin pumping strength coeffi-

cient $d=0.15\text{nm}$ are determined from the fit. The observed additional damping is attributed to the spin current emission on the Ni/Pd interface, which agrees with the measured non-local damping in Pd/Py/Pd trilayers measured with Ferromagnetic Resonance[21, 89].

6.5.2 Si/Pd/Ni/Al wedge sample

To increase the homogeneity of the samples and avoid differences caused by slightly different growth conditions for each individual sample, a wedge sample is made where the nickel layer thickness varied from 1nm to 60nm. The thickness of the palladium layer is held constant at 5nm and a 2nm aluminum capping layer is deposited to prevent oxidation.

The time resolved MOKE spectra are taken with extra precaution to make equivalent and systematic measurements on the entire wedge sample. The measurements are done in an external field of $\mu_0 H = 150\text{mT}$, $\varphi(H) = 30^\circ$ out-of-plane with a pump fluence of $F_{pump} = 50\text{mJ/cm}^2$. Fig. 6.20 shows the TR MOKE spectra on the wedge sample with nickel layer thicknesses of less than 10nm, from which the incoherent magnon background is extracted.

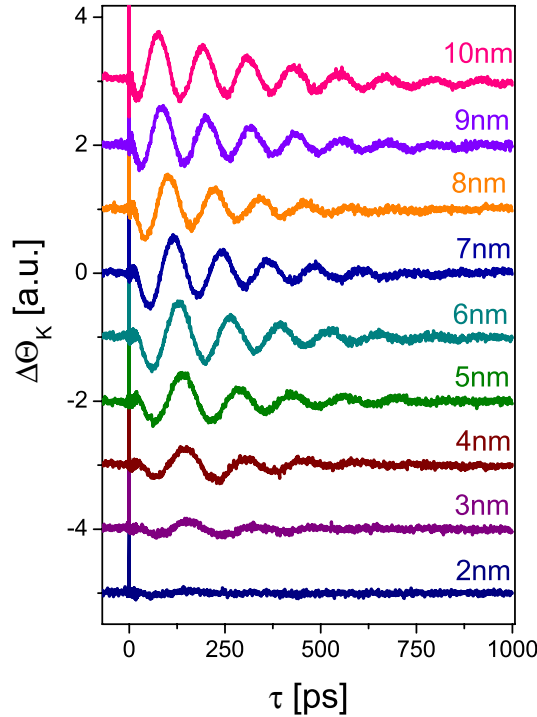


Figure 6.20: TR MOKE spectra for the Si(100)/5nmPd/xnmNi/2nmAl wedge sample at $\mu_0 H = -150\text{mT}$, $\varphi(H) = 30^\circ$ out-of-plane and $F_{pump} = 50\text{mJ/cm}^2$.

The precession amplitude and number of observed oscillations strongly depend on the nickel layer thickness. Starting with thicker samples, the oscillation

amplitude increases to a maximum at the 8nm nickel sample, then decays as thickness is reduced, and finally disappears totally in the 2nm nickel layer. A shift to lower frequencies in samples with thinner nickel films is also observed. The samples with thinner nickel layers have only one or two observable oscillation antinodes, which implies a higher damping parameter. The precession frequency ν and the exponential decay time τ_α are extracted from the TR MOKE measurements and plotted versus the thickness of the nickel layer in Fig. 6.21 and Fig. 6.22.

As observed for the time resolved spectra, the precession frequency is lower in samples with thinner nickel layers. Two regimes are observable in the frequency spectrum. Samples with nickel layers thicker than 10nm exhibit a relatively small frequency shift: 0.5GHz for the 40nm nickel layer. Samples with nickel layers thinner than 10nm show frequency drops of ≈ 5.5 GHz for the 3nm nickel layer. The frequency change for the thinner nickel layers can be also attributed to the spin current emission at the Ni/Pd interface.

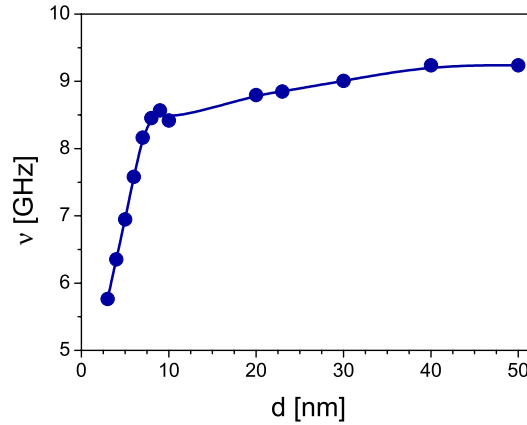


Figure 6.21: Precession frequency versus nickel layer thickness for the Si(100)/5nmPd/ x nmNi/2nmAl wedge sample at $\mu_0 H = -150$ mT, $\varphi(H) = 30^\circ$ out-of-plane and $F_{pump} = 50$ mJ/cm². The line is a guide for the eyes.

The exponential decay time τ_α decreases non-uniformly with reducing the nickel layer thickness from $\tau_\alpha = 330$ ps for the 10nm nickel layer down to $\tau_\alpha = 175$ ps for the 3nm nickel layer. At around 6nm nickel, the damping time slightly increases by $\approx 20\%$. This is shown below to be a characteristic feature of wedge samples.

The damping parameter is derived from τ_α by extracting the anisotropy constant from the frequency values. Fig. 6.23 plots the damping parameter versus the nickel layer thickness on a Si/Pd/Ni/Al wedge sample. The damping parameter is almost constant at ≈ 0.04 for samples with thicker nickel layers. When the nickel layer thickness less than 10nm, damping parameter enhancement is inversely proportional to the nickel layer thickness. α takes values up to 0.142 for the 3nm nickel layer. This additional damping is attributed to the spin

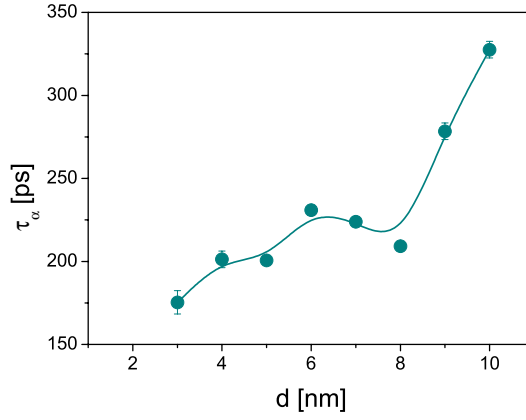


Figure 6.22: Exponential decay time versus nickel layer thickness for the Si(100)/5nmPd/xnmNi/2nmAl wedge sample at $\mu_0 H = -150\text{mT}$, $\varphi(H) = 30^\circ$ out-of-plane and $F_{pump} = 50\text{mJ}/\text{cm}^2$. The line is a guide for the eyes.

current emission at the Ni/Pd interface.

To characterize the spin pumping strength, the theory of non-local damping by emission of spin current by Tserkovnyak and Braatas can be applied. Eq. 6.36 gives the appropriate function to describe the increase of the damping and fit agrees well with the experimental data shown in Fig. 6.23. The values of the intrinsic damping $\alpha_0 = 0.024(3)$ and spin pumping coefficient $a = 0.33(3)$ are determined from the fit. The intrinsic damping constant α_0 is comparable with literature values for nickel. Spin pumping coefficient can also be used as the conductance parameter, and Eq. 6.34 results in a corresponding value

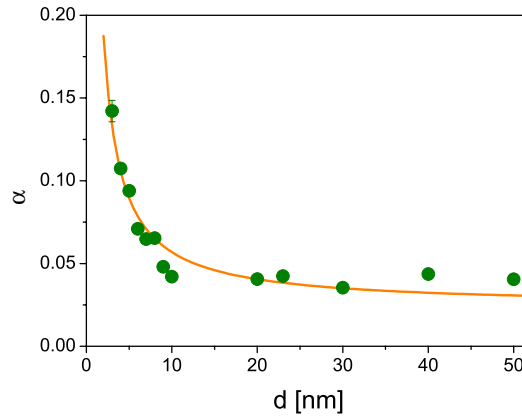


Figure 6.23: Damping parameter versus nickel layer thickness for the Si(100)/5nmPd/xnmNi/2nmAl wedge sample at $\mu_0 H = -150\text{mT}$, $\varphi(H) = 30^\circ$ out-of-plane and $F_{pump} = 50\text{mJ}/\text{cm}^2$. The line is fit according to Eq. 6.36.

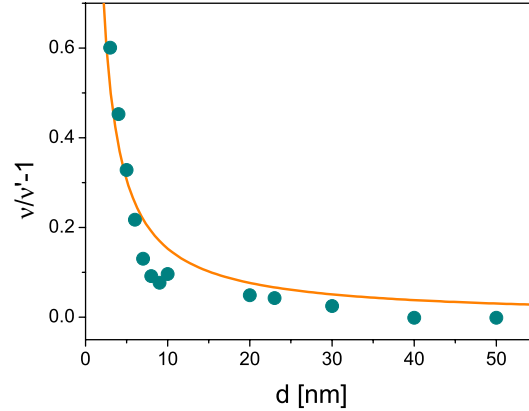


Figure 6.24: Normalized frequency change versus nickel layer thickness for the Si(100)/5nmPd/xnmNi/2nmAl wedge sample at $\mu_0 H = -150\text{mT}$, $\varphi(H) = 30^\circ$ out-of-plane and $F_{pump} = 50\text{mJ/cm}^2$. The line is a fit according to Eq. 6.34.

of $G_r^{\uparrow\downarrow} = 4.5 \cdot 10^{15} \Omega^{-1} \text{m}^{-2}$. This experimentally determined real part of the interface mixing conductance is an order of magnitude greater than theoretical predictions for the Cu/Co and Cr/Fe clean interface and alloy. No calculations are made for the nickel that consider realistic interface roughnesses. These would be more appropriate to compare to the $G_r^{\uparrow\downarrow}$ determined in our experiment.

The theory of non-local damping by the spin current emission predicts a change in the gyromagnetic ratio. The observed reduction of the precession frequency for a nickel layer, for which the corresponding damping parameter is enhanced, could result from spin current emission at the FM/NM interface. The experimental values fit well with Eq. 6.34, as shown in Fig. 6.24, with the imaginary part of the conductance tensor $G_i^{\uparrow\downarrow} = 2.1 \cdot 10^{16} \Omega^{-1} \text{m}^{-2}$. This value is three orders of magnitude greater than theoretical calculations. Underestimation of the mixing interface conductance, $G^{\uparrow\downarrow}$, for this particular sample and the expected strong increase of its imaginary part $G_i^{\uparrow\downarrow}$, could explain the difference between the measured and the calculated values.

The increase in damping parameter for samples with thinner nickel layers in double layers with palladium, by almost triple, results from spin-current damping. The 5nm palladium layer has proven a good spin sink, causing dephasing of the spin up and spin down electrons, originating from pumping through magnetization torque from the nickel layer. Reduction of the precession frequency from 9GHz to 5.5GHz is observed in the same thickness range.

6.5.3 Si/Ni/Dy/Al wedge sample

To further investigate the damping by spin currents, the normal metal is switched and dysprosium is used as the spin sink. The wedge sample Si(100)/Ni/5nmDy/-

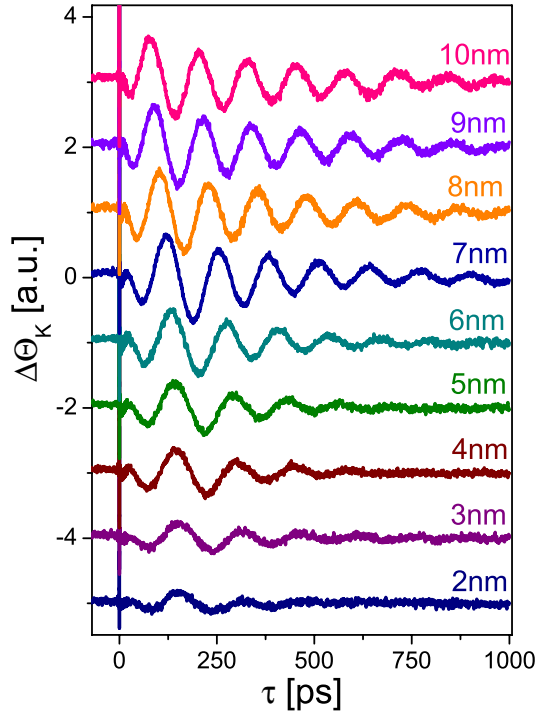


Figure 6.25: TR MOKE spectra for the Si(100)/5nmDy/xnmNi/2nmAl wedge sample at $\mu_0 H = -150\text{mT}$, $\varphi(H) = 30^\circ$ out-of-plane and $F_{pump} = 50\text{mJ}/\text{cm}^2$.

2nmAl is made with a varied nickel layer thickness from 1nm to 60nm. The time resolved MOKE spectra are taken with extra precaution to make equivalent and systematic measurements on the entire wedge sample. The measurements are done in an external field of $\mu_0 H = 150\text{mT}$, $\varphi(H) = 30^\circ$ out-of-plane, under a pump fluence of $F_{pump} = 50\text{mJ}/\text{cm}^2$. Fig. 6.25 shows the TR MOKE spectra on the wedge sample with nickel layer thicknesses less than 10nm, from which the incoherent magnon background is extracted. The dependence of the oscillation amplitudes on the nickel layer thickness as well as the reduced number of visible oscillations for thinner films is observable. The precession frequency and damping parameter are extracted from the time resolved spectra and plotted versus the thickness of the nickel layer on the Si/Ni/Dy/Al wedge sample in Fig. 6.26 and Fig. 6.28.

The complicated frequency distribution can be classified into three regions of the nickel layer thickness: the saturation plateau at $\approx 8\text{GHz}$ for thicknesses around 10nm, the slow rise of 1GHz over 40nm thickness for thicker samples, and a sharp drop of 2GHz over 6nm thickness for thinner samples. The change in precession frequency for thicker layers results from the mode conversion between the main $k = 0$ mode and the standing spin-wave modes. The giant drop in frequency for thinner layers is caused by the change in the gyromagnetic ratio from spin current emission. Independently of the change of the precession

frequency, only the main mode and the corresponding damping parameters are considered within this chapter.

Fig. 6.27 plots the exponential decay time τ_α , extracted from fitting the time resolved spectra in Fig. 6.25, versus the nickel layer thickness. τ_α decreases non-uniformly by reducing the thickness of the nickel layer, taking values from $\tau_\alpha = 440\text{ps}$ for a 13nm nickel layer down to $\tau_\alpha = 136\text{ps}$ for a 2nm nickel layer. For the approximately 3nm, nickel layer the damping time slightly increases by $\approx 10\%$, similar to the wedge sample with palladium.

Fig. 6.28 plots the damping parameter of the main $k = 0$ mode versus the nickel layer thickness on the Si/Ni/Dy/Al wedge sample. The damping parameter is almost constant at 0.033(2) for nickel layer thicknesses between 10nm and 20nm. By reducing the thickness of the nickel layer to under 10nm a giant increase of the damping parameter is observed, up to $\alpha = 0.18$ for 2nm. This additional damping for thin nickel films is from spin-current damping. There is a slight homogeneous increase of 20% of the damping parameter is observed for thicker nickel layers, with the maximum value at a thickness of 35nm.

To characterize the spin pumping strength, the damping parameter is fitted with Eq. 6.36 and the fit is also presented in Fig. 6.28. The proposed model from Tserkovnyak and Brataas agrees for thicknesses smaller than 20nm. The intrinsic damping of $\alpha_0 = 0.012(5)$ and a spin pumping coefficient $a = 0.32(3)$ are determined from the fit. The corresponding real part of the mixing interface conductance is $G_r^{\uparrow\downarrow} = 4.5 \cdot 10^{15} \Omega^{-1} \text{m}^{-2}$, similar to the wedge sample with palladium. The Tserkovnyak and Brataas model describes the damping parameter enhancement due to the spin current emission, which is the dominating process for thin ferromagnetic layers but insufficient to completely describe the thickness dependence of the damping parameter. Therefore, Eq. 6.36 agrees well with the experimental results only for nickel layer thicknesses smaller than

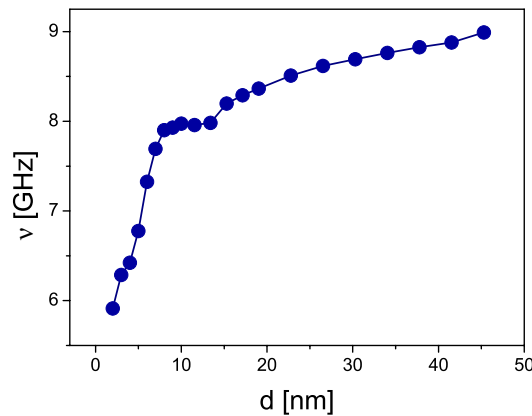


Figure 6.26: Precession frequency versus nickel layer thickness for the Si(100)/5nmDy/xnmNi/2nmAl wedge sample at $\mu_0 H = -150\text{mT}$, $\varphi(H) = 30^\circ$ out-of-plane and $F_{pump} = 50\text{mJ/cm}^2$. The line is a guide for the eyes.

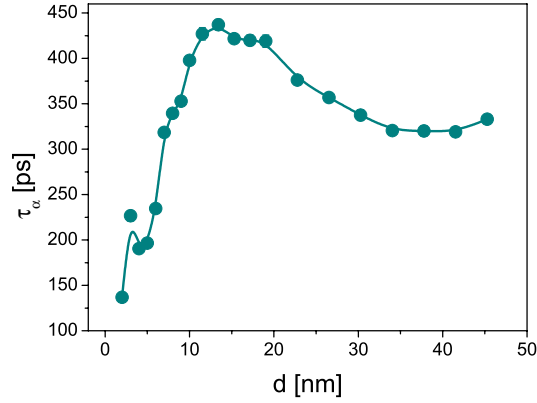


Figure 6.27: Exponential decay time τ_α versus nickel layer thickness for the Si(100)/5nmDy/xnmNi/2nmAl wedge sample at $\mu_0 H = -150\text{mT}$, $\varphi(H) = 30^\circ$ out-of-plane and $F_{pump} = 50\text{mJ/cm}^2$. The line is a guide for the eyes.

20nm.

The additional increase of the damping parameter for thicknesses larger than 20nm has a different origin than the spin pumping. Both the Kittel $k = 0$ and standing spin-wave mode are present at these thicknesses. The increase in damping parameter α for the Kittel mode indicates that there are the additional dissipation processes, in which the magnetic energy is transferred from the Kittel to the standing spin-wave mode. The effectivity of the mode conversion depends on the wavevector $k = \pi/d$ of the standing spin wave, which explains the non-monotonic behavior of the damping parameter.

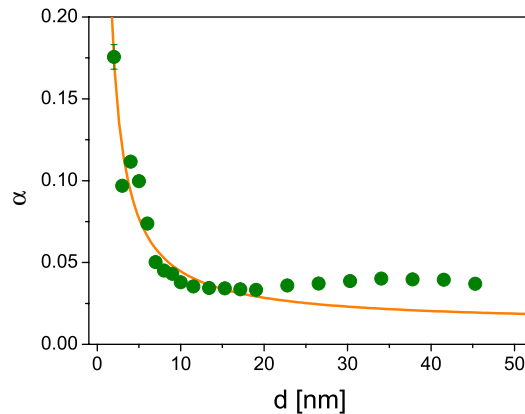


Figure 6.28: Damping parameter versus nickel layer thickness for the Si(100)/5nmDy/xnmNi/2nmAl wedge sample at $\mu_0 H = -150\text{mT}$, $\varphi(H) = 30^\circ$ out-of-plane and $F_{pump} = 50\text{mJ/cm}^2$. The line is a fit according to Eq. 6.36.

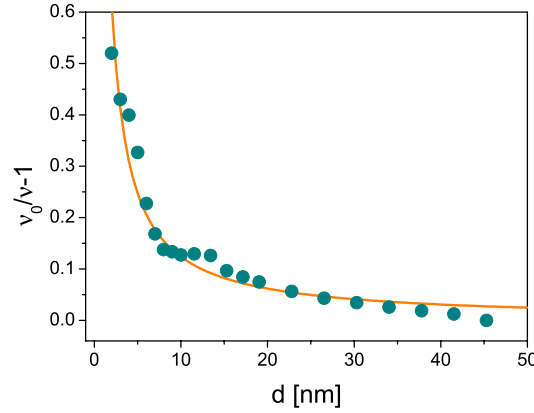


Figure 6.29: Normalized frequency change versus nickel layer thickness for the Si(100)/5nmDy/xnmNi/2nmAl wedge sample at $\mu_0 H = -150\text{mT}$, $\varphi(H) = 30^\circ$ out-of-plane and $F_{pump} = 50\text{mJ}/\text{cm}^2$. The line is a fit according to Eq. 6.34.

The non-homogeneous decay in the frequency spectrum can also be explained by applying the theory of non-local damping by the spin current emission. The experimental values fit well with Eq. 6.34, as shown in Fig. 6.29, with the imaginary part of the conductance tensor $G_i^{\uparrow\downarrow} = 1.7 \cdot 10^{16} \Omega^{-1} \text{m}^{-2}$. This value is slightly smaller than that for the Ni/Pd wedge sample.

A damping parameter enhancement from the spin current emission is observed for nickel/dysprosium layers with 5nm Dy and nickel layer thicknesses smaller than 10nm. When the thickness of the nickel layer approaches the λ_{opt} , the increase in damping parameter of the Kittel $k = 0$ mode is observed, resulting from the mode conversion to the standing spin wave. The reduction of the Kittel mode frequency from 9GHz to 6GHz is observed for thicknesses of less than 50nm.

6.5.4 Si/Cr/Ni/Cu individual samples

This section investigates chromium as a spin sink. For this purpose, samples are made with a varied nickel layer thicknesses from 2nm to 100nm, with chromium layer thickness held constant at 5nm, Si(100)/5nmCr/xnmNi/2nmCu. To access all details of the demagnetization dynamics, the measurements are taken in a variety of external fields, from 0mT up to 150mT. Fig. 6.30 shows the time resolved MOKE spectra of a 15nm thin nickel layer sample, with the external magnetic field oriented $\varphi(\mathbf{H}) = 35^\circ$ out-of-plane and pump fluence $F_{pump} = 50\text{mJ}/\text{cm}^2$.

The measurements show that the chromium layer makes the magnetization of the nickel layer quite inert, so higher external magnetic fields are required to trigger the coherent magnetization precession. Due to the small oscillation amplitude, the uncertainty of the experimentally determined magnetic parameters

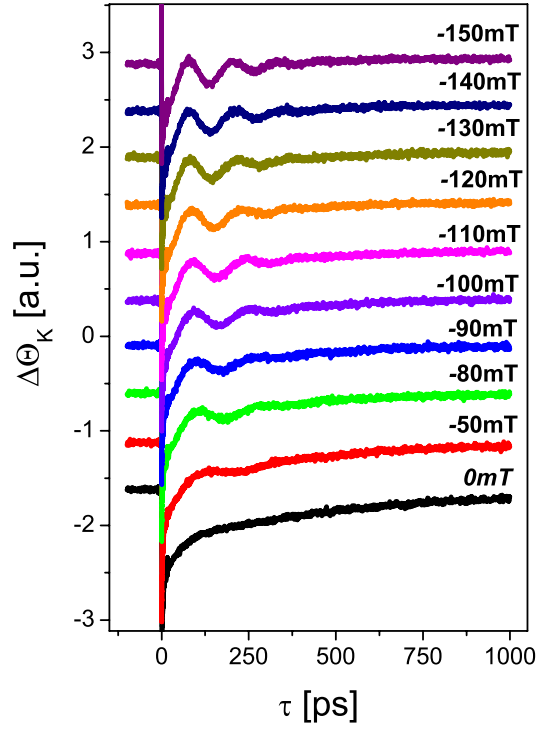


Figure 6.30: TR MOKE spectra for the Si(100)/5nmCr/15nmNi/2nmCu sample at $0\text{mT} < \mu_0 H < 150\text{mT}$, $\varphi(\mathbf{H}) = 35^\circ$ out-of-plane and $F_{\text{pump}} = 50\text{mJ}/\text{cm}^2$.

is much higher than in the previous samples.

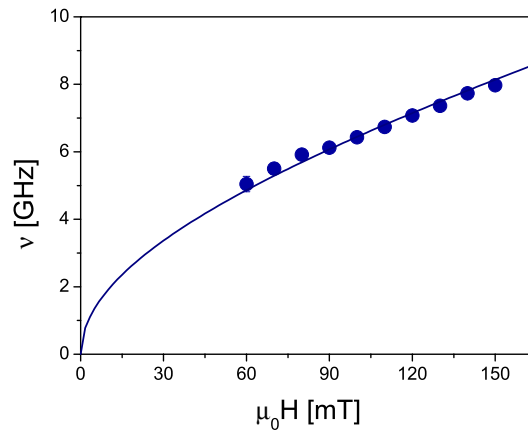


Figure 6.31: Frequency spectrum for the Si(100)/5nmCr/15nmNi/2nmCu sample at $0\text{mT} < \mu_0 H < 150\text{mT}$, $\varphi(\mathbf{H}) = 35^\circ$ out-of-plane and $F_{\text{pump}} = 50\text{mJ}/\text{cm}^2$. The line represents the fit with the Kittel formula Eq.2.40.

Fig. 6.31 shows the frequency spectrum of the Si(100)/5nmCr/15nmNi/2nmCu sample. The frequencies fit well with the Kittel formula with an out-of-plane anisotropy constant of $K_z = 2.49(5) \cdot 10^5 \text{ J/m}^3$. The damping parameter is then derived from the exponential decay time and plotted versus external magnetic field in Fig. 6.32.

The strong frequency dependence of the damping parameter is observed, in contrast with the previous samples, in which the damping had a Gilbert like character. For a 15nm nickel layer, α goes from 0.08 in higher magnetic fields to 0.26 in lower fields. A small stagnation in the damping parameter occurs

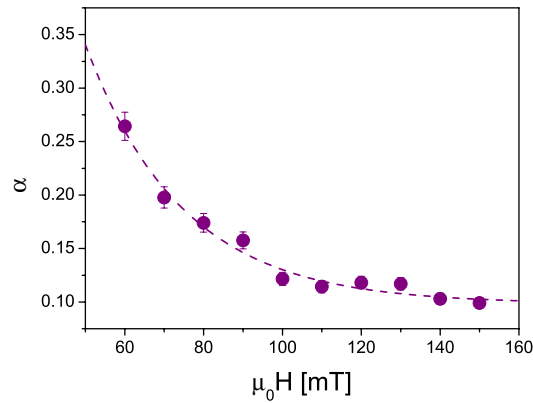


Figure 6.32: Damping parameter for the Si(100)/5nmCr/15nmNi/2nmCu sample at $0 \text{ mT} < \mu_0 H < 150 \text{ mT}$, $\varphi(\mathbf{H}) = 35^\circ$ out-of-plane and $F_{pump} = 50 \text{ mJ/cm}^2$. The line is a guide for the eyes.

for fields $\mu_0 H > 100 \text{ mT}$, so those values can be attributed to the intrinsic value of the damping parameter. The frequency dependence of α originates from the antiferromagnetic order of the chromium itself and implies that dissipation processes are complicated at the Ni/Cr interface.

To observe the damping by spin currents, experiments were performed on Si(100)/5nmCr/xnmNi/2nmCu layers, in which nickel layer thickness varies to values of $x=2 \text{ nm}$, 5 nm , 8 nm , 10 nm , 15 nm , 20 nm , 30 nm and 40 nm . Fig. 6.33 shows the TR MOKE spectra of the Si/Cr/Ni/Cu samples with nickel layer thicknesses from 2 nm to 40 nm in an external field of $\mu_0 H = -150 \text{ mT}$, $\varphi(\mathbf{H}) = 35^\circ$ out-of-plane, with a pump fluence $F_{pump} = 50 \text{ mJ/cm}^2$. These spectra are quite different. For samples with a nickel layer up to 30 nm , only one oscillation is observed, which is attributed to the Kittel $k = 0$ mode. With increasing the nickel layer thickness a second oscillation also contributes to the spectra. This oscillation results from the standing spin wave observed for samples thicker than the optical penetration depth λ_{opt} of the laser beam.

The time resolved spectra already imply that damping parameter depends on the thickness of the nickel layer. Only two antinodes are observed for samples with a thinner nickel layer, which signifies that those samples are more strongly damped. In contrast, the thicker samples, which are weaker damped, have clear

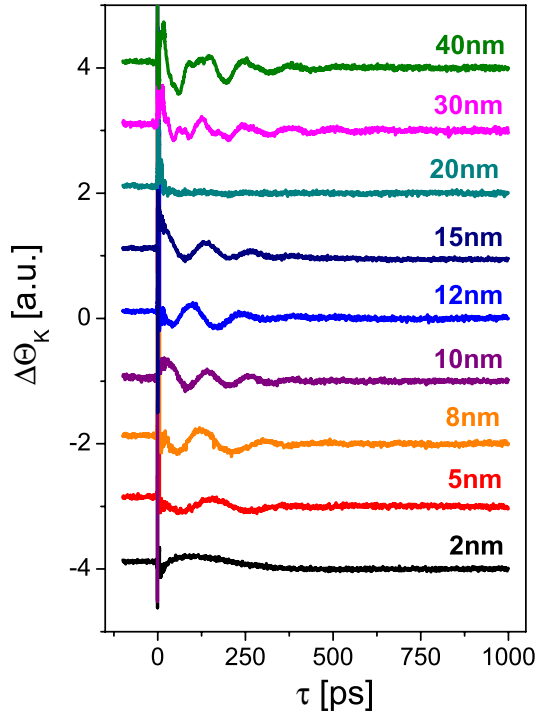


Figure 6.33: TR MOKE spectra for the Si(100)/5nmCr/xNi/2nmCu samples at $\mu_0 H = -150\text{mT}$, $\varphi(\mathbf{H}) = 35^\circ$ out-of-plane and $F_{\text{pump}} = 50\text{mJ}/\text{cm}^2$.

precession patterns up to the 5th oscillation antinode.

Fig. 6.34 shows the frequency dependence of the damping parameters for Si/Cr/-Ni/Cu samples with a nickel thickness of 12nm and 40nm. As a reference data set, the damping parameter of the Si(100)/5nmCr/50nmNi/3nmCu sample is plotted as well. A replacement of the copper layer with chromium already causes a significant increase in damping by more than a factor of three. The additional damping with the insertion of a Cr layer shows further enhancement through reduction of Ni layer thickness. For the Si/5nmCr/12nmNi/2nmCu sample, α takes values starting from 0.2 for high field and increases up to 0.6 for lower fields. Remarkably, this value corresponds to damping within only $\tau \approx 60\text{ps}$ to 110ps . The time constant of the damping approaches the period of the magnetic precession.

Though α depends strongly on the precession frequency, the damping parameters for different samples can be compared with values in higher external magnetic fields. Fig. 6.35 presents the damping parameter α , extracted from the time resolved measurements in $\mu_0 H = -150\text{mT}$ for samples with different nickel layer thickness. A homogeneous increase in the damping parameter, inversely proportional to the thickness of the nickel layer is observed. Fitting Eq. 6.36 determines the value of the intrinsic damping constant $\alpha_0 = 0.10(2)$ and the spin pumping coefficient $a = 0.67(5)$. The attributed real part of the interface

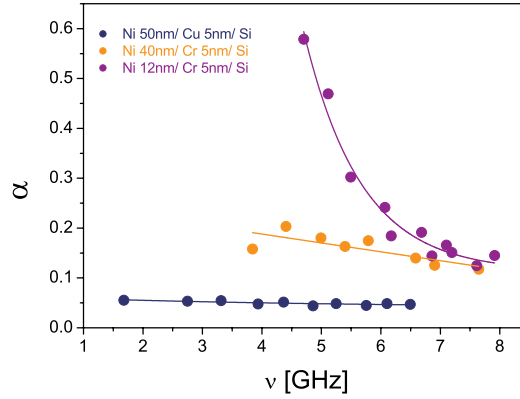


Figure 6.34: Damping parameter versus the precession frequency of the magnetization for Si(100)/5nmCr/xNi/2nmCu samples, where $x=40\text{nm}$ and $x=12\text{nm}$, and for a Si(100)/5nmCu/50nmNi/3nmCu sample. The lines are guides for the eyes.

conductance is then $G_r^{\uparrow\downarrow} = 9.4 \cdot 10^{15} \Omega^{-1} \text{m}^{-2}$.

The pronounced frequency dependence of the damping parameter implicates a complicated energy dissipation process at the Ni/Cr interface. This could be attributed to two-magnon scattering. A similar effect has been observed at the Fe/Cr interface[90]. The authors point out that two-magnon scattering, as a consequence of spatially inhomogeneous exchange bias due to the antiferromagnet-ferromagnet interface, induces a frequency dependence of α . In our case, however, the effect is much more pronounced and the damping is measured over a broader field range.

We conclude that the inserted Cr layer acts as a spin sink due to strong spin-

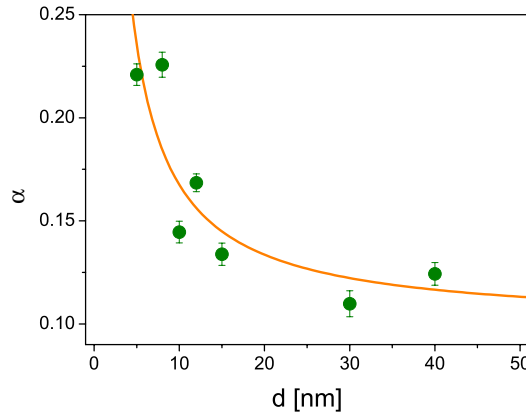


Figure 6.35: Damping parameter versus nickel layer thickness for the Si(100)/5nmCr/xNi/2nmCu samples at $\mu_0 H = -150\text{mT}$, $\varphi(\mathbf{H}) = 35^\circ$ out-of-plane and $F_{\text{pump}} = 50\text{mJ/cm}^2$. The line is a fit according to Eq. 6.36.

orbit scattering and complex magnetic order. It is also responsible for the observed additional damping, which shows strong frequency dependence.

6.6 Conclusion

The all-optical pump-probe experiments are a powerful tool to investigate the energy dissipation processes. The directly observable dissipation times are the main advantage of the time resolved measurements compared to techniques relying on the frequency range. The magnetization relaxation upon excitation by an intensive pump pulse is a complex process that includes of coherent and incoherent contributions. This chapter investigated the dissipation of the magnetization torque energy of the Kittel $k = 0$ mode in various ferromagnet/normal metal samples.

As preliminary work to estimate the effect of spin pumping, the damping parameter of the double layers with Pd, Cu, Al, Cr, Dy is compared. The smallest damping parameter is found for the Ni/Ag double layer, and the largest for the Ni/Dy sample. This agrees with the theory of non-local spin current by Tserkovnyak, in which the elements with full p and f orbitals are damped much more strongly than those with s electrons, as for Ag.

The non-local damping is then investigated for spin sinks of 5nm palladium, dysprosium and chromium. A giant enhancement of the damping parameter for nickel layers thinner than 10nm is observed. 2-3nm nickel samples show damping parameter up to three times higher than in the thicker layer. The damping parameter increases with inversely proportion to the thickness of the nickel layer. The intermixing conductance coefficients for the Ni/Pd, Ni/Dy and Ni/Cr interfaces are determined by fitting the experimental values. The conductance parameters for the double layers with Pd and Dy are similar to each other, but smaller than those for the double layer with Cr. In general, the measured values are one order of magnitude greater than theoretical predictions. It is rather complicated to compare the calculations based on the modeled interfaces and energy bands with the measurements on the real samples. It has been shown, that the increased interface roughness is sufficient to double the damping parameter. The additional damping due to spin-current emission is expected to have a rather small effect, but due to its tendency to occur at interfaces, there can be an additional energy dissipation that is not included into the model of damping by spin currents.

Additionally, with increase of the damping parameter for thinner nickel layers, the frequency of the Kittel $k = 0$ mode decreases in the same thickness range. The theory of non-local damping by spin currents also predicts a change of the gyromagnetic ratio proportional to the imaginary part of the mixing conductance coefficient. The theoretical predictions by the same authors imply that the imaginary part of the mixing interface conductance is much smaller than the real one. When the appropriate normalized experimentally determined precession frequencies are fitted to the model of non-local damping by spin currents, the determined mixing coefficient is three orders of magnitude greater

than the theoretically predicted one. This difference is partially attributed to underestimation of the mixing conductance, especially to the neglected influence of the interface roughness. There could be also other reasons for precession frequency decrease for thinner samples. For example, the increase of the magneto-crystalline anisotropy would cause a similar effect. Larger anisotropy leads to a higher precession frequency and coercive field. These relations are expected to be inverse to the layer thickness.

The damping parameter of nickel/chromium double layers is found not to be of Gilbert type, but rather strongly dependent on the precession frequency. This indicates the presence of two-magnon processes at the Ni/Cr interface. Nevertheless, the increase of the damping parameter for films with reduced nickel layer thickness unambiguously mirrors the spin pumping effect.

CHAPTER 7

Summary

The all-optical pump-probe technique is a powerful tool to investigate magnetization dynamics on sub ns timescales. In contrast to frequency oriented techniques, time resolved measurements allow direct observation of the basic time constants of magnetization dynamics with inherent time resolution using femtosecond laser pulses. The time resolved spectrum is characterized by a strong negative peak shortly after the pump pulse reaches the sample, which represents ultrafast demagnetization, followed by damped magnetic precession plus incoherent background on the ns scale. This work investigates thin transition metal ferromagnetic films on both long and short timescales upon laser excitation.

The demagnetization peak is found to be strongly dependent on the external magnetic field even though the Zeeman energy term is significantly smaller than the thermal energy from the pump pulse. The remagnetization of the sample is described by two relaxation times. One is in the range of 400-800fs and is attributed to the spin-phonon scattering in earlier work. The second relaxation takes place at a timescale of 5-8ps and is observed for highly perturbed systems, such as measurements for high pump fluencies. This ultraslow remagnetization is attributed to the energy transfer from spin waves with higher wave vectors to those with smaller k-vectors and Kittel $k = 0$ mode.

The magnetization dynamics on the 100ps scale are followed by coherent precession of the magnetization and the incoherent magnon background. The various spin-wave modes excited are ascribed to three regions of thickness of the nickel layer. The Kittel $k = 0$ mode, which describes the coherent homogenous precession within the entire ferromagnetic layer, is present for all sample thicknesses. If the sample is thicker than the optical penetration depth λ_{opt} , standing spin-wave modes up to the third order are also observed. Due to their origin in the

exchange interaction, those modes exist in both longitudinal and polar configurations. For samples significantly thicker than λ_{opt} , the dipole field dominated modes are also observed. The incoherent background is found to have a magnetic origin contributed from the incoherent short wavelength magnons.

The last chapter investigates the Gilbert damping parameter for thin ferromagnet/normal metal double layers from the perspective of non-local damping by spin current emission. The nature of the magnetic damping is quite complex and various processes contribute to the dissipation of the magnetic energy. It is observed, that the damping parameter is strongly influenced by interface roughness. Therefore, only samples with a similar growth quality and interface roughness, can be directly compared by damping parameter. Comparing samples with various normal metal layers, it is found, enhanced damping by spin currents emission is observed for the Ni/Pd, Ni/Dy and Ni/Cr double layers. For these films, a 5nm metal layer completely absorbs the spin current, which is pumped from the nickel layer. The increase in the damping parameter is inversely proportional to the thickness of the nickel layer, as expected from the inverse volume dependence of the spin pumping torque. In addition to the damping parameter enhancement, the frequency spectrum of the Kittel $k = 0$ mode shifts to smaller values when the thickness of the nickel layer is reduced. This effect results partially from reduction of the gyromagnetic ratio by spin current emission.

Bibliography

- [1] A. T. J. Miltat, G. Albuquerque, *Spin dynamics in confined magnetic structures I*, Springer-Vorlag Berlin Heidelberg, 2002.
- [2] W. Döring, *Über die Trägheit der Wände zwischen Weißchen Bezirken*, Z. Naturforsch. **3a**, 373 (1948).
- [3] H. Goldstein, *Classical mechanics*, Addison-Wesley, Redford, 1980.
- [4] C. H. Back, K. Perzlmaier and M. Buess, *Magnetism: A synchrotron radiation approach*, Springer-Verlag Berlin Heidelberg, 2006.
- [5] J. Smit and H. Beljers, *Ferromagnetic resonance absorbtion in BaFe₁₂O₁₉ a highly anisotropic crystal*, Phil. Res. Rep. **10**, 113 (1955).
- [6] G. Eilers, M. Lüttich and M. Münzenberg, *Giant nonlocal damping by spin wave emission*, Phys. Rev. B **74**, 054411 (2006).
- [7] A. H. Morrish, *The physical principles of magnetism*, Wiley, New York, 1965.
- [8] W. K. Hiebert, A. Stankiewicz and M. Freeman, *Direct observation of magnetic relaxation in a small permalloy disk by time-resolved scanning Kerr microscopy*, Phys. Rev. Lett. **79**, 1134 (1997).
- [9] B. Koopmans, M. G. Koerkamp, T. Rasing and H. van den Berg, *Observation of large Kerr angles in the nonlinear optical response from magnetic multilayers*, Phys.Rev.Lett. **74**, 3692 (1995).
- [10] J. Hohlfeld, E. Matthias, R. Knorren and K. Bennemann, *Nonequilibrium magnetization dynamics of nickel*, Phys. Rev. Lett. **78**, 4861 (1997).
- [11] M. Lisowski, P. A. Loukakos, A. Melnikov, I. Radu, L. Ungureanu, M. Wolf and U. Bowensiepen, *Femtosecond electron and spin dynamics in Gd(0001) studied by time-resolved photoemission and magneto-optics*, Phys. Rev. Lett. **95**, 137402 (2005).

- [12] J. Vogel, W. Kuch, M. Bonfim, J. Camarero, Y. Pennec, F. Offi, K. Fukumoto, J. Kirschner, A. Fontaine and S. Pizzini, *Time-resolved magnetic domain imaging by x-ray photoemission electron microscopy*, Appl. Phys. Lett. **82**, 2299 (2003).
- [13] M. Bonfim, G. Ghiringhelli, F. Montaigne, S. Pizzini, N. B. Brookes, F. Petroff, J. Vogel, J. Camarero and A. Fontaine, *Element-selective nanosecond magnetization dynamics in magnetic heterostructures*, Phys. Rev. Lett. **86**, 3646 (2001).
- [14] S.-B. Choe, Y. Acremann, A. Scholl, A. Bauer, A. Doran, J. Stöhr and H. Padmore, *Vortex core-driven magnetization dynamics*, Sciencemag. **304**, 420 (2004).
- [15] C. Stamm and H. Dürr, Private correspondence .
- [16] C. Kittel, *On the theory of ferromagnetic resonance absorption*, Phys. Rev. **73**, 155 (1948).
- [17] J. Lindner, K. Lenz, E. Kosubek, K. Baberschke, D. Spoddig, R. Meckenstock, J. Pelzl, Z. Frait and D. Mills, *Non-Gilbert-type damping of the magnetic relaxation in ultrathin ferromagnets: Importance of magnon-magnon scattering*, Phys. Rev. B **68**, 060102 (2003).
- [18] J. Lindner and K. Baberschke, *Ferromagnetic resonance in coupled ultrathin films*, J. Phys.: Condens. Matt **15**, 465 (2003).
- [19] M. Farle, *Ferromagnetic resonance of ultrathin metallic layers*, Rep. Prog. Phys. **61**, 755 (1998).
- [20] M. Buess, T. Haug, M. R. Scheinfein and C. H. Back, *Micromagnetic dissipation, dispersion, and mode conversion in thin permalloy platelets*, Phys. Rev. Lett. **94**, 127205 (2005).
- [21] S. Mizukami, Y. Ando and T. Miyazaki, *The study on ferromagnetic resonance linewidth for NM/80NiFe/NM (NM= Cu, Ta, Pd and Pt) films*, Jpn. J. Apl. Phys. **40**, 580 (2001).
- [22] B. Hillebrands, *Magnetisierungsdynamik in magnetischen Strukturen*, Forschungszentrum Jülich GmbH, 2000.
- [23] J. Sandercock, *Light scattering in solids III*, Springer Verlag, Berlin, Heidelberg, New York, 1982.
- [24] B. Hillebrands, *Progress in multipass tandem Fabry-Perot interferometry: I. A fully automated, easy to use, self-aligning spectrometer with increased stability and flexibility*, Rev. Sci. Instr. **70**, 1589 (1999).
- [25] G. Srinivasan, C. E. Patton and P. R. Emtage, *Brillouin light scattering on yttrium iron garnet films in a magnetostatic wave device structure*, Jour. Appl. Phys. **6**, 1987 (61).
- [26] C. Mathieu, J. Jorzick, A. Frank, S. Demokritov, B. Hillebrands, B. Bartelien, C. Chappert, D. Decanini, F. Rousseaux and E. Cambril, *Lateral quantization of spin waves in micron size magnetic wires*, Phys. Rev. Lett. **81**, 3968 (1998).

-
- [27] J. Jorzick, S. O. Demokritov, B. Hillebrands, M. Bailleul, C. Fermon, K. Y. Guslienko and A. N. Slavin, *Spin wave wells in nonellipsoidal micrometer size magnetic elements*, Phys. Rev. Lett. **88**, 047204 (2002).
- [28] M. Djordjevic, M. Lüttich, P. Moschkau, P. Guderian, T. Kampfrath, R. Ulbrich, M. Münzenberg, W. Felsch and J. Moodera, *Comprehensive view on ultrafast dynamics of ferromagnetic films*, Phys. Stat. Sol. C **3**, 1347 (2006).
- [29] P. Moschkau, Zeitaufgelöste Reflektivitätsmessungen an ferromagnetischen dünnen Filmen, Master's thesis, Universität Göttingen, 2004.
- [30] E. Beaurepaire, J.-C. Merle, A. Daunois and J.-Y. Bigot, *Ultrafast spin dynamics in ferromagnetic nickel*, Phys. Rev. Lett **76**, 4250 (1996).
- [31] S. I. Anisimov, B. L. Kapeliovitch and T. L. Perel'man, Sov. Phys. JETP **39**, 375 (1974).
- [32] M. van Kampen, *Ultrafast spin dynamics in ferromagnetic metals*, PhD thesis, Technische Universiteit Eindhoven, 2003.
- [33] M. van Kampen, C. Jozsa, J. T. Kohlhepp, P. LeClair, L. Lagae, W. J. M. de Jonge and B. Koopmans, *All-optical probe of coherent spin waves*, Phys. Rev. Lett. **88**, 227201 (2002).
- [34] Z. Qiu and S. Bader, *Surface magneto-optic Kerr effect (SMOKE)*, J. Magn. Magn. Mater **200**, 664 (1999).
- [35] C.-Y. You and S.-C. Shin, *Generalized analytic formulae for magneto-optical Kerr effects*, Jour. Appl. Phys **84**, 541 (1998).
- [36] P. Bruno, Y. Suzuki and C. Chappert, *Magneto-optical Kerr effect in a paramagnetic overlayer on a ferromagnetic substrate: A spin-polarized quantum size effect*, Phys. Rev. B **53**, 9214 (1996).
- [37] T. Kampfrath, Zeitaufgelöste Messungen des magnetooptischen Kerr-Effektes an dünnen Eisenschichten, Master's thesis, Universität Göttingen, 2004.
- [38] B. Koopmans, *Spin dynamics in confined magnetic structures II*, Springer-Verlag Berlin Heidelberg, 2003.
- [39] M. Münzenberg, Untersuchungen zur Zwischenschichtkopplung bei La/Fe-Vielfachschichten und am Reorientierungsübergang von CeH₂/Fe-Vielfachschichten mit dem magnetooptischen Kerreffekt, Master's thesis, Universität Göttingen, 1997.
- [40] T. Kampfrath, R. G. Ulbrich, F. Leuenberger, M. Münzenberg, B. Sass and W. Felsch, *Ultrafast magneto-optical response of iron thin films*, Phys. Rev. B **65**, 104429 (2002).
- [41] S. Freundt, *Interferometrische Kreuzkorrelation mit Titan-Saphir-Laserpulsen an GaAs*, PhD thesis, Universität Göttingen, 1994.
- [42] M. Lüttich, Wiederaufbau eines Titan-Saphir-Lasers und magnetische Simulation, Master's thesis, Universität Göttingen, 2004.
- [43] *Operator's manual RegA Model 9000 Laser, Coherent.*

- [44] P. M. Oppeneer and A. Liebsch, *Ultrafast demagnetization in Ni: theory of magneto-optics for non-equilibrium electron distributions*, J. Phys. : Condens. Matter **16**, 5519 (2004).
- [45] L. Guidoni, E. Beaurepaire and J. Y. Bigot, *Magneto-optics in the ultrafast regime: thermalization of spin populations in ferromagnetic films*, Phys. Rev. Lett. **89**, 017401 (2002).
- [46] M. Djordjevic and M. Münzenberg, *Connecting the timescales in picosecond remagnetization experiments*, Phys. Rev. B **75**, 012404 (2007).
- [47] M. J. Donahue and D. G. Porter, *OOMMF User's Guide, Version 1.0*, Interagency Report NISTIR 6376, National Institute of Standards and Technology, Gaithersburg, MD (1999).
- [48] M. Donahue and R. D. McMichael, *Exchange energy representations in computational micromagnetics*, Physica B **233**, 272 (1997).
- [49] J. Fidler and T. Schrefl, *Micromagnetic modelling-the current state of the art*, J.Phys. D:Appl. Phys. **33**, R135 (2000).
- [50] U. Nowak, N. Kazantseva, R. Chantrell, O. Chubykalo-Fesenko, F. Garcia-Sanchez, O. N. Mryasov and A. Rebei, *Atomistic models of magnetization processes and devices*, in *International Conference on Magnetism, Kyoto, Japan*, 2006.
- [51] C. Jozsa, J. H. H. Rietjens, M. van Kampen, E. Smalbrugge, M. K. Smit, W. J. M. de Jonge and B. Koopmans, *Retrieving pulse profiles from pump-probe experiments on magnetization dynamics*, Jour. Appl. Phys. **95**, 7447 (2004).
- [52] M. Djordjevic, G. Eilers, A. Parge, M. Münzenberg and J. S. Moodera, *Intrinsic and non-local Gilbert Damping parameter in all optical pump-probe experiments*, Jour. Appl. Phys. **99**, 08F308 (2006).
- [53] B. Heinrich, K. Urquhart, A. Arrott, J. Cochran, K. Myrtle and S. Purcell, *Ferromagnetic-resonance study of ultrathin bcc Fe(100) films grown epitaxially on fcc Ag(100) substrates*, Phys. Rev. Lett. **59**, 1756 (1987).
- [54] J. Lindner, K. Lenz, E. Kosubek, K. Babeschke, D. S. adn R. Meckenstock, J. Pelzl, Z. Frait and D. L. Mills, *Non-Gilbert-type damping of the magnetic relaxation in ultrathin ferromagnets: importance of magnon-magnon scattering*, Phys. Rev. B **68**, 060102(R) (2003).
- [55] C. H. Back, D. Weller, J. Heidmann, D. Mauri, D. Guarisco, E. L. Garwin and H. C. Siegmann, *Magnetization reversal in ultrashort magnetic field pulses*, Phys. Rev. Lett. **81**, 3251 (1998).
- [56] M. Buess, T. P. J. Knowles, R. Höllinger, T. Haug, U. Krey, D. Weiss, D. Pescia, M. R. Scheinfein and C. H. Back, *Excitations with negative dispersion in a spin vortex*, Phys. Rev. B **71**, 104415 (2005).
- [57] M. Buess, R. Höllinger, T. Haug, K. Perzlmaier, U. Krey, D. Pescia, M. R. Scheinfein, D. Weiss and C. H. Back, *Fourier transform imaging of spin vortex eigenmodes*, Phys. Rev. Lett. **93**, 077207 (2004).

-
- [58] J. Jorzick, S. Demokritov, B. Hillebrands, B. Bartenlian, C. Chappert, D. Decanini, F. Rousseaux and E. Cambril, *Quantized spin wave modes in micron size magnetic disks*, Jour. Appl. Phys. **87**, 5082 (2000).
- [59] G. Gubbiotti, C. Carlotti, T. Okuno, T. Shinjo, F. Nizzoli and R. Zivieri, *Brillouin light scattering investigation of dynamic spin modes confined in cylindrical Permalloy dots*, Phys. Rev. B **68**, 184409 (2003).
- [60] G. Gubbiotti, M. Kostylev, N. Sergeeva, M. Conti, G. Carlotti, T. Ono, A. Slavin and A. Stashkevich, *Brillouin light scattering investigation of magnetostatic modes in symmetric and asymmetric NiFe/Cu/NiFe trilayered wires*, Phys. Rev. B **70**, 224422 (2004).
- [61] J. Morkowski, *Rapid magnon relaxation*, Jour. Phys. Conf. Ser. **30**, 17 (2006).
- [62] S. M. Bhagat and P. Lubitz, *Temperature variation of ferromagnetic relaxation in the 3d transition metals*, Phys. Rev. B **10**, 179 (1974).
- [63] G. Woltersdorf, B. Heinrich, J. Woltersdorf and R. Scholz, *Spin dynamics in ultrathin film structures with a network of misfit dislocations*, Jour. Appl. Phys. **95**, 7007 (2004).
- [64] R. Arias and D. Mills, *Extrinsic contributions to the ferromagnetic resonance response of ultrathin films*, Phys. Rev. B **60**, 7395 (1999).
- [65] M. D. Stiles, *Spin transfer torque in non-uniform magnetizations*, in *ICM 2006 Conference proceedings*, 2006.
- [66] M. Hayashi, L. Thomas, Y. B. Bazaliy, C. Rettner, R. Moriya, X. Jiang and S. P. Parkin, *Influence of current on field-driven domain wall motion in permalloy nanowires from time resolved measurements of anisotropic magnetoresistance*, Phys.Rev. Lett. **96**, 197207 (2006).
- [67] M. Fähnle and D. Steiauf, *Dissipative magnetization dynamics close to the adiabatic regime*, Private correspondence (2006).
- [68] M. Fähnle, *Nanosecond relaxation processes, theory and experiment*, in *SPP 1133 Workshop Göttingen*, 2005.
- [69] B. Koopmans, J. J. M. Ruigrok, F. D. Longa and W. J. M. de Jonge, *Unifying ultrafast magnetization dynamics*, Phys.Rev.Lett. **95**, 267207 (2005).
- [70] V. Kambersky, *On the Landau-Lifshitz relaxation in ferromagnetic metals*, Can. Jour. Phys. **48**, 2906 (1970).
- [71] Y. Yafet, *g-factors and spin lattice relaxation of conduction electrons*, Solid State Physics **14**, 1 (1963).
- [72] D. Zubarev, Usp.Fiz.Nauk. **71**, 71 (1960).
- [73] R. Elliott, *Theory of the effect of spin-orbit coupling on magnetic resonance in some semiconductors*, Phys. Rev. **96**, 266 (1954).
- [74] B. Heinrich and Z. Frait, *Temperature dependence of the FMR linewidth of iron single-crystal platelets*, Phys. Stat. Sol. **16**, K11 (1966).

- [75] S. Zhang and Z. Li, *Roles of nonequilibrium conduction electrons on the magnetization dynamics of ferromagnets*, Phys. Rev. Lett. **93**, 127204 (2004).
- [76] M. Fähnle, R. Singer, D. Steiauf and V. P. Antropov, *Role of nonequilibrium conduction electrons on the magnetization dynamics of ferromagnets in the s-d model*, Phys.Rev.B **73**, 172408 (2006).
- [77] Y. Tserkovnyak, A. Brataas and G. Bauer, *Enhanced Gilbert damping in thin ferromagnetic films*, Phys. Rev. Lett. **88**, 117601 (2002).
- [78] B. Heinrich, D. Meredith and J. Cochran, *Wave number and temperature dependent Landau-Lifshitz damping in nickel*, Jour. Appl. Phys. **50**, 7726 (1979).
- [79] V. Korenman and R. Prange, *Anomalous damping of spin waves in magnetic metals*, Phys. Rev. B **6**, 2769 (1972).
- [80] D. Steiauf and M. Fähnle, *Damping of spin dynamics in nanostructures: An ab initio study*, Phys. Rev. B **72**, 064450 (2005).
- [81] Y. Tserkovnyak, G. Fiete and B. Halperin, *Mean-field magnetization relaxation in conducting ferromagnets*, Appl. Phys. Lett. **84**, 5234 (2004).
- [82] Y. Tserkovnyak, A. Brataas and G. Bauer, *Dynamic exchange coupling and Gilbert damping in magnetic multilayers*, Jour. Appl. Phys. **93**, 7534 (2003).
- [83] Y. Tserkovnyak, A. Brataas and G. Bauer, *Spin pumping and magnetization dynamics in metallic multilayers*, Phys. Rev. B **66**, 224403 (2002).
- [84] Y. Tserkovnyak, A. Brataas, G. E. W. Bauer and B. I. Halperin, *Nonlocal magnetization dynamics in ferromagnetic hybrid nanostructures*, cond-mat **0409242 v1** (2004).
- [85] J. Slonczewski, *Current-driven excitation of magnetic multilayers*, J. Magn. Magn. Mater. **159**, L1 (1996).
- [86] K. Xia, P. Kelly, G. Bauer, A. Brataas and I. Turek, *Spin torques in ferromagnetic/normal-metal structures*, Phys. Rev. B **65**, 220401 (2002).
- [87] R. Urban, G. Woltersdorf and B. Heinrich, *Gilbert damping in single and multilayer ultrathin films: Role of interfaces in nonlocal spin dynamics*, Phys. Rev. Lett. **87**, 217204 (2001).
- [88] S. Ingvarsson, L. Ritchie, X. Y. Liu, G. Xiao, J. C. Slonczewski, P. L. Trouilloud and R. H. Koch, *Role of electron scattering in the magnetization relaxation of thin $Ni_{81}Fe_{19}$ films*, Phys. Rev. B **66**, 214416 (2002).
- [89] S. Mizukami, Y. Ando and T. Miyazaki, *Effect of spin diffusion on Gilbert damping for a very thin permalloy layer in Cu/permalloy/Cu/Pt films*, Phys. Rev. B **66**, 104413 (2002).
- [90] G. Woltersdorf, M. Buess, B. Heinrich and C. H. Back, *Time resolved magnetization dynamics of ultrathin Fe(001) films: Spin-pumping and two-magnon scattering*, Phys. Rev. Lett. **95**, 037401 (2005).

Danksagung

Die vorliegende Doktorarbeit ist das Ergebnis von über 3 Jahren Arbeit am 4. Physikalischen Institut der Universität Göttingen. Ohne die Unterstützung, die ich von meinen Kollegen, Freunden und meiner Familie während dieser Zeit bekam, wäre diese Arbeit wohl nicht in der vorliegenden Form zustande gekommen.

Im Folgenden möchte ich den vielen Menschen, deren Zeit und Nerven ich in Anspruch genommen habe, meinen Dank aussprechen.

- Prof. Dr. Markus Münzenberg, für die von ihm erfahrene Betreuung und Unterstützung, die mich nie vom rechten Weg abkommen ließ; und für sein Vertrauen auf meine Fähigkeiten von der ersten Stunde an;
- Prof. Dr. Christian Back, dafür, dass er so viel Mühe und einen langen Weg auf sich genommen hat, um die Stelle als Korreferent annehmen zu können.

Meiner gesamten Arbeitsgruppe für die gewinnbringende Arbeitsatmosphäre, aber ganz besonders

- Gerrit Eilers, für die Herstellung der Proben, deren Anzahl die Hunderter-Marke mit Leichtigkeit durchbrach;
- Anne Parge, für angebrachte Korrekturen, sowie ganz besonders für die von ihr erfahrene moralische Unterstützung und Zusammenarbeit in dem wohl schönsten Büro im Institut;
- Mario Lüttich und Peter Moschkau, für die gute gemeinsame Zusammenarbeit während der Entstehung des Femto-Labors;
- Matthäus Pietz und Stefan Bretschneider, für ihre Unterstützung und nicht enden wollende Diskussionen.

Weiterer Dank geht an

- Daniel Steiauf, dafür, dass er sein Wissen über die Theorie der magnetischen Dämpfung mit mir geteilt hat;
- Jan Petersen, für die von ihm durchgeführten X-Ray Messungen;

Alle Kollegen des 4. Physikalischen Institutes, für die unzähligen und fruchtbaren Gespräche, die entgegengebrachte Freundlichkeit und das schöne, meine dortige Arbeit unterstützende Klima;

- Georg Müller und Daniel Quinlan, durch deren angebrachte Korrekturen meine Arbeit sich auf dem jetzigen Stand befindet;

An die Teams der Elektronischen und Mechanischen Werkstatt der 4. Physik, sowie der Zentral Werkstatt, für ihre schnelle und freundliche Hilfe zu jeder Zeit.

Mein ganz besonderer Dank geht an

- Meinen Ehemann Timm, für sein aufgebrachtes Verständnis und seine moralische Unterstützung und Motivation an guten wie an schlechten Tagen;
- Meine Familie, für ihre Unterstützung und Hilfe in allen Lebenslagen und, dass sie mir immer das Gefühl gegeben haben, ich könne alles erreichen.

Ich möchte mich weiterhin noch bei all meinen Freunden und Bekannten für ihre Hilfe und die schöne gemeinsame Zeit in Göttingen bedanken, ganz besonders bei

- Marco Bertelli, durch den ich in Gesprächen auch einmal aus der Welt der Physik entfliehen konnte.

Lebenslauf

PERSÖNLICHE ANGABEN

Name: Marija Djordjević Kaufmann

Familienstand: verheiratet

Staatsangehörigkeit: serbisch

Geburtsdatum: 09.06.1978

Geburtsort: Niš, Serbien

SCHULAUSBILDUNG

1985 - 1993 Grundschule *Čegar*, Niš, Serbien

1993 - 1997 Gymnasium *Svetozar Marković*, Niš, Serbien

HOCHSCHULAUSBILDUNG

Studium der Physik an der Universität Belgrad, Serbien

WS 1997/1998 Aufnahme des Studiums

11/2002 Diplom, Thema der Diplomarbeit:
„PULSED LASER DEPOSITION OF TITANIUM-
DIOXIDE ON A SILICIUM SURFACE”

01/2003 Beginn der vorliegenden Dissertation

seit 01/2003 Wissenschaftliche Mitarbeiterin der Universität
Göttingen

seit 06/2004 Mitarbeiter im Schwerpunktprogramm 1133:
„ULTRAFAST MAGNETIZATION PROCESSES” der
Deutschen Forschungsgemeinschaft

Göttingen, Oktober 2006

Marija Djordjević Kaufmann